Multilayered magnetic nanoparticles fabricated by nanoimprint lithography for magnetomechanical treatment of cancer

Byung Seok Kwon

A dissertation

Submitted in partial fulfillment of the requirement for the degree of

Doctor of Philosophy

University of Washington

2017

Reading Committee

Dr. Kannan M. Krishnan, Chair

Dr. Karl F. Bohringer

Dr. Lucien N. Brush

Dr. Qiuming Yu

Program Authorized to Offer Degree:

Materials Science & Engineering

University of Washington

Abstract

Multilayered magnetic nanoparticles fabricated by nanoimprint lithography

for magnetomechanical treatment of cancer

Byung Seok Kwon

Chair of Supervisory Committee:

Prof. Kannan M. Krishnan

Materials Science & Engineering

Fe_3O_4-magetite nanoparticles have received wide interest as prominent agents for various biomedical applications, ranging from target-specific cancer treatment, gene therapy, and Magnetic Particle Imaging (MPI). However, Fe_3O_4-magnetite nanoparticles, synthesized

by chemical methods beyond a certain size, present challenges in controlling size distribution and shape. Similarly, Fe_3O_4-magnetite nanoparticles fabricated by conventional top-down lithographic methods present difficulty of controlling defects and lead to agglomeration due to large size. In order to overcome the difficulties associated with the conventional chemical and top-down lithographic methods, it is critical to develop a fabrication method which produces homogeneous nanoparticles in large quantities with the control of size, defects, and structure.

Furthermore, the concept of cell death induced by mechanical perturbation has received wide attention as a way to maximize the cancer cell death with minimal side effects. Previous study has proposed the use of permalloy disk-shaped vortex state microparticles, in order to create cancer cell death by mechanical force. However, insufficient biocompatibility, inadequate mechanical force created by vortex switching, and inability to control the particle size have been critical issues to be further researched and proceeded for *in vivo* application.

Hence, we studied physical and magnetic properties of Fe_3O_4 as a material in thin film form and proceeded to develop Fe_3O_4 based synthetic antiferromagnetic (SAF) thin films. Then, we combined these favorable physical/magnetic properties with nanoimprint lithography to fabricate homogeneously patterned synthetic antiferromagnetic (SAF) nanoparticles (wafer area >1 x 1 cm^2) with the control of size, shape and structure. Then we demonstrated the release of these particles in an aqueous environment. The fabrication process combines a tetrafluoroethylene (ETFE) "working stamp", a bi-layer resist lift-off, defect-free nanoimprint and sputtering in order to fabricate synthetic antiferromagnetic (SAF) nanoparticles. SAF nanoparticles are composed of alternating magnetic/non-magnetic multilayers to prevent any agglomeration in spite of the ferromagnetic nature of the particles. This heterostructure gives rise to nearly zero magnetic remanence and coercivity values and

also prevents possible oxidation of Fe_3O_4. The superparamagnet-like behavior (nearly zero remanence and coercivity) of SAF nanoparticles suggests that the SAF nanoparticles with favorable geometry fabricated by top-down methods have potential for biomedical application.

In order to prove the suitability of SAF nanoparticles for biomedical application, we initially controlled the movement of these SAF nanoparticles with A.C magnetic field, and mechanically rotated them in solution. After we have studied field frequency dependence on mechanical rotation, these SAF nanoparticles were implemented in *in vitro* environment to test the biocompatibility of these SAF nanoparticlesn, and also to confirm the effectiveness of mechanical force created by A.C magnetic field in order to kill cancer cells. This proof of concept successfully eradicated cancer cells with these SAF nanoparticles. We have demonstrated the effective cancer death after 16 minutes of exposure to mechanically rotating SAF nanoparticles under frequency of 1 Hz (>92% cell death). Furthermore, under the same frequency and exposure time, we have shown that up to 1:4 (nanoparticles:cell) concentration, the mechanical perturbation is effective to kill cancer cells (>80% cell death). However, we suggest to further study the biological mechanism of cancer cell death by mechanical perturbation to truly understand this phenomenon.

Acknowledgement

I would like to thank Professor Kannan Krishnan for giving me the opportunity to join his group and work in the exciting field of nanomagnetic materials for biomedical application. I wouldn't have achieved who I am today without his support and guidance. I have grown to be a better researcher as well as a better person through last 5 years of my life.

Also, I would like to thank my committee members, Prof. Karl Bohringer, Prof. Lucien Brush and Prof. Quiming Yu for their time and support, which helped to make this work complete.

Personally, I would like to dedicate this to my beloved family, Seok Ha Kwon, Mi Kyung Cho, and Ha Kyung Kwon, who have supported me unconditionally through this long journey. Without them, I couldn't have made my ends meet. No matter what I have done, they have trusted me and supported me to be who I am today in 2017.

For last 3 years, I struggled everyday to be a better person, but this would have been really painful process without Joan Kim. She has been with me throughout the this long process and have taught me to be positive everyday. When I am down, she encouraged me to try again, and I am up, she was truly happy with my achievements. Without you, I wouldn't have made this far.

Through my ph.D career, Dr. Wei Zhang has been my mentor, who has not only taught me the technical knowledge, but also never to give up. With your encouragement, I was able to successfully finish my ph.D career.

Dr. Yufeng Hou has been my mentor who has guided me through the future path and has taught me to keep trying even if I fail at the moment. With your encouragement and help, I was able to end up in Silicon Valley.

Dr. Zheng Li has been the mentor, who has helped me very closely. I was able to learn what I should do next in my life seeing you taking a step. I have learned so much from you and this is the reason why I was able to finish up the grand goal, ph.D.

My group colleagues have also given me tremendous help in the past five years. I want to express the gratitude to them, Dr. Matt Ferguson, Dr. Amit Khandhar, Mark Brunson, Dr. Hamed Arami, Eric Teeman and Ryan Hufschmid, for their helpful suggestions and support.

Part of this work was done at the Washington Nanofabrication Facility/Molecular Analysis Facility, A National Nanotechnology Coordinated Infrastructure (NNCI) site at University of Washington.

Thank you everyone who I have not mentioned. Without your support and care, I wouldn't have been able to go this far.

Table of Contents

Chapter 1

Introduction, Background, and Motivation

1.1. Fe_3O_4-magnetite nanoparticles for biomedical application

Fe_3O_4-magnetite nanoparticles have potential use in biological and biomedical applications[1], ranging from Magnetic Particle Imaging (MPI) [2], to direct drug delivery and hyperthemia[3], as well as stem cell tracking and gene therapy[1]. Unlike most metallic ferromagnetic materials (e.g., Co, Ni) that are not biocompatible, Fe_3O_4-mangetite is known to demonstrate adequate magnetic properties and bio-compatibility[4].

Conventionally, Fe_3O_4-mangetite nanoparticles have been fabricated using "bottom-up" chemical synthesis methods such as iron salts[5,6], micro-emulsion[7], polyols process[8], and decomposition of iron pentacarbonyl[9]. These processes can be scaled up for mass production, but fail in controlling the shape, size, structure, phase purity and defects in particles larger than ~30 nm in size. At room temperature, spherical nanoparticles of magnetite demonstrates a superparamagnetic behavior for sizes below ~27 nm[10] for a measurement time of 100s. Larger particles, ≥27 nm in diameter, tend to be ferrimagnetic and agglomerate due to magnetic dipolar coupling. To resolve such issues, "top-down" fabrication methods were proposed and investigated as an alternative approach. Of particular importance, nanoimprint lithography was initially developed to directly pattern the resist using a mold. However, the "top-down" fabrication methods alone cannot resolve the

agglomeration issue due to the magnetic dipolar coupling.

In order to resolve the agglomeration issue, the concept of synthetic antiferro/ferrimagnetic nanoparticles (SAF) was proposed[11]. SAF configuration refers to a multi-layered structure composed of alternating ferro/ferrimagnetic layers separated by non-magnetic layers. In this configuration, alternating ferro/ferrimagnetic layers are magnetostatically coupled and in its ground state, leads to antiparallel orientation of the magnetization between the nearest ferro/ferrimagnetic layers and renders them effectively antiferro/ferrimagnetic with near-zero remanent magnetization. Thus, magnetic nanoparticles with a SAF configuration can be fabricated in much larger sizes without risking agglomeration.

1.2. Mechanical rotation of magnetic nanopraticles for biomedical application

As mentioned in § 1.1, numerous studies have been done using magnetic nanoparticles for treating cancer; hyperthermia[1-3,12] is a promising method to treat cancer cells via heat generated by high frequency of external magnetic field (> 100 kHz). However, soon, it was found to pose health risks. The heat created from the relaxation of magnetic nanoparticles, subject to AC fields, also destroys a large area of healthy cells around the nanoparticles, which cause necrosis. In order to overcome the limitations of this treatment method, Kim *et al* proposed using low AC magnetic field to mechanically rotate the magnetic nanoparticles, and without any heat induction[13]. This particular idea of mechanical destruction of cells is shown in the schematic diagram of Figure 1.1.

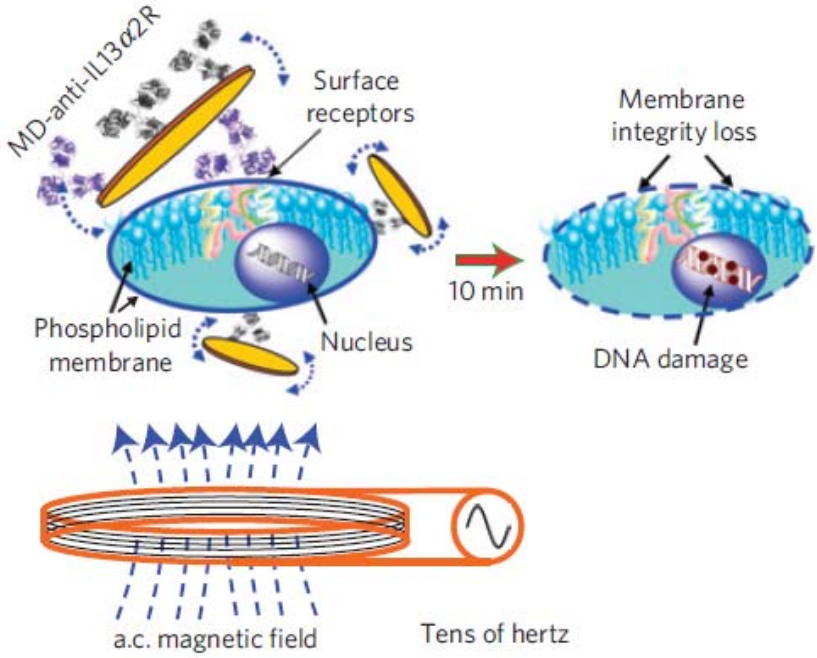

Figure 1.1. The concept of targeted magnetomechanical cancer-cell destruction using disc-shaped magnetic particles possessing a *spin-vortex* ground state. The micro-discs are bio-functionalized with anti-human IL13α2R antibody, specifically targeting human glioblastoma cells. After targeting, when an alternating magnetic field is applied, the magnetic discs physically oscillate, compromising membrane integrity and initiating spin-vortex-mediated programmed cell death. Reproduced from [Kim, DH et al, "Biofunctionalized magnetic-vortex microdiscs for targeted cancer-cell destruction", Nature Materials 9.2 (2010): 165-171], with permission of Nature Publishing Group

These permalloy nanodisks can rotate mechanically due to field-induced switching of the vortex state, and can cause apoptosis in the process.. However, permalloy disk-shaped magnetic particles readily oxidize in solution or *in vivo*. In addition, the vortex state of a disk-shaped particle still retains a considerable magnetic remanence and coercivity, which can cause particles to agglomerate. Furthermore, these particles are too large (>~1 μm) to be recommended for use in biomedical applications. These properties pose critical concern for a safe implementation of the nanoparticles into the body.

Furthermore, vortex state nanoparticles mechanically rotate due to the movement of the magnetic singularity within the nanoparticles, as this mechanism also induces vibration of nanoparticles. This vibration effect cannot be controlled, which might induce additional

mechanical force that is not desired [13].

Subsequent studies have yet to find safe, non-oxidizing, nano-sized particles with no magnetic remanence and coercivity. Nonetheless, some further studies were conducted, but the material, structure and size of nanoparticles were not tailored for biomedical application[14,15].

Therefore, combining the concept of synthetic antiferromagnetism and mechanical rotation for biomedical application, we propose to utilize Fe_3O_4-magnetite SAF nanoparticles released in solution to induce the mechanical rotation for biomedical application. Compared to the movement of the magnetic singularity of the vortex state, physical rotation via SAF nanoparticles is expected to be well-controlled. In addition, Fe_3O_4-magnetite SAF nanoparticles are expected to be much more bio-compatible than permalloy vortex state nanoaprticles. This is the primary motivation for fabricating and releasing heterostructure elements for biomedical application

1.3. Fundamental material characteristic of Fe_3O_4-magnetite

Fe_3O_4-magnetite has suitable magnetic properties and bio-compatibility among different composition of iron oxides. More specifically, iron oxide has four distinct chemical phases: FeO-Wustite, α-Fe_2O_3-hematite, γ-Fe_2O_3-maghemite, Fe_3O_4-magnetite. Unlike other chemical phases of iron oxides, Fe_3O_4-magnetite has distinct crystal structure which leads to its unique magnetic properties. First, Fe_3O_4-magnetite is a ferrimagnetic material which has a chemical formula of iron (II, III) oxide ($Fe^{2+}Fe^{3+}{}_2O_4$). Due to its cations occupying the octahedral and tetrahedral sites, Fe_3O_4-magnetite has inverse spinel structure[16] (Figure 1.2).

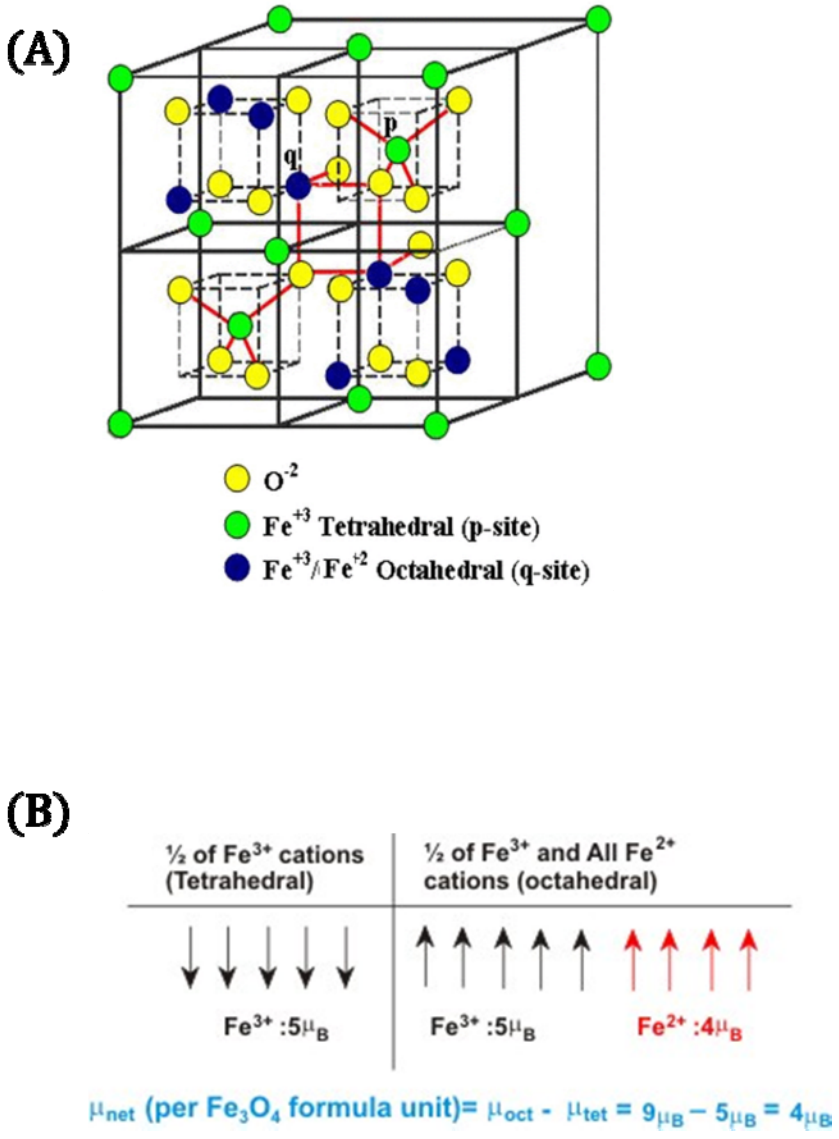

Figure 1.2. (A) Schematic illustration of the inverse spinel structure (ex. magnetite-Fe_3O_4). Reproduced from [Mund, HS *et al*, "Investigation of orbital magnetization in inverse spinel cobalt ferrite using magnetic Compton scattering", J. Appl. Phys. 110, 073914 (2011)] with permission of AIP publishing LLC. (B) showing the imbalance of octahedral and tetrahedral sites occupation, leading to total magnetic moment of 4μB.

In inverse spinel structure, magnetic moments of cations occupying octahedral sites and those occupying tetrahedral sites are in opposite direction, which is a fundamental characteristic of ferrimagnetism. However, due to its imbalance of octahedral and tetrahedral sites occupation, Fe_3O_4-magnetite results in a net moment of 4μB per formula unit[17]. After

fabricating Fe_3O_4-magnetite nanoparticles, we must confirm that the resulting material is sufficiently phase pure. Fe_3O_4-magnetite has suitable magnetic properties and bio-compatibility among different compositions of iron oxide. In order to distinguish between FeO-wustite, α-Fe_2O_3-hematite, γ-Fe_2O_3-maghemite, and Fe_3O_4-magnetite, several methods have been utilized including X-ray Diffraction (XRD)[18], X-ray photoelectron spectroscopy (XPS)[19,20], Raman spectroscopy[21-23], Electron energy loss spectroscopy (EELS)[24], and Mossbauer spectroscopy[25,26]. Among such methods, only Raman and Mossbauer spectroscopy have been used to clearly distinguish the three composition[21-23,25,26]. Figure 1.3 and 1.4 show Raman spectroscopy and Mossbauer spectroscopy of different phase of iron oxides respectively. However, other characterization methods, such as XRD, XPS or EELS, show slight differences in either peak intensity (XRD) (Figure 1.5) or presence of parasite peaks (XPS) (Figure 1.6) between different phases. Therefore, these methods are not conclusive on their own to clearly distinguish between the different phases. In my thesis, we utilize XRD in order to first partially confirm the phase of our fabricated iron oxide thin film. Then we further chacterize our fabricated iron oxide thin films with Raman spectroscopy in order to confirm the phase of iron oxide that we fabricate.

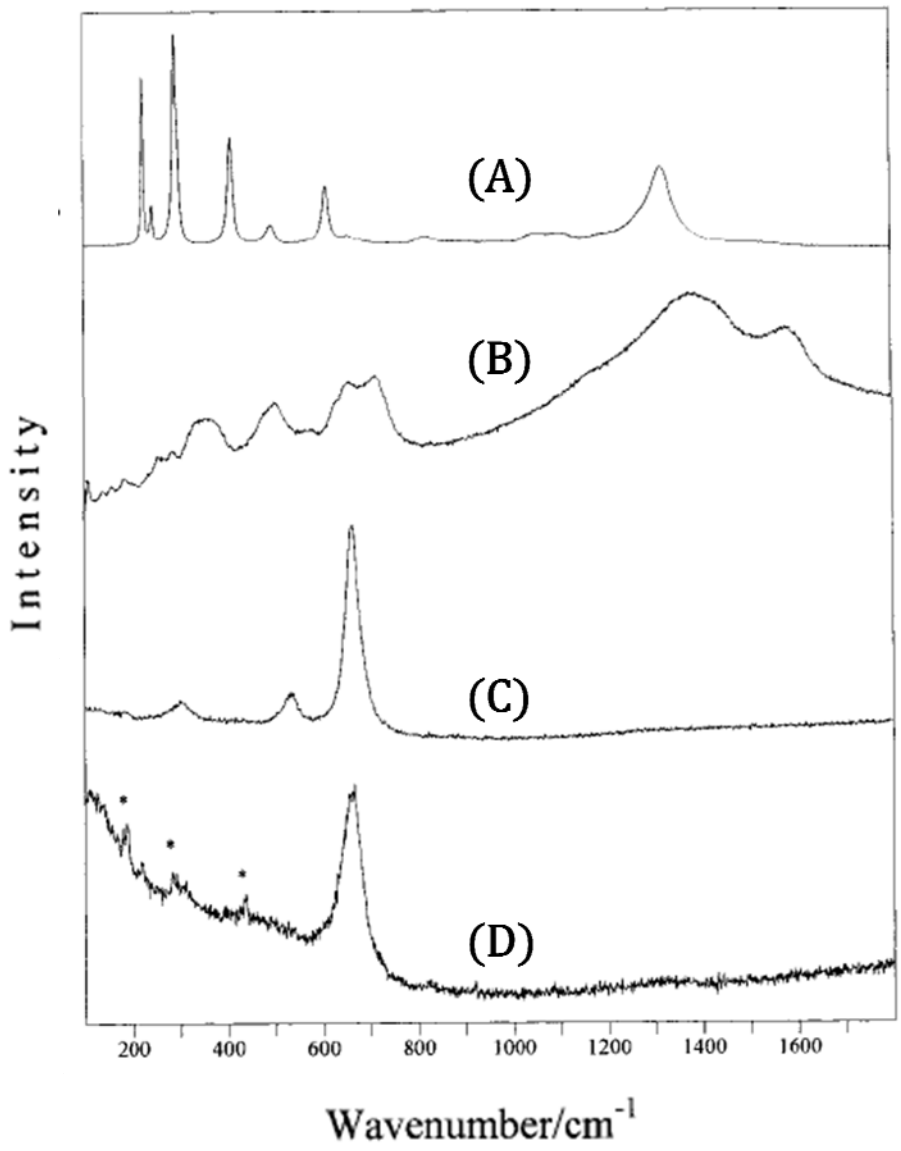

Figure 1.3. Raman spectra of different composition of iron oxide, including α-Fe_2O_3-hematite (A), γ-Fe_2O_3-maghemite (B), Fe_3O_4-magnetite (C), and FeO-wustite (D) [21]. In order to distinguish Fe_3O_4-magnetite phase, please note the presence of signature peaks at 650 cm^{-1}, 580 cm^{-1} and 300 cm^{-1}, which are not observed in α-Fe_2O_3-hematite, and γ-Fe_2O_3-maghemite phases. reproduced from [De Faria. D et al, "Raman Microscpectroscopy of some iron oxides and oxyhydroxides", Journal of Raman spectroscopy 28.11 (1997): 873-878] with permission of Wiley Online Library.

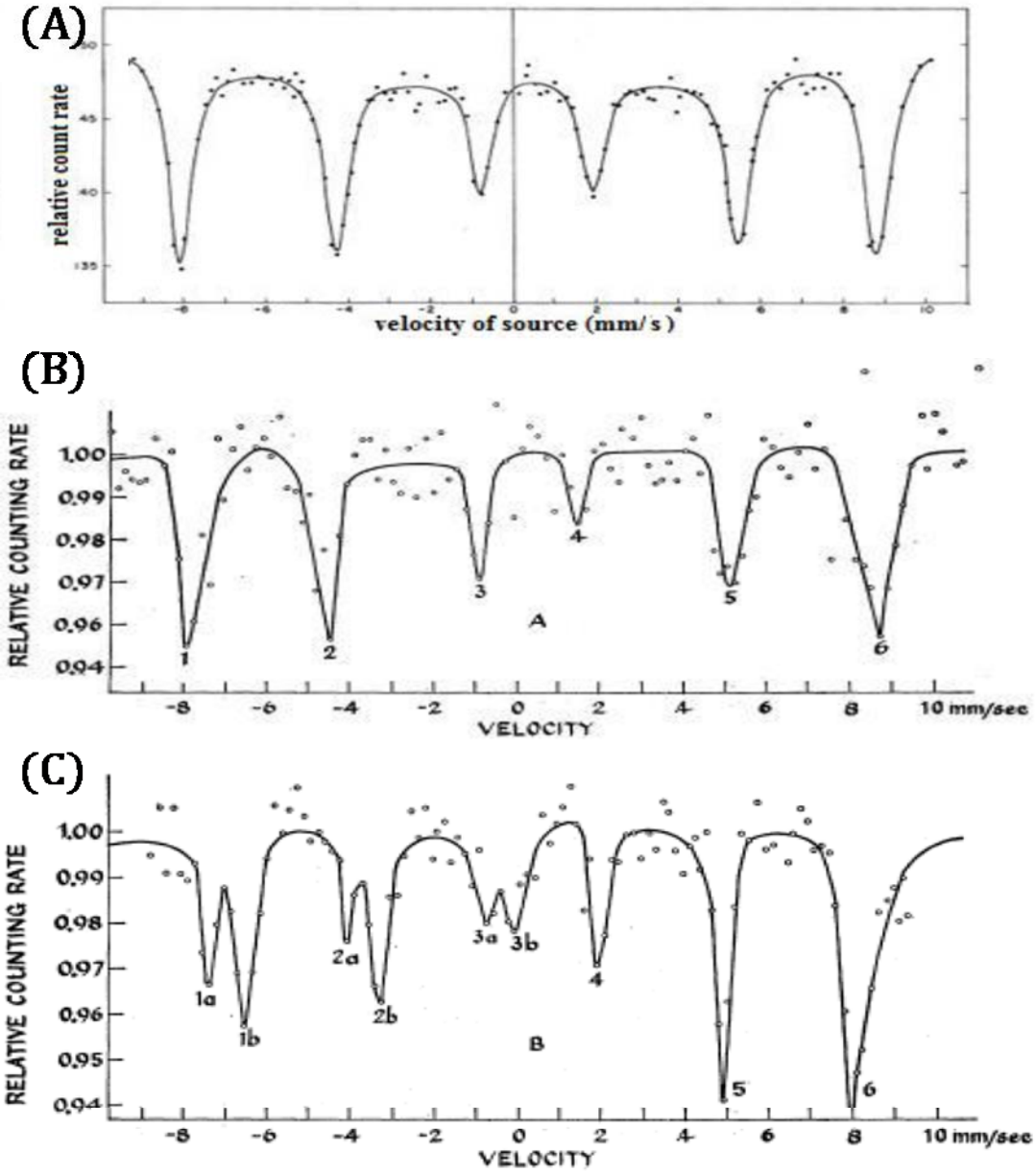

Figure 1.4. Mossbauer spectroscopy of different phase of iron oxide at 85K: (A) α-Fe_2O_3-hematite, (B) γ-Fe_2O_3-maghemite, and (C) Fe_3O_4-magnetite. Note that the Fe_3O_4-magnetite peak has satellite peaks (1a, 1b, 2a, 2b, 3a, and 3b), which are not observed in α-Fe_2O_3-hematite, and γ-Fe_2O_3-maghemite spectra[25], reproduced from [Carpenter, E. E., et al. "Magnetic and Mössbauer spectroscopy studies of nanocrystalline iron oxide aerogels." *Journal of applied physics* 99.8 (2006): 08N711.] with permission of AIP publishing LLC.

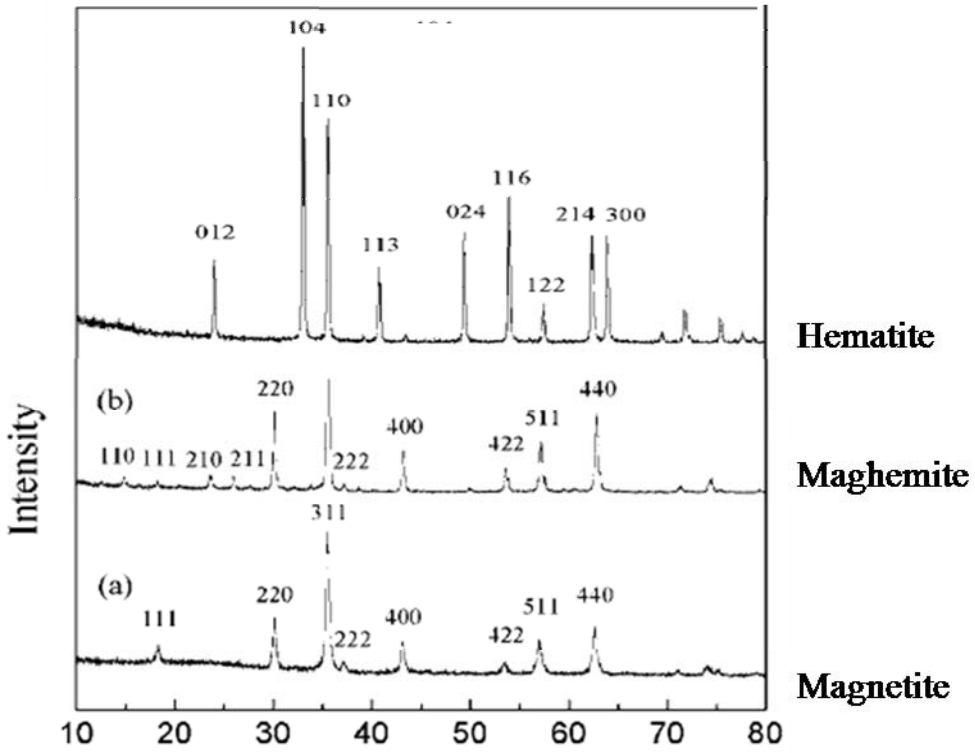

Figure 1.5. XRD spectra using Cu Kα radiation of α-Fe_2O_3-hematite, γ-Fe_2O_3-maghemite, and Fe_3O_4-magnetite from. γ-Fe_2O_3-maghemite, and Fe_3O_4-magnetite have characteristic peak of 34.5°, 35°, 36°. α-Fe_2O_3-hematite only has partiall overlap with those characteristic peak locations (35°), which can partially confirm the phase of iron oxide of a fabricated sample. Reproduced from [Yuan, S *et al.*" Structural evolution from mesoporous α-Fe_2O_3 to Fe_3O_4@C and γ-Fe_2O_3nanospheres and their lithium storage performances" , *CrystEngComm* 13.14 (2011): 4709-4713] with permission of Royal Society of Chemistry

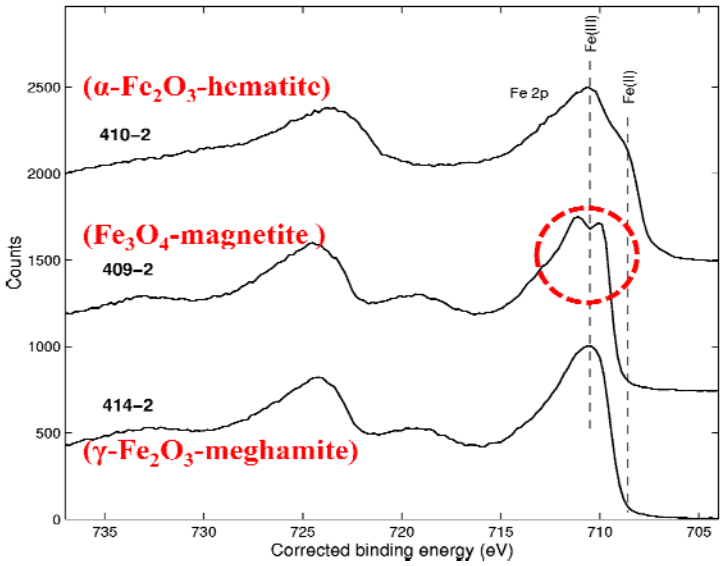

Figure 1.6. XPS spectra of α-Fe_2O_3-hematite, γ-Fe_2O_3-maghemite, and Fe_3O_4-magnetite. Note the existence of a parasite peak from Fe_3O_4-magnetite spectra (red circle), which can distinguish the phase of Fe_3O_4-magnetite from other phases of iron oxide. However, this peak is not distinct enough to evidently confirm Fe_3O_4-magnetite from a fabricated sample. Reproduced from [Chambers, S.A. et al. "Fe 2p core-level spectra for pure, epitaxial α-Fe_2O_3-(0001), γ-Fe_2O_3(001), and Fe_3O_4(001)", Surface Science Spectra 5.3 (1998): 219-228] with permission from AIP publishing LLC.

1.4. Synthetic Antiferromagnetism

Synthetic antiferomagnetism (SAF) is observed in two or more thin ferromagnetic layers separated by a non-magnetic layer (spacer). Dipolar coupling between the ferromagnetic layers results in antiparallel alignment of the magnetization of the neighboring ferromagnetic layer. Conventionally, SAF configuration has been mostly utilized in spin valve head[27,28] or giant magnetoresistance[29-33]. Figure 1.7 shows the schematic drawing of the SAF biased single spin valve head. However, SAF started to be recognized as potential elements for biomedical application for its near zero magnetic remanence and near zero coercivity.

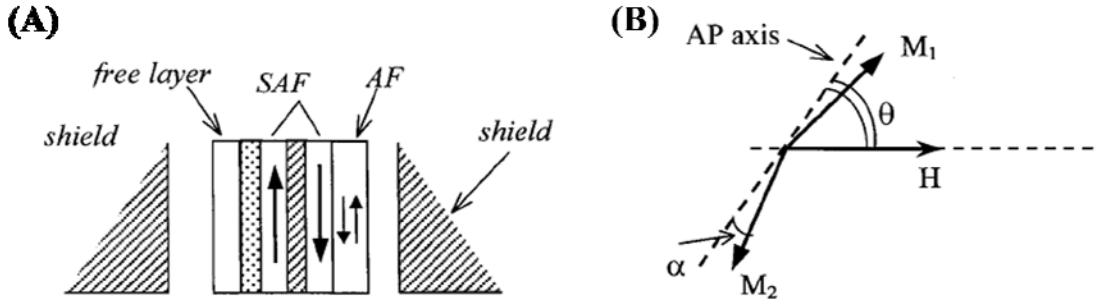

Figure 1.7. (A) Schematic drawing of SAF biased single spin valve head. AF is an antiferromagnetic film providing pinning, (B) an SAF under an applied field H, M_1 and M_2 denote the magnetization vector of the two magnetic layers in the SAF. Reproduced from [Zhu, J. "Spin valve and dual spin valve heads with synthetic antiferromagnets" IEEE transactions on magnetics, 35.2 (1999): 655-660 with permission of IEEE.

Hu *et al*. combined the concept of artificial antiferromagnetism and nanoimprint lithography to fabricate aqueous-stable SAF nanoparticles[11,34,35]. These SAFs have distinct advantages over chemically synthesized particles, such as higher magnetic moment due to larger particles size, homogeneous particle size, and near-zero remanence preventing agglomerations over a wide range of particle sizes from tens of nanometers to micrometers. In our group, Zhang *et al* used ethylene tetrafluoroethylene (ETFE) to create a "working stamp" instead of using a "master" silicon mold for imprinting. Using this ETFE stamp, they demonstrated improved process in terms of defects prevention and direct release[36]. The use of flexible ETFE working stamp prevented significant defects being induced from the rigid silicon mold as well as the degradation, with use, of the silicon mold itself. Through this method, they were able to achieve direct release of high-quality disk-shaped magnetic nanoparticles in solution using an ETFE "working stamp", bilayer resist lift-off, and silicon etching process specifically designed for the release of the nanoparticles[36]. This method demonstrated by the fabrication of disk-shaped nanoparticles, consisting of Fe/Ta multilayers, lacks good biocompatibility and favors an in-plane magnetization, due to their strong shape anisotropy, As a result, magnetic nanoparticles with sophisticated shapes and complex

structures are being investigated for improved magnetic response and functionality[37,38].

Chapter 2

Methods: Thin film deposition, Nanofabrication, Characterization, Micromagnetic simulation

In chapter 2, we discuss: (i) thin film deposition by magnetron and ion beam sputtering system, (ii) nanofabrication by electron-beam lithography, and nanoimprint lithography, (iii) characterization of crystalline structure (XRD), micro/nano-structure (SEM, TEM, AFM), composition (Raman Spectroscopy), magnetic behavior (VSM, and MFM), (iv) numerical modeling using micromagnetic simulation, v) cell death via mechanical rotation.

2.1. Thin film deposition

The fabrication of the multilayered nanostructure is heavily depended upon the thin film deposition. Recent process using ultra-high vacuum have allowed for atomic level thin film deposition, which have been utilized within a wide range of engineering applications from surface science to nano-device fabrication. The thin film thickness and structure are primarily determined by the adsorption kinetics of the thin film atoms on the substrate surface. By controlling the mobility of deposited atoms on the surface, and interfacial energy of the film and substrate, we can control the diffusion and aggregation of atoms and the subsequent development of the film structure.

The deposition of a thin film on a surface can be classified into two main categories: chemical deposition and physical deposition. Chemical deposition is mainly involved with the exposure to one or more volatile chemical precursors, which react and/or decompose on the substrate surface to produce the desired film on the surface. Due to its inherent characteristic, chemical deposition is highly non-directional since the deposition is completely dependent upon the reaction of precursor with the exposed surface. On the other hand, the physical deposition is involved with the mechanical, electromagnetic, and thermodynamic energy to create the physical atom movement from target to substrate. This deposition method is directional since the deposition is dependent upon the physical atom movement from target to substrate.

The physical deposition process is governed by the vacuum environment of the deposition chamber due to 1) collision between atomic particles and residual air molecules, 2) oxidation of the substrate and the film due to impurities from residual air or gas molecules. In order to prevent such collision and oxidation, and to provide the optimal vacuum environment for deposition, we use ultra-high vacuum (UHV) system, with pressure less than 10^{-8} torr. This vacuum decreases the number of collisions between atomic particles and residual air molecules, thereby increasing the number of atomic particles that reach the target substrate. Furthermore, high vacuum levels minimize the risk of oxidation of the surfaces, which can lead to deviation in purity and chemical composition of the resulting film.

There are many different types of physical depositions, including thermal evaporation, sputtering, pulsed laser deposition, cathodic arc deposition and electro-hydrodynamic deposition. Among these various physical deposition methods, sputtering is of our particular interest. Sputtering is where target atoms are physically removed from the source due to collision of highly energized ions, such as Ar^{+}, which is accelerated by either

electric field within an ion gun (e.g. ion beam sputtering), or magnetic field within the magnetron gun (e.g. magnetron sputtering). Then target atoms physically travels through the deposition chamber and adsorb to the substrate. The repetition of this adsorption results in diffusion and aggregation of atoms that eventually develop into a thin film. Here, we focus on two sputtering methods for our fabrication: ion beam sputtering and magnetron sputtering.

2.1.1. Ion beam sputtering (IBS)

For metal deposition that requires high film quality, our group utilizes our home-built IBS system, which has simple and independent control of ion flux and ion energy by using a modified electron gun structure[39,40]. IBS consists of a main sputtering chamber and a small load lock, connected by a vacuum gate (Figure 2.1). The deposition chamber is constantly maintained at a vacuum level of 10^{-8} torr with cryo-pump at a working temperature of 12 K by helium compressor, following a water cooling cycle. The load lock is designed to help maintain the vacuum of the main sputtering chamber, so that sample can be transferred into/out of the main deposition chamber without changing the vacuum level of the main deposition chamber. A magnetic transporter located in the load lock chamber can transfer the sample into/out of the main deposition chamber through the gate, which separates the load lock chamber and main deposition chamber. In addition, the IBS system is equipped with a high intensity Kaufman ion source, which can generate a high-intensity focused ion beam directed at the target. The discharge chamber, both cathode and anode, and the ion optics (grids) are two major components of the ion source. Applying a high voltage field (250~1000 V) between the anode and cathode inside the discharge chamber creates an electrostatic field inside the ion source, confining electrons around a saddle point in the center of the chamber.

When the Ar gas flow is introduced from a gas cylinder to the ion source in a controlled manner, the Ar ions are generated by collisions with electrons. Then the ions are extracted from the discharge chamber and accelerated toward a target by the electric field emanating from the grids. As the ions leave the source, they are neutralized by electrons from a second external filament called the neutralizer. Then the neutralized atom flow bombards the target material, transferring the momentum between the ion and the target, which results in the target atom leaving the source target. The IBS system is preferred to other sputtering methods available in our facility for several reasons: 1) the directionality of deposition is superior due to control of energy and flux of ions, 2) high quality film with desired chemical ordering is ensured due to control of the deposition rate as low as 0.5Å/sec, which can be achieved by tuning the source beam voltage, 3) the deposition chamber pressure is constantly maintained with the presence of load lock, which minimizes the contamination/oxidation of the film.

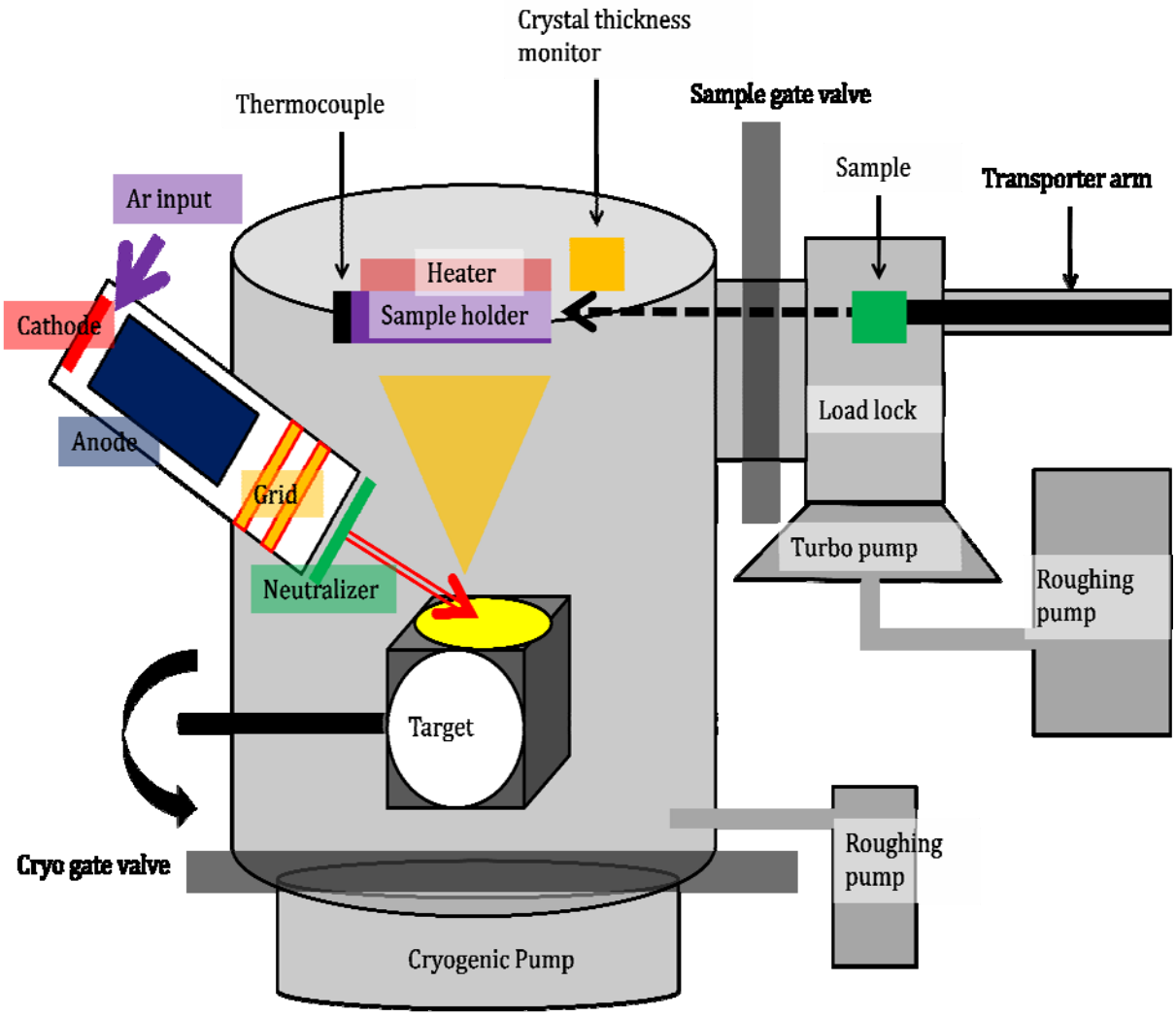

Figure 2.1. Schematic diagram of our ion-beam sputtering deposition system using Kaufman ion gun.

In our IBS system, the targets are placed at the focal plane of the ion source. The target holder has a cubic shape and can hold up to four different targets at one time. During sputtering, the targets can be changed by rotating the target holder. The substrate is placed at the ceiling of the main chamber facing downwards. During the thin film growth, the sputtered elements diffuse along the gas pressure gradient from the ion source to the substrate and get deposited. At the back of the sample holder is a vacuum sample heater, which heats the sample in the temperature range of 300K to 800K. Right next to the sample holder is a quartz

crystal microbalance (QCM) thickness monitor, which detects the resonant frequency shift of the quartz crystal due to the deposited thin film, and thus calculate the film thickness.

2.1.2. Magnetron sputtering

For oxide deposition, we utilize the magnetron sputtering system from AJA international, which uses a plasma produced and controlled by magnetron guns. Our magnetron sputtering system consists only of a main chamber with three 1-inch diameter magnetron guns. The deposition chamber is kept at atmospheric pressure, but it can be pumped down to $<5*10^{-6}$ torr with combination of mechanical pump and turbo pump to ensure a high quality deposition. In addition, our magnetron system is equipped with three magnetron guns for three different targets. Two guns are operated by RF source, and one gun is operated by DC source. The magnetron guns use magnetic and electric fields to confine the electron path, so the electron remains close to the surface of the cathode[41]. The cathode, here, is the target material to be sputtered and acts as the negative terminal, so that it provides an electron emitting surface [41]. The magnets in the magnetron guns are positioned to provide a closed path and form a high circulating current on the surface. This high circulating current results in high flux of electrons, causing high density of plasma due to electron-Ar atom collisions and ionization. The acceleration of Ar ions to the target surface cause the transfer of momentum between the ion and the target, which results in the target atom leaving the source target. The schematic diagram in Figure 2.2 clearly shows the fundamental mechanism of magnetron sputtering.

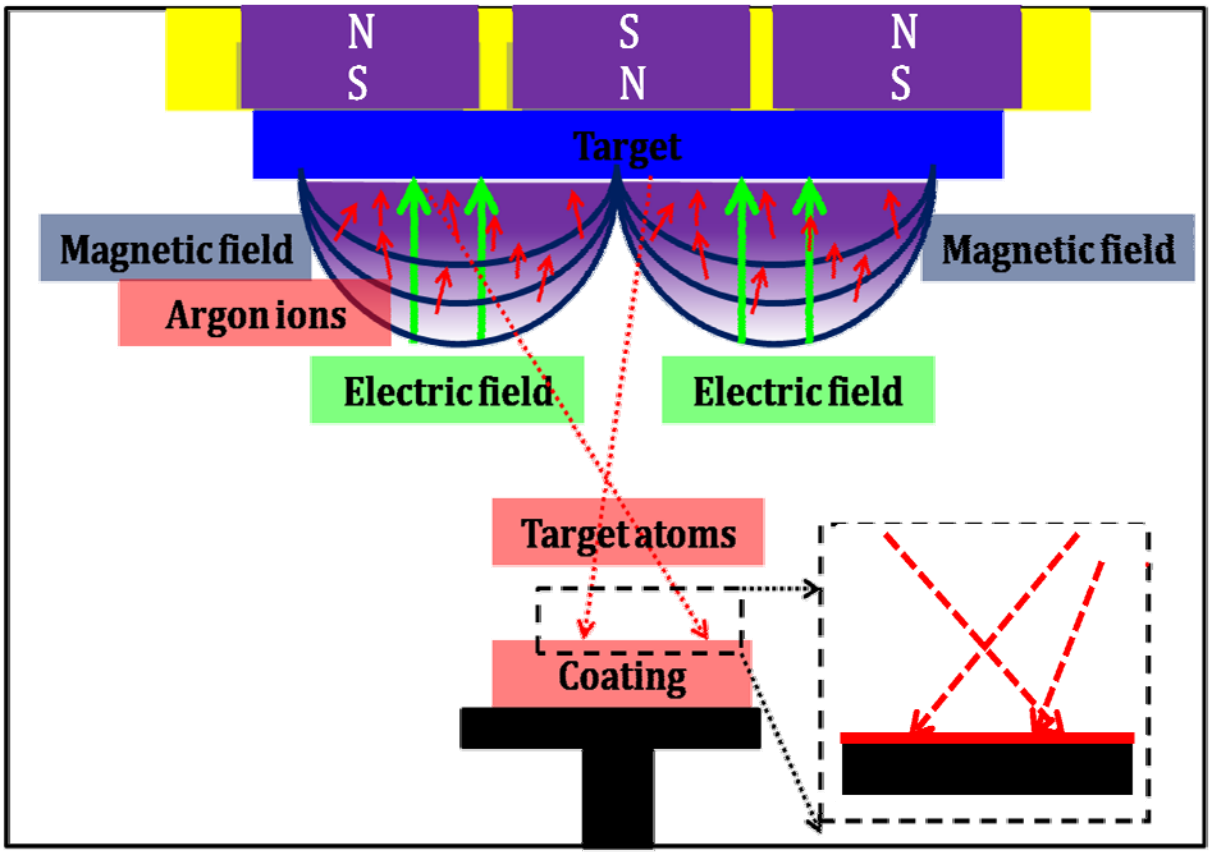

Figure 2.2. Schematic diagram showing the mechanism of magnetron sputtering: magnetic field produced by magnets will cause argon ions to bombard the surface of the target to transfer the momentum for the target atom to travel through the chamber for deposition

This mechanism, with the DC setup which locks the position of cathode as the target, is only suitable for conductive target because of the charge build-up. For an insulating target, a radio frequency (RF) potential is more appropriate. Therefore, RF potential may be applied instead of a DC potential for insulating target. When an RF potential, with a large peak-to-peak voltage, is coupled to an electrode, an alternating positive/negative potential appears on the surface. During part of each half-cycle, the potential is such that ions are accelerated to the surface with enough energy to cause sputtering. While on other half-cycles, electrons reach the surface to prevent any charge build-up, which enables insulator deposition.

The magnetron system is preferred to other sputtering methods available in our facility for two reasons: 1) since RF sputtering enables easy deposition of insulating material, oxide deposition is preferred on magnetron sputtering, 2) the operating power can be easily changed from 0~50W to ensure the slow to fast deposition rate depending on the applications.

2.2. Nanofabrication

Here, we discuss different nanofabrication techniques utilized in the thesis. In order to fabricate magnetic particles with the freedom of size, structure, shape and desired magnetic characteristics, a top-down lithographic method is highly preferred. Depending on the lateral size of the nano-features, different types of patterning techniques have been utilized. Here, we specifically discuss electron-beam lithography, and nanoimprint lithography.

2.2.1. Electron-beam lithography

Electron-beam lithography (EBL) is a patterning technique which uses an electron beam to pattern an array of elements. Specifically, a focused beam of electrons is used to draw custom shapes on a surface, covered with an electron-sensitive film called a resist[42]. As specific parts of the resist are exposed to the electron beam, the electron beam changes the solubility of the resist, enabling selective removal of either the exposed or non-exposed regions of the resist by immersing the film into the developer. As resolution of focused electron beam can be precisely controlled, electron beam lithography typically demonstrates <10 nm resolution[43].

In our thesis, poly (methyl methacrylate) (PMMA), a polymer material, which is sensitive to high-energy electrons, is used. PMMA normally comes in two molecular weights, 495K and 950K. For our samples, the 950K resist diluted in 3% anisole (950-A3) was used[44]. The PMMA 950 is spin coated on Si wafer at 3000 rpm for 45s to form a uniform thin film of ~100 nm thickness. The resist is soft baked on a hot plate at 180°C for 90s. Then the baked resist is brought to the University of Washington Nano Tech User Facility's (NTUF) FEI XL-30 scanning electron microscope for pattern writing. Here, electron beam is moved onto the PMMA coated substrate. The patterning is done by point-by-point process under the control of the Nanometer Pattern Generation System (NPGS) software. The schematic EBL process is shown in Figure 2.3. Then the pattern is developed for 70s, rinsed with Isopropyl alcohol (IPA) solution, and blow dried to remove the residue. Then, after the desired thin film materials were deposited, the sample was immersed in Remover-PG for lift-off[45].

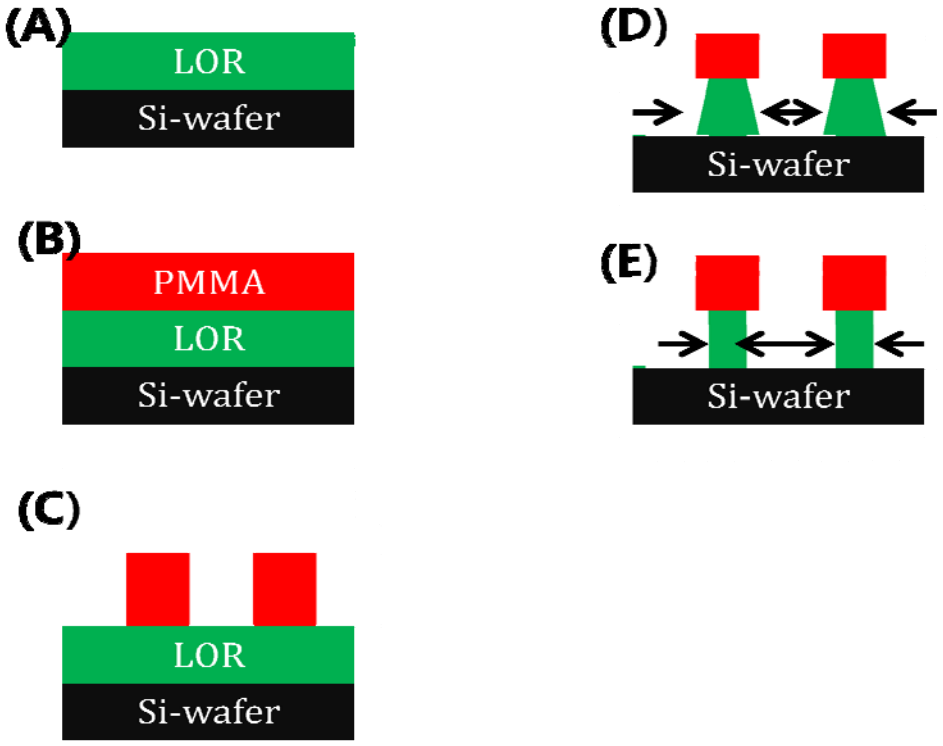

Figure 2.3. Schematic diagram of EBL process: (A) spin-coat of LOR under-layer, (B) PMMA coating on LOR under-layer, (C) Expose to EBL gun and develop to create the pattern, and (D), (E) selective wet-etching process to create the double layer undercut profile.

As mentioned earlier, EBL has one of the highest resolution capabilities among current lithographic techniques (<10 nm). However, it has posed critical difficulties since the focused electron beam cannot expose multiple elements simultaneously, which causes extensive writing time and high-cost issue. Therefore, EBL was only used to fabricate the original master mold for future nano-imprint lithography, which will be discussed in 2.2.2.

2.2.2. Nanoimprint Lithography

Nanoimprint lithography is a patterning technique which uses the mechanical

deformation of imprint resist and subsequent lift-off processes. Earliest forms of nanoimprint lithography proposed by Chou *et al*. utilizes thermoplastic polymers as resist materials[46-48]. In standard thermoplastic nanoimprint lithography, a thin layer of imprint resist is spin-coated on the sample substrate. Then the mold, which is predefined with topological patterns, is pressed onto the resist-coated substrate at elevated temperature (above glass transition temperature (T_g)) and pressure. The pattern on the mold is transferred onto the softened resist, and subsequently, when it is cooled down, the resist hardens. After the mold is separated from the sample, the patterned resist remains on the substrate. Since the initial idea of this technique was demonstrated, numerous variations of the nanoimprint lithography have been developed. Specifically, photo-nanoimprint lithography substitutes the required high temperature to harden the thermoplastic resist with UV-light to harden the resist and to transfer the pattern[49-54].

2.2.2.1. Hard-mold nanoimprint lithography

Nanoimprint lithography allows for a high-throughput and high-speed patterning of nano-arrays with high resolution at a low-cost. Initially, Chou *et al* relied on direct mechanical deformation of the resist material under a rigid silicon mold, which exhibited resolutions better than photolithography using UV light. In their proof of concept demonstration, they used silicon molds with 40~200 nm patterns, and press it onto a layer of thermoplastic resist (poly(methyl methacrylate) (PMMA)) spin-coated on the silicon substrate (see Figure 2.4 (A)). Furthermore, the residue of the resist was removed by a reactive ion etching (RIE) process to expose the compressed areas (Figure 2.4 (B), (C)). With such technique, Chou *et al*. achieved the best resolution of ~25 nm in patterning metal dots as

shown in Figure 2.4 (D) [47]. Although silicon mold-based nanoimprint lithography approaches have demonstrated excellent resolutions, significant challenges have risen, including difficulty in defect control of patterned area, inability to lift-off due to side wall deposition, and breakage of the mold through multiple imprint process.

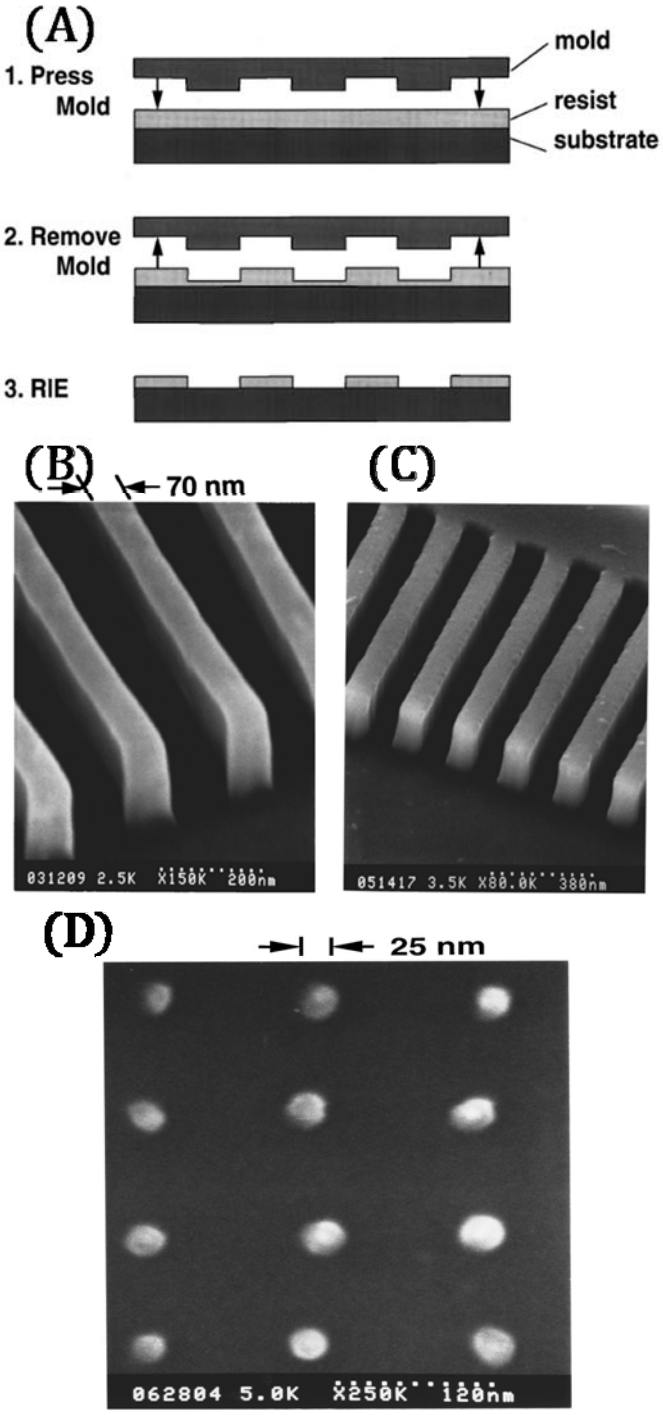

Figure 2.4. (A) Schematic diagram of nanoimprint lithography process: 1) imprinting using a mold to create a thickness contrast in a resist. 2) demolding, and 3) pattern transfer using anisotropic etching to remove residue resist in the compressed areas. (B) SEM micrograph of a perspective view of strips formed into a PMMA film by imprint. The strips are 70 nm wide and 200 nm tall with a high aspect ratio, a surface roughness less than 3 nm, and nearly perfect 90° corners. (C) SEM micrograph of the mold that was used to imprint the PMMA strips shown in Figure 2.4 (B). (D) SEM micrograph of 25 nm diameter and 120 nm period metal dots fabricated by imprint lithography and a lift-off process. Reproduced from [Chou, Stephen Y., Peter R. Krauss, and Preston J. Renstrom. "Nanoimprint lithography." Journal of Vacuum Science & Technology B 14.6 (1996): 4129-4133.] with permission of American Vacuum Society.

2.2.2.2. Soft-mold nanoimprint lithography

Soft-mold nanoimprint lithography has been developed to increase the yield and defect control in patterning. As mentioned, despite high resolution, hard-mold nanoimprint lithography has some problems that are associated with the inherent mechanical properties of the mold. The properties of patterned elements are easily influenced by extrinsic parameters, such as defects generated from the lithography process. For instance, submicron size particles in the resist solution that are not filtered out, can be transferred onto the substrate after spin-coating, causing the failure of lithography. The consequence of such defects has introduced significant issues for nanoimprint lithography, in particular, during mechanical contact between a stamp and a resist for the pattern generation. As a result, as mentioned in 2.2.2.1, the mold can be easily damaged. These issues introduce a dilemma: the mold should be used as much as possible for pattern generation, maintaining the integrity of the pattern, but the mold should not be considered as consumable for its high cost. Replication of the hard-mold can be made using a soft and flexible material, often polymer-based materials, such as PDMS, PFPE, ETFE, and PET, to resolve this dilemma. In addition to their low cost, their flexibility provides conformal and intimate contact between substrate and mold without the need for high external pressure. Also, their flexibility also makes them insensitive to particle contaminants in the resist, as they can locally deform around a particle without damaging the mold or affecting the lithography yield[37,38,55]. For their versatile characteristics and low cost, we focus on using soft-mold nanoimprint lithography in this thesis.

Conventionally, PDMS has been the prevalent material in use for soft-mold nanoimprint lithography. However it also has shown critical limitations for repeatable high

resolution imprint, caused by high porosity, low Young's modulus, and low reproducibility. Hence, many efforts have been made in developing molds maintaining flexibility and conformality, while securing high Young's modulus, and high durability against thermal and chemical environment. For instance, ETFE $(C_4H_4F_4)_n$ is a recently developed fluorinated polymer material which has been used as soft-molds for its high Young's modulus (> 10 Mpa), good mechanical strength, good chemical stability, and very low surface energy. ETFE was initially used to replace PDMS-based polymers for realizing cleaner and finer soft-mold nanoimprint lithography[51,56-58]. Furthermore, Barbero *et al* demonstrated ETFE stamps for thermal nanoimprint lithography[57]. Despite these advantages, the patterning resolution has been limited because of the crystallization of the polymer, which happens at ~100 nm scale. This crystallization has been observed in a previous study, showing the loss of the integrity of the imprinted features with <150 nm resolution[51].

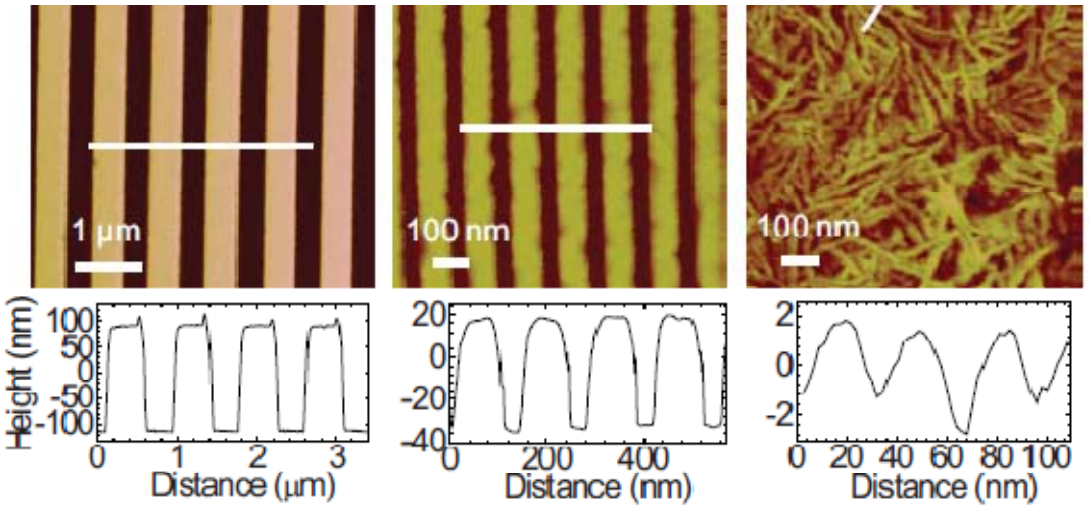

Figure 2.5. AFM topography images and profiles (along white lines) of ETFE molds with (A) 833 nm period. (b) 139 nm period, and (c) nominally flat mold showing needlelike crystals. Reproduced from [Dirk N., Stephen T. Meyers, and Douglas A. Keszler. "All-inorganic thermal nanoimprint process." *Journal of Vacuum Science & Technology B*28.4 (2010): 823-828] with permission of American Vacuum Society.

2.2.2.3. Nanoimprint lithographic fabrication of nanoparticles and release

The fabrication and release of the magnetic nanoparticles were carried out in several necessary steps: replication of nanoimprint stamp, fabrication of bi-layer resist undercut profile, nanoimprinting, anisotropic deposition, lift-off, and the release in solution (Figure 2.6).

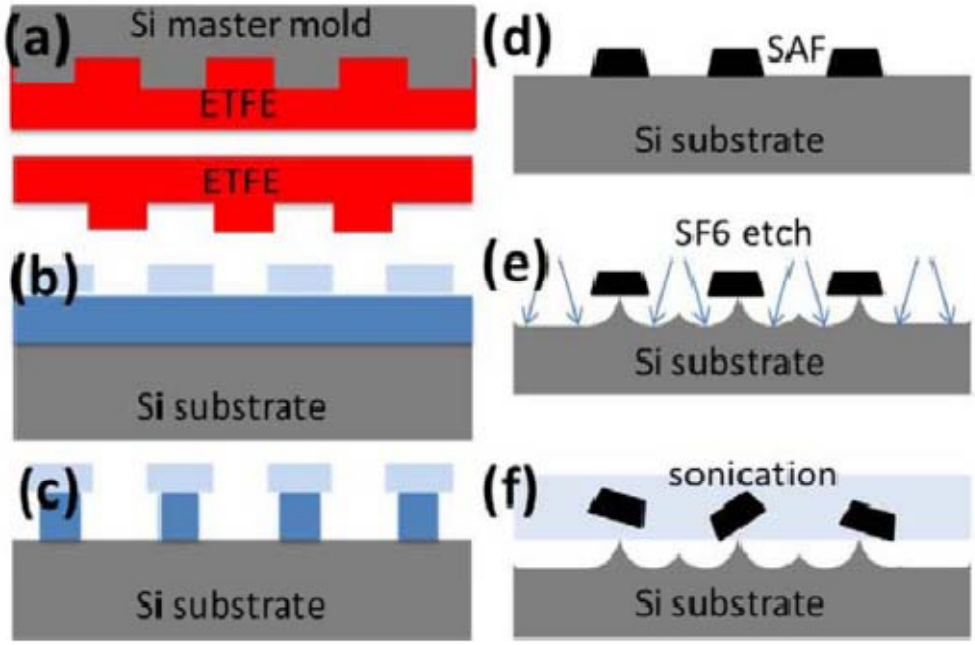

Figure 2.6: Representative diagram of the nanoimprint process used to fabricate disk-shaped magnetic nanoparticles[55]. Reproduced from [Zhang, Wei, Krishnan, Kannan M. "Direct release of synthetic antiferromagnetic nanoparticles fabricated by defect-free thermal imprinting." Journal of Applied Physics 111.7 (2012) 07B509] under the permission of AIP publishing.

The recipe used was based on the method developed by Zhang *et al.,* but adjusted for magnetite lift-off. For ETFE mold fabrication from the silicon master mold, we cleaned and sonicated a sheet of ETFE (DuPont Tefzel) with acetone and isopropyl alcohol for 5 minutes, blow-dried with nitrogen, and placed onto a clean Si-wafer for hot-embossing, The Si master

mold (150 nm ~ 350 nm size holes in hexagonal lattice form, 120 nm ~ 250 nm groove depth, and 300 nm ~ 700 nm period, from Lightsmyth Technologies) was placed on the ETFE sheet, then imprinted using a Nanonex NX-B 100 compact thermal nanoimprinter at 250°C and 450 psi, for 2 minutes. Next, we spin-coated a bi-layer resist, consisting of LOR 1 A (MicroChem) and NXR-1025 (Nanonex), and soft-baked each layer at 200°C and 150°C on a hot plate, respectively. After the bi-layer resist was ready, it was patterned with the ETFE mold using Nanonex NX-B100 imprinter (Figure 2.6 A). Large area hole arrays of the top layer were obtained. Next, we performed anisotropic oxygen plasma reactive ion etching (RIE) to remove the imprint resist residue, then we selectively etched LOR 1A layer of the patterned bi-layer resist to create an undercut. Then, we carried out the desired deposition process in order to fabricate array of magnetic nanoparticles. In Figure 2.6, we show a schematic example for the fabrication process of sombrero-shaped nanoparticles, which will be discussed in detail in Chapter 4 and Chapter 5.

2.3. Characterization

2.3.1. Crystal structure: X-Ray Diffraction

After NIL fabrication of lithographic elements, the chemical ordering and the crystal structure of fabricated film and elements must be confirmed. One of the most common instruments to characterize the thin film and/or element is X-ray Diffraction (XRD). X-ray is a type of electromagnetic radiation generated by bombardment of electrons onto a target material[59,60]. For XRD systems, an electron beam, accelerated by a high field, hits rotating Cu/Mo targets. When the high energy electron beam hits Cu or Mo targets, the electrons ionized out of the inner shell of the Cu/Mo (K shell), which introduces vacancies in the inner

shells. These inner vacancies are not energetically favorable , so the electrons try to fill the vacancies from the outer shell (L shell) to reach a more energetically favorable state. However, since the energies of K shell and L shell electrons are different, the energy difference is released in the form of an X-ray. For Cu (KαK, this X-ray has a wavelength of 1.54 Å, which is equivalent to 8 KeV. For Mo (Kαo, the X-ray has a wavelength of 0.8 Å, which is equivalent to 14KeV. Since this wavelength is comparable in length to the atomic periodicity in most crystals, X-ray can be utilized for probing the atomic structure.

For XRD, the conventional method that we use to characterize the crystal structure and chemical order is the θ-2θ scan. Here, an incident X-ray on a sample is scattered by parallel planes of atoms, where each plane reflects 10^{-5} to 10^{-3} of the incident radiation, depending on the scattering power. Diffraction effects are observed when the distance between the sources (plane of atoms) is comparable to the wavelength of the incident x-rays. The diffracted radiation has a strong angular dependence because it is produced by constructive and destructive interference. Constructive interference occurs when the phases of the scattered waves from atoms in parallel planes differ by an integer number of wavelengths, and a peak in the diffraction pattern is formed. Destructive interference results in low intensity in the diffraction spectra.

The position and intensities of the peaks are used to identify the crystal structure and chemical order of the material. For a given set of lattice planes with an inter-plane distance of d, the diffraction peak location can be calculated using *Bragg's law*.

$$n\lambda = 2d\sin\theta \qquad (2.3.1)$$

Here, n is the order of wavelength, λ is the wavelength of incident electron beam, which is 1.54 for Cu target and 0.8 for Mo target, and d is the spacing between planes in the atomic

lattice. θ is angle of incident beam. Figure 2.7 shows the setup of conventional XRD in this Bragg-Brentano geometry. The detector is always at the angle of 2θ from the incident beam, which gives the conventional XRD θ-2θ scan.

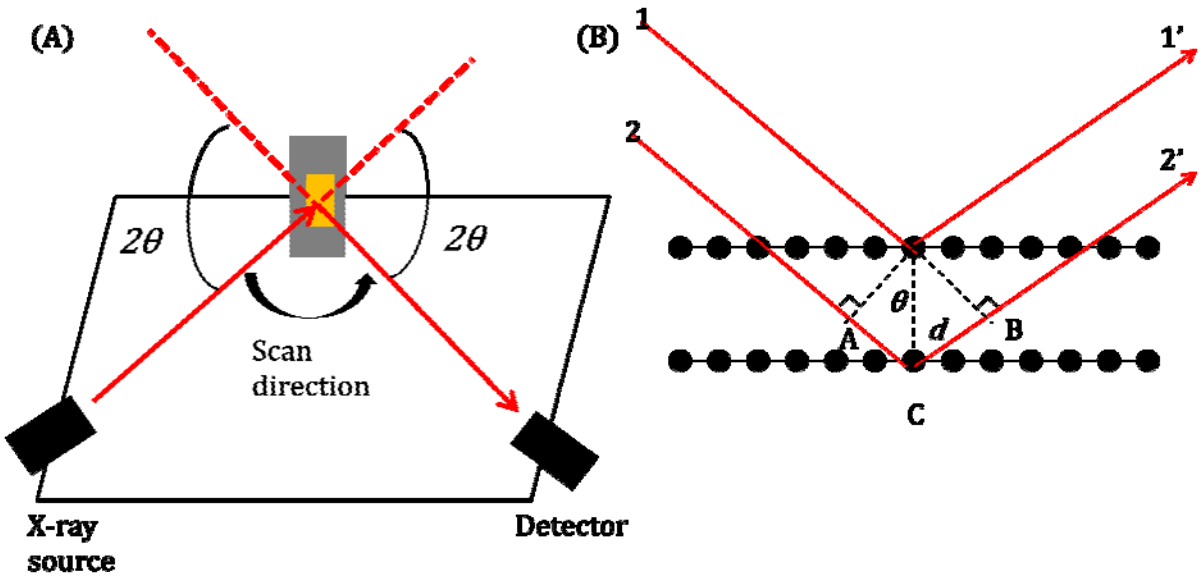

Figure 2.7. XRD of 'θ-2θ scan' geometry and the schematic diagram showing Bragg's law. Here, 1(1') and 2(2') are two parallel incident beams.

2.3.2. Magnetic reversal behavior: vibrating sample magnetometer (VSM)

Magnetic reversal behavior is characterized using vibrating sample magnetometer (VSM). The VSM is based on Faraday's induction law, which states that a changing magnetic flux will produce an electric voltage in a closed current loop. The change in electric voltage can be measured and further correlated to the changing magnetic flux. During VSM measurements, the sample, driven by a motor, is vibrated in sinusoidal motion, while the set of electromagnets, placed on either side of the sample, generate the uniform magnetic field. The electrical signal resulting from the vibration of the sample in a magnetic field can be read

by a pickup coil. The electric signal has the same frequency as the vibration and its amplitude will be directly proportional to the magnetic moment, vibration amplitude, and the relative position to the pickup coil. In our lab, there are two instruments which can carry out those magnetic reversal measurement: the Lake Shore Model 7300 commercial VSM equipment can measure the room temperature magnetic moment of the sample from 10^{-5} emu to 10^{4} emu, and VSM installed in a Physical Property Measurement System (Quantum Design Inc) can measure magnetic reversal behavior of the sample in various temperatures, ranging from 10K to 480K.

2.3.3. Magnetic remanence state characterization: magnetic force microscopy (MFM)

Scanning probe microscopy (SPM) obtains images of a surface by physically scanning the sample surface using a fine tip. Figure 2.8 illustrates the major components of a typical SPM. There is a very fine tip with a typical end radius of several nanometers attached to the cantilever. The cantilever is held by a piezoelectric transducer (PZT). Monochromatic laser is reflected from the back of the cantilever onto a position sensitive quadrant photo diode. As the cantilever and tip is scanned over the sample surface, the cantilever bends and the laser beam reflected from its surface is deviated due to the deflection of the cantilever, which is detected on the quadrant photo diode. The signals from the photo diode are used to control the PZT moving the cantilever to maintain a constant bending of the cantilever which return the reflected beam's point of incidence on the quadrant photo diode to the center. This ensures that the force exerted by the tip on the surface remains constant and that the tip follows the surface topography.

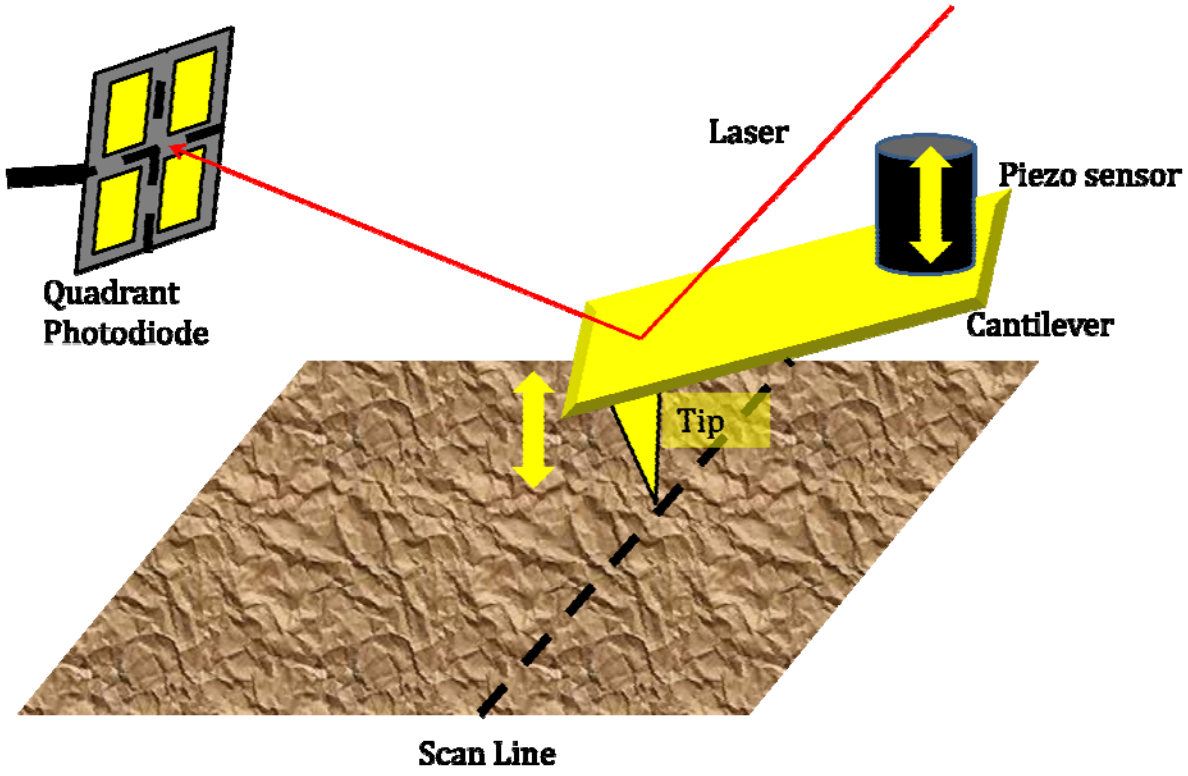

Figure 2.8. Schematic diagram of the Scanning Probe Microscopy showing the feedback-control system

Here, we will discuss two different modes of operation of a scanning probe microscope: 1) atomic force microscope (AFM) and 2) magnetic force microscope (MFM). With AFM, we are able to characterize the topography of the sample surface through the mechanism described above. For AFM, there are two different kinds of scanning methods: static or contact methods, or dynamic or tapping methods. In static or contact methods, the tip is in direct contact with the sample surface during the scan, but in dynamic or tapping methods, the tip is oscillating above the surface during the scan. If the tip is far from the surface, the magnitude of the vibration is its free air magnitude. However, as the tip approaches the surface, it starts to react to the force from the surface, which can be either attractive or repulsive. The vibration magnitude of the tip deviates from the free air value depending upon the distance between the tip and the surface. However, by fixing the distance

between the tip and the surface, we can set the vibration magnitude to a certain value.

For this thesis, we mainly use the tapping/dynamic method than contact/static method due to two reasons: 1) tapping/dynamic method makes minimum amount of contact between tip and the sample surface, which causes minimum wear/degrade of the tip during the scan, 2) minimum amount of contact also minimizes sample degradation. An exemplary AFM image using tapping/dynamic method is shown in Figure 2.9.

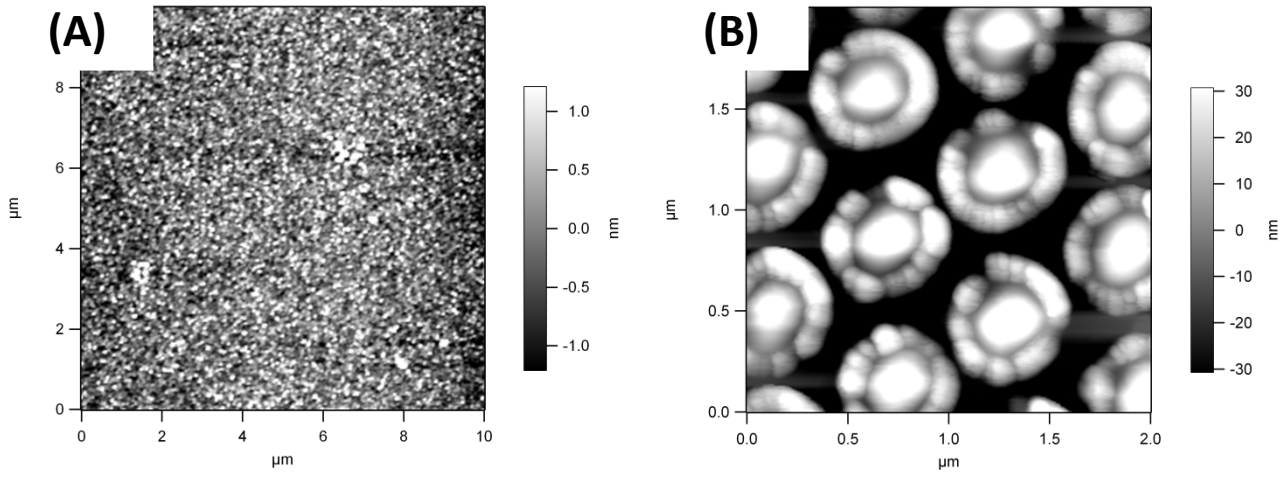

Figure 2.9. Exemplary AFM image using tapping/dynamic method of Fe_3O_4-magnetite thin film (A), and Fe_3O_4-magnetite sombrero-shaped nanoparticles

For magnetic force microscopy (MFM), the tip is coated with a thin layer of magnetic material such as Co, CoPtCr, or CoCr. To isolate the magnetic signal for the sample surface from other signals, the tip goes through the normal topographical scan (tapping/dynamic method) and interleave scan, which is also called "lift-mode" or "nap mode". Interleave scan is the secondary scan after the normal topographical scan with certain fixed distance (delta height) above the sample surface. This delta height prevents any short

but strong interaction with sample surface (i.e. Van der Waals Force, Capillary wetting interaction) (Figure 2.10). During the interleave scan, the tip is essentially following the topographical trace, but with delta heights, which allows the magnetic tip to detect the gradient of the magnetic field in a direction normal to the surface of the sample. More specifically, as the tip scans over the sample surface, it encounters a non-uniform stray field from the surface of the sample. Then, the force is exerted on the tip.

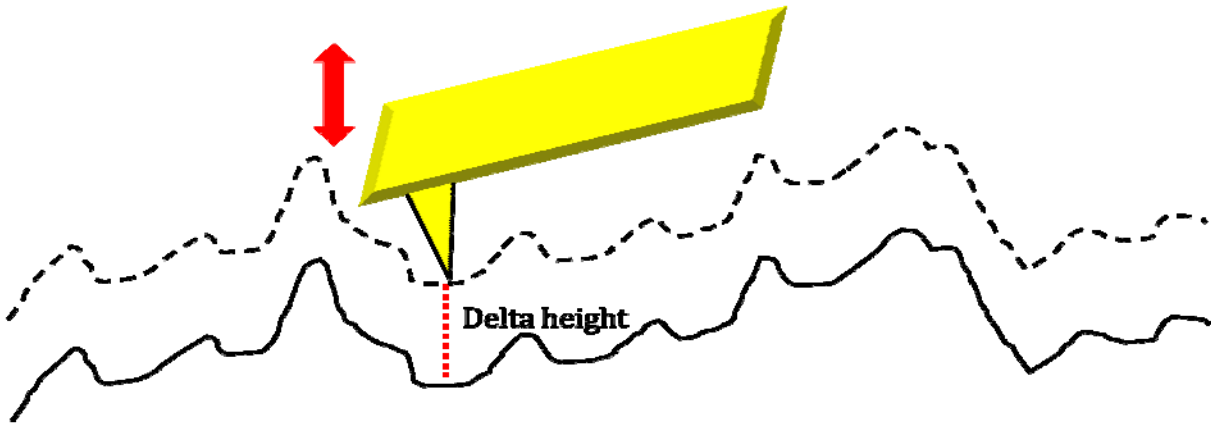

Figure 2.10 Schematic diagram of the interleave mode for magnetic force microscopy: the tip scans the surface twice, the first scans the topography, and second time, the tip is lifted up with a certain height (delta height) to detect the force caused by the magnetic interaction.

However, since the MFM uses a magnetized tip to detect the magnetic signal from the sample, its spatial resolution is heavily dependent upon the tip diameter. Most of the MFM tips are coated with magnetic films, such as CoCr or CoPt onto the regular AFM silicon tip. The magnetic coating material and its thickness is dependent upon whether the tip is measuring a strong magnetic element or a weak magnetic element surface. For a strong magnetic element, we typically use high-moment MFM tip, which can detect a strong signal, due to the thicker coating (100 nm), and for a weak magnetic element, we typically use a

low-moment MFM tip, which has a higher resolution (15 nm). In this thesis, Fe_3O_4-magnetite has a considerably weak magnetic signal due to its ferrimagnetism, so we use low-moment MFM tip.

2.4. Magnetic modeling: LLG micromagnetic simulation

Micromagnetic simulation is used to numerically predict the magnetic domain configuration and magnetic reversal process in the micron and nanometer scale. Here, micromagnetic simulation basically solves for the magnetization, *M,* as a function of position (x,y) with the energy minimum using dynamic LLG differential equation with the given initial state and boundary conditions. Here, we discuss the fundamental principle of micromagnetic simulation.

2.4.1. Continuum hypothesis

In order to describe the magnetic configuration and behavior of a system, the classical *continuum hypothesis* is utilized in the simulation. This hypothesis simplifies the problem by neglecting quantum mechanical effects, and only considers classical physics in a continuum description of a magnetic material. Here, we assume the magnetization to be continuous vector field, $\mathrm{M}(\vec{r})$, with $\vec{r}$ representing the position vector inside the material, which leads to

$$\overrightarrow{\mathrm{M}}(\vec{r}) = \mathrm{M_s}\ \overrightarrow{\mathrm{m}}(\vec{r}) \tag{2.4.1}$$

$$\overrightarrow{\mathrm{m}} \cdot \overrightarrow{\mathrm{m}} = 1 \tag{2.4.2}$$

$\mathrm{M_s}$ is the saturation magnetization of the material. The basic micromagnetic approach

is to formulate the energy in terms of a continuous magnetization vector field, and to minimize the energy in order to determine static magnetic configurations. The relevant energy terms are discussed below:

2.4.2. Exchange energy

Exchange energy is caused by the interaction between two nearest-neighboring spins in a microscopic model, which can be expressed as following:

$$W_{ij} = -2\ J\ \vec{S}_i \cdot{*}\vec{S}_j \tag{2.4.3}$$

J is the exchange constant, and $\vec{S}_i$, $\vec{S}_j$ is the spin angular momentum of spin *i* and *j*, respectively. We assume that the angle θ_{ij} between spins S_i and S_j is very small.

$$\vec{S}_i \cdot \vec{S}_j = S^2\, cos\theta_{ij} = S^2\,(1 - \tfrac{1}{2}{\theta_{ij}}^2) = S^2\left(1 - \tfrac{1}{2}\left|\vec{m}_i - \vec{m}_j\right|\right)^2 \tag{2.4.4.}$$

Spin i and spin j have identical magnetic moments, so $S = |S_i| = |S_j|$. In the continuum hypothesis, we assume that $\vec{m}_i$ can be estimated with continuous function $\vec{m}(r)$ of position.

$$\vec{m} = \alpha\hat{\imath} + \beta\hat{\jmath} + \gamma\hat{k} \tag{2.4.5}$$

We can transform the vector expression $\left|\vec{m}_i - \vec{m}_j\right|$ in terms of spin vector $\vec{s}_j$, which is the position vector of spin j, with respect to spin i. Therefore,

$$\left|\vec{m}_i - \vec{m}_j\right| = |(\vec{s}_j \cdot \nabla)\vec{m}_i\,| \tag{2.4.6}$$

We can express the excess exchange energy due to spin i and spin j.

$$W_{ij} = J\ S^2\left|\vec{m}_i - \vec{m}_j\right|^2 = J\,S^2|(\vec{s}_j \cdot \nabla)\vec{m}_i\,|^2 \tag{2.4.7}$$

Then we can express the excess exchange energy per unit volume with sum of the excess exchange energy due to spin i and spin j.

$$w_e = \frac{1}{2}\, nJS^2 \sum_i^j \left|(\vec{s}_j \cdot \nabla)\vec{m}_i\right|^2 \quad (2.4.8)$$

Finally, the excess exchange energy within the material is the volume integral of the excess exchange energy per unit volume.

$$E = \int w_e \, dV \quad (2.4.9)$$

2.4.3. Magnetocrystalline anisotropy energy

Magnetocrystalline energy is an interaction energy caused by the crystal structure of a material. Here, we discuss the volume magnetocrystalline anisotropy for uniaxial and cubic crystals. In both cases, we assume a crystal symmetry to decrease the number of coefficients, and eliminate all terms, except the first two terms, which dominate.

For an uniaxial crystal (easy axis in y), energy density, w_a, can be estimated using direction cosines of vector M with respect to the three principle axis: α, β, γ

$$w_a = K_1 (1 - \beta)^2 + K_2 (1 - \beta^2)^2 \quad (2.4.10)$$

For a cubic crystal, the energy density can be estimated using the direction cosines of vector M, with respect to the three principle axis: α, β, γ

$$w_a = K_1 (\alpha^2\beta^2 + \beta^2\gamma^2 + \alpha^2\gamma^2) + K_2 (\alpha^2\beta^2\gamma^2) \quad (2.4.11)$$

The magnetocrystalline anisotropy energy is simply the volume integral of the energy density which is

$$E = \int w_a dV \quad (2.4.12)$$

2.4.4. Magnetostatic energy

The magnetostatic energy comes from the demagnetization field within the material without any external field. The magnetostatic or demagnetizating field H_d is governed by

$$\nabla \times \vec{H}_d = 0 \tag{2.4.13}$$

$$\nabla \cdot \vec{B} = \nabla \cdot (\vec{H}_d + \vec{M}) = 0 \tag{2.4.14}$$

Here, $\vec{B}$ is an induction vector, which satisfies the following relationship with field and magnetization

$$\vec{B} = \mu_0(\vec{H}_d + \vec{M}) \tag{2.4.15}$$

The demagnetizing field, $\vec{H}_d$,, can be derived from negative gradient of the scalar magnetic potential,

$$\vec{H}_d = -\nabla \cdot \phi \tag{2.4.16}$$

From the equation above, following equations can be derived within the magnetic material, and outside of magnetic material

$$\nabla^2 \cdot \phi_{in} = \nabla \cdot \vec{M} \tag{2.4.17}$$

$$\nabla^2 \cdot \phi_{out} = 0 \tag{2.4.18}$$

These two conditions lead to the boundary conditions at the surface of the magnetic material,

$$\phi_{in} = \phi_{out} \tag{2.4.19}$$

$$\frac{\partial \phi_{in}}{\partial n} = \frac{\partial \phi_{out}}{\partial n} + \vec{M} * \hat{n} \tag{2.4.20}$$

$\hat{n} =$ the surface normal and $\frac{\partial \phi}{\partial n}$ is the derivative of the magnetic potential, with respect to the distance from the surface.

From these equations, we can assume that the magnetization within the body forms a big magnetic dipole within the magnetic material.

During the process of magnetizing the sample, the work has to be done to overcome the effect of this internal field, which is so called demagnetizing field. If we assume that the demagnetizing field is uniform throughout the body, we can estimate the energy of magnetostatic energy to be

$$E = -\frac{\mu_0}{2} \int \vec{M} \cdot \vec{H}_d dV \quad (2.4.21)$$

2.4.5. Zeeman energy

Lastly, the Zeeman energy term can be described as the potential energy of a continuous magnetic moment distribution, subject to external field $\vec{H}_e$.

$$E = -\mu_0 \int \vec{M} \cdot \vec{H}_e dV \quad (2.4.22)$$

2.4.6. Dynamic LLG equation

With energy terms described above, we calculate the magnetic microstructure at equilibrium. Here, we assume that the total energy involved in this system is the sum of four energies that were mentioned above: exchange energy, magnetocrystalline energy, magnetostatic energy, and Zeeman energy. At equilibrium, the energy does not change over time. In order to numerically reach the equilibrium, we calculate the magnetic microstructure simultaneously using LLG equation. LLG equation is listed as following:

$$\frac{\partial \vec{M}}{\partial t} = -\gamma \vec{M} \times \vec{H}_{eff} + \frac{\alpha}{M_s} \vec{M} \times \frac{\partial \vec{M}}{\partial t} \quad (2.4.23)$$

Here, $\vec{H}_{eff}$ is an effective field derived from total energy of the system, which can be defined as

$$\vec{H}_{eff} = \frac{dE_{tot}}{d(\mu_0 M_s(\alpha(\vec{r}))} \quad (2.4.24)$$

In order to make instantaneous change of magnetization $(\frac{\partial \vec{M}}{\partial t})$ to be zero, $\vec{M}$ X $\vec{H}_{eff}$ (magnetic torque) has to be zero. Geometrically, in order for the cross product to be zero, $\vec{M}$ and $\vec{H}_{eff}$ has to be parallel. However, LLG equation is a non-linear differential equation, which makes it extremely difficult to find an exact analytical solution. Therefore, we iterate discrete time steps in order to calculate the convergence minimum (near zero solution) for the magnetization configuration.

In this thesis, the micromagnetic simulation was performed using a commercial software package, LLG micromagnetic simulator, which was developed by M. R. Scheinfein [61,62]. By using this program, we were able to simulate the behavior of full 3-dimensional magnetic objects. However, we have to specify few basic parameters: 1) geometry and material properties of the magnetic element, 2) cell dimensions (individual spin dimensions), which is comparable to exchange length, 3) initial state and boundary conditions, 4) convergence minimum which is called as "equilibrium".

In LLG micromagnetic simulation, before any calculations are carried out, the magnetic object is discretely divided into small arbitrary entity called cells. The size of the cell must be small enough so that it has to represent an individual micromagnetic spin within the magnetic material . Therefore, the cells must be exchange coupled with each other, which basically decides the cell size to be comparable to exchange length[63]. The exchange length gives an estimation of the characteristic dimension on which the exchange interaction is dominant. For our experiments, the cell size is defined to be 2 nm.

2.5. Cell death via mechanical rotation

In this thesis, we discuss cell death via mechanical rotation of magnetic particles. As mentioned in section 1.4, previous studies have demonstrated the potential of effective cell death via mechanical force induced by the rotation of the disk-shaped particles. However, the bio-compatibility of the disk-shaped particles that were used is not suitable for real life application. Therefore, here, we also use the idea of magnetic nanoparticles in order to create mechanical movement and force required to cause cell death. In order to do so, we use biocompatible material (Fe_3O_4-magnetite) without magnetic remanence via synthetic antiferromagnetic configuration in order to demonstrate the mechanical rotation, and further cell death via mechanical force.

2.5.1. Mechanical Rotation

Figure 2.11 shows the schematic diagram of our setup to confirm the mechanical rotation of magnetic nanoparticles in the solution. In our setup, a laser with a wavelength of 512 nm is shone through the vial between electromagnets, which induce the A.C magnetic field. Then, the transmitted laser is detected by the photodiode detector. In theory, the particles in absence of external magnetic field should exhibit Brownian motion, which will not transmit the laser. On the other hand, when magnetic field is present, magnetic nanoparticles would rotate to align itself to the external magnetic field due to shape anisotropy of the disk. As the intensity of external magnetic field increases, the intensity of the transmitted laser should increase. Figure 2.11 shows the simple schematic diagram of particles in the absence of magnetic field, the diagram of particles in the presence of magnetic

field, and the graph showing the light intensity depending on magnetic field intensity.

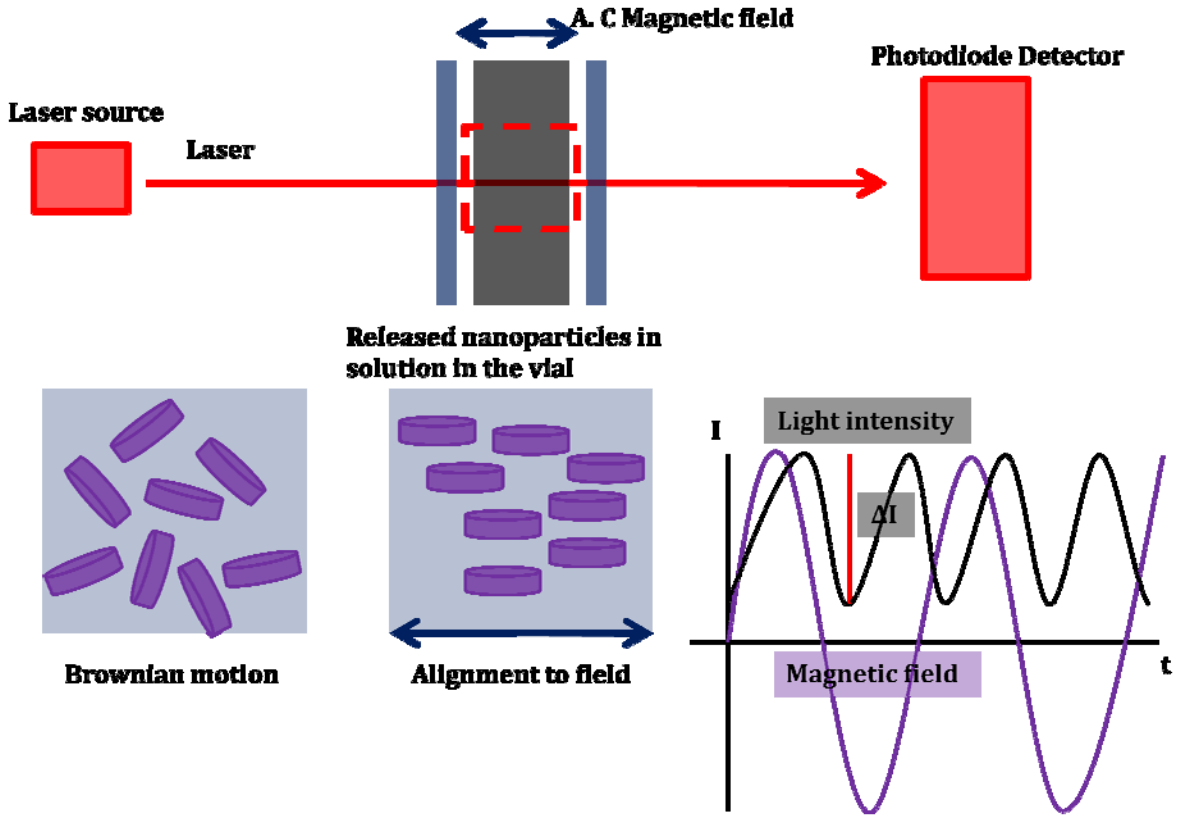

Figure 2.11. (upper) Schematic diagram of our setup to confirm the rotation of the magnetic nanoparticles in solution using the laser, which goes through the vial with magnetic nanoparticles. Then the transmitted laser will be detected with photodiode detector. (lower) Schematic diagram of orientation of magnetic nanoparticles in solution with/without external magnetic field.

2.5.2. HeLa cell culture

Here, we use HeLa cell in our experiment for its unlimited growing capacity. HeLa is a cell type in an immortal cell line, which is derived from cervical cancer cells. Unlike a normal cell, which naturally degrades after certain time, HeLa cell can grow without limit, which makes them desirable for our experiment. Cell culture is done using our own cell culture lab (Figure 2.12). In order to grow the cells, we use DMEM media in 37.5C with a 5%

carbon dioxide environment incubator. We follow general cell culture protocols:

Figure 2.12. Images showing key instruments required for cell culture process: (A) incubator showing the temperature and carbon content, (B) incubator shelf, (C) bio-hood facility equipped with UV cleaning system, and (D) hot bath for thawing process.

1) Thaw the frozen cell line in a hot bath (15 min) and put them into the flask with 10 ml of media to start the growth.

2) Meanwhile, change media every 2 days to prevent cell from perishing.

3) If the cell line expands to 70% of the flask then split those cell lines into 2~3 flasks in order to give space for them to grow.

4) After we have sufficient number of cells, count the cell and adjust the cell numbers to the appropriate value for desired cell experiment (~ 0.1 million cells per well)

5) Divide prepared cells into different wells and wait 3 hours for them to attach to the surface of the well and stablize.

After we are done preparing the cells for experiment, we divide them into four groups: 1) control live cell group without magnetic particles, 2) cell group with magnetic particles but without external magnetic field, 3) cell group with magnetic particles and external magnetic field, 4) pure media.

This process is specifically handled with care due to the high potential of contamination from HeLa cells. HeLa cells tend to cross contaminate other cells via any sort of medium (residue on the hood, residue in the pipette, residue on any instrument within the bio-hood) due to its robust and contagious nature.

Chapter 3

Fe_3O_4-magnetite thin film and Fe_3O_4-magnetite based synthetic antiferrimagnetic (SAF) configuration

3.1. Introduction

In § 2.1. the thin film deposition methods were described in detail. Furthermore, in § 2.3, various characterization methods to study and confirm the iron oxide phase were also presented. While there have been numerous previous studies which have investigated the chemical, structural, and magnetic properties of Fe_3O_4-magnetite, it is necessary for us to meticulously calibrate our deposition process and confirm a reliable and reproducible selective fabrication of mono-phase Fe_3O_4-magnetite. The Fe_3O_4-magnetite phase is essential for biomedical application, which will be discussed in Chapter 6 in detail. In summary, in order to utilize the iron oxide nanoparticles for biomedical applications, it is critical to selectively fabricate Fe_3O_4-magnetite, which has demonstrated adequate magnetic properties and excellent biocompatibility. Furthermore, as mentioned in Chapter 1, nanoparticles with SAF configuration is necessary in order to overcome the size limitations and avoid agglomeration. Theoretically, SAF configuration would allow the particles to have near-zero remanent magnetization and near-zero coercivity due to antiparallel orientation of the magnetization between ferro/ferrimagnetic layers.

Here, we discuss the process of fabricating Fe_3O_4-magnetite thin films, confirm the phase, and study the magnetic properties. Furthermore, we proceed to fabricate Fe_3O_4-

magnetite based SAF thin film with varying number of magnetic layers in order to study the dependence of magnetic properties on number of magnetic layers.

3.2. Fe_3O_4-magnetite thin film

3.2.1. Fe_3O_4-magnetite thin film deposition:

Fe_3O_4 thin films on silicon substrate were deposited by RF magnetron sputtering ($P_{base} < 5*10^{-6}$ torr). Typically, in a sputtering process, it is difficult to control the oxidation state and obtain phase pure magnetite. Therefore, the critical step is to calibrate the argon partial pressure and deposition rate/power to neither over-oxidize nor under-oxidize from Fe_3O_4 source. Silicon substrates were cleaned with acetone and isopropyl alcohol (IPA) to remove any residual particles on substrate. Then the silicon substrate was placed in the deposition chamber, followed by deposition at ~7.0 mtorr with RF power at 50W. In order to ensure sufficient signal for both XRD and Raman spectroscopy from the resultant thin film, the film thickness was > 100 nm. After deposition, the thin film was characterized with XRD and Raman to confirm Fe_3O_4 composition.

3.2.2. XRD characterization of Fe_3O_4-magnetite thin film

XRD have been conventionally used to characterize the specific phase or crystal structure of the thin film. Iron oxide exists in three different structures, corresponding to different iron oxidation states: FeO-wustite, Fe_2O_3-maghemite/hematite, and Fe_3O_4-magnetite. Because Fe_3O_4-magnetite and Fe_2O_3-maghemite both have inverse spinel structures, XRD characterization is not sufficient to directly confirm the phase of the thin film as Fe_3O_4-

magnetite or Fe_2O_3-maghemite due to common overlapping peaks. Figure 1.5 demonstrates XRD *θ-2θ* scan (Cu Kα) of different forms of iron oxides: Fe_2O_3-maghemite/hematite and Fe_3O_4-magnetite[18]. As shown, hematite can be easily differentiated from maghemite and magnetite, even with simple XRD *θ-2θ* scan, since the peak location for characteristic peaks is completely distinct: hematite (104) peak is located at 32°, but maghemite and magnetite peaks are 30.5°, 35° and 36°.

In order to characterize the fabricated thin film from our magnetron sputtering method, XRD *θ-2θ* scan was carried out using Bruker D8 Focus XRD in our department. The XRD result of our fabricated thin film using Cu $K\alpha_1$ presumed to be Fe_3O_4 demonstrates potential maghemite/magentite peaks at ~30.5°, ~34.7° and ~35.2° (Figure 3.1) with monochromater, which eliminate the possibility of hematite. Even though we can conclude that the sample is not hematite based on the XRD characterization, the thin film needs to be further characterized via a different characterization method in order to distinguish whether the thin film is composed of Fe_3O_4-magnetite or γ-Fe_2O_3- maghemite, or both.

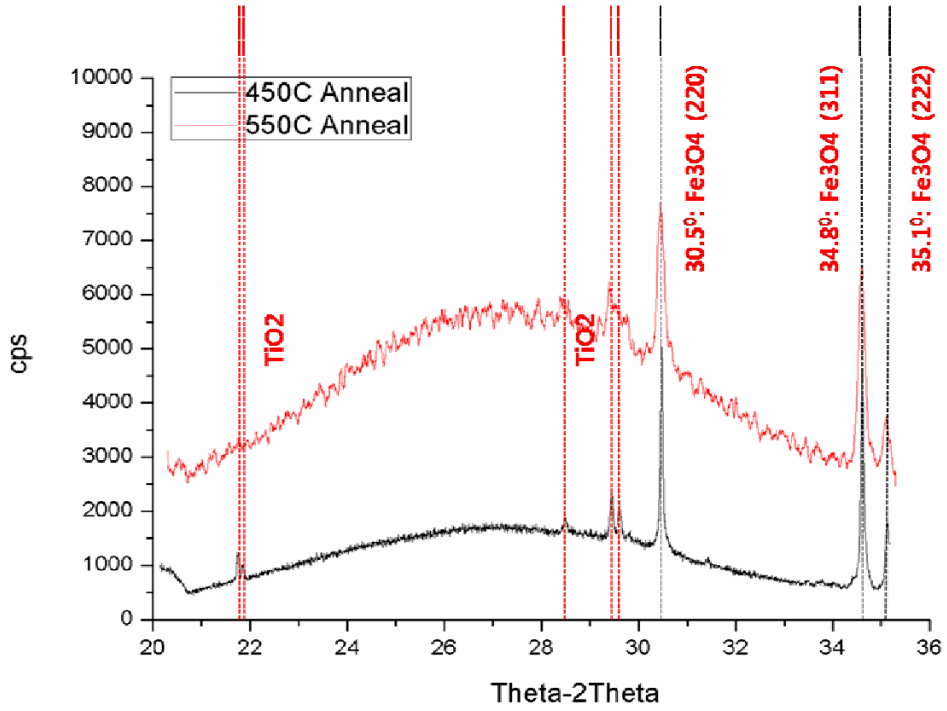

Figure 3.1. XRD spectra of fabricated thin film annealed at 450°C and 550°C, showing characteristic peak at 30.5°, 34.8° and 35.1°. The XRD *θ-2θ* scan was carried out using D8 focus XRD available at our department. This XRD is operated using Cu Kα radiation and normally operated using monochromater.

3.2.3. Raman spectroscopy characterization of Fe_3O_4-magnetite thin film

Once the possibility of a hematite phase has been ruled out, Raman spectroscopy can be used to differentiate between Fe_3O_4-magnetite from γ-Fe_2O_3- maghemite. Previous Raman spectra on different phases of iron oxides have clearly shown the difference in characteristic peaks for α-Fe_2O_3- hematite, γ-Fe_2O_3- maghemite, and Fe_3O_4-magnetite (Figure 3.2). To be more specific, Fe_3O_4-magnetite spectra shows two distinctive peaks of Raman shift (cm^{-1}): a sharp peak at 650 cm^{-1} with a smaller peak at 570 cm^{-1}. These peaks are clear indications of Fe_3O_4-magnetite that are not observed with any other phases of iron oxides.

Figure 3.3 shows a Raman spectra of our thin films, which has the characteristic peak at ~650 cm^{-1} and smaller peak at ~570 cm^{-1}. From the Figure 3.2, which both shows the

maghemite mono-phase (Figure 3.2 (B) and maghemite with magnetite (Figure 3.2 (A)), we can safely eliminate the possibility of maghemite presence within our fabricated film. Combining the results from XRD and Raman spectroscopy of our fabricated thin film, we can safely conclude that our samples deposited via magnetron sputtering are composed of mono-phase Fe_3O_4-magnetite.

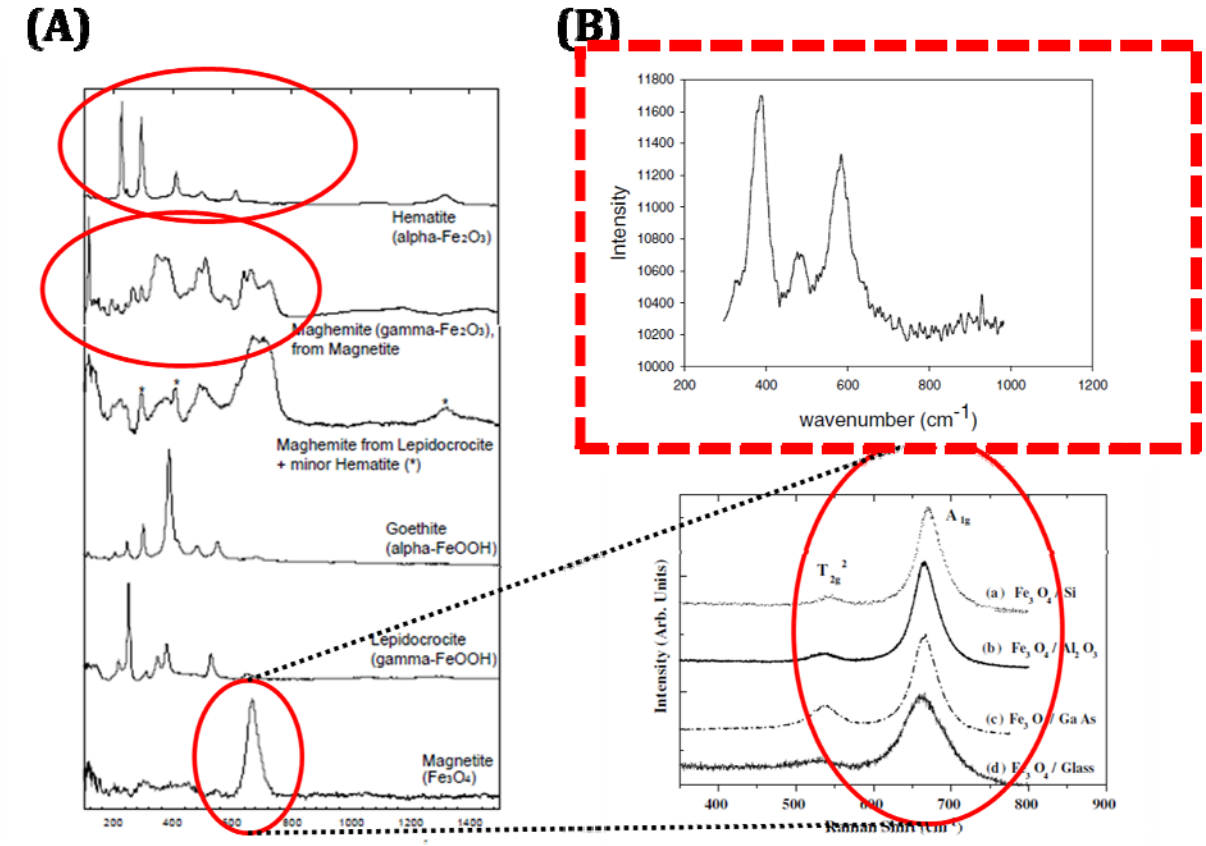

Figure 3.2. (A) Raman spectra of different composition of iron oxide, including α-Fe_2O_3-hematite, γ-Fe_2O_3-maghemite, and Fe_3O_4-magnetite, (B) Raman spectra of γ-Fe_2O_3-maghemite[21-23]. Please note the difference of relative peak intensity of maghemite from magnetite (A) and maghemite (B). reproduced from [De Faria. D et al, "Raman Microspectroscopy of some iron oxides and oxyhydroxides", Journal of Raman spectroscopy 28.11 (1997): 873-878] with permission of Wiley Online Library, and reproduced from [Hyeon. T et al, "Synthetic of Highly crystalline and monodisperse maghemite nanocrystallites without a size-selection process." Journal of the American Chemical Society 123.51 (2001): 12798-12801] with permission of American Chemical Society

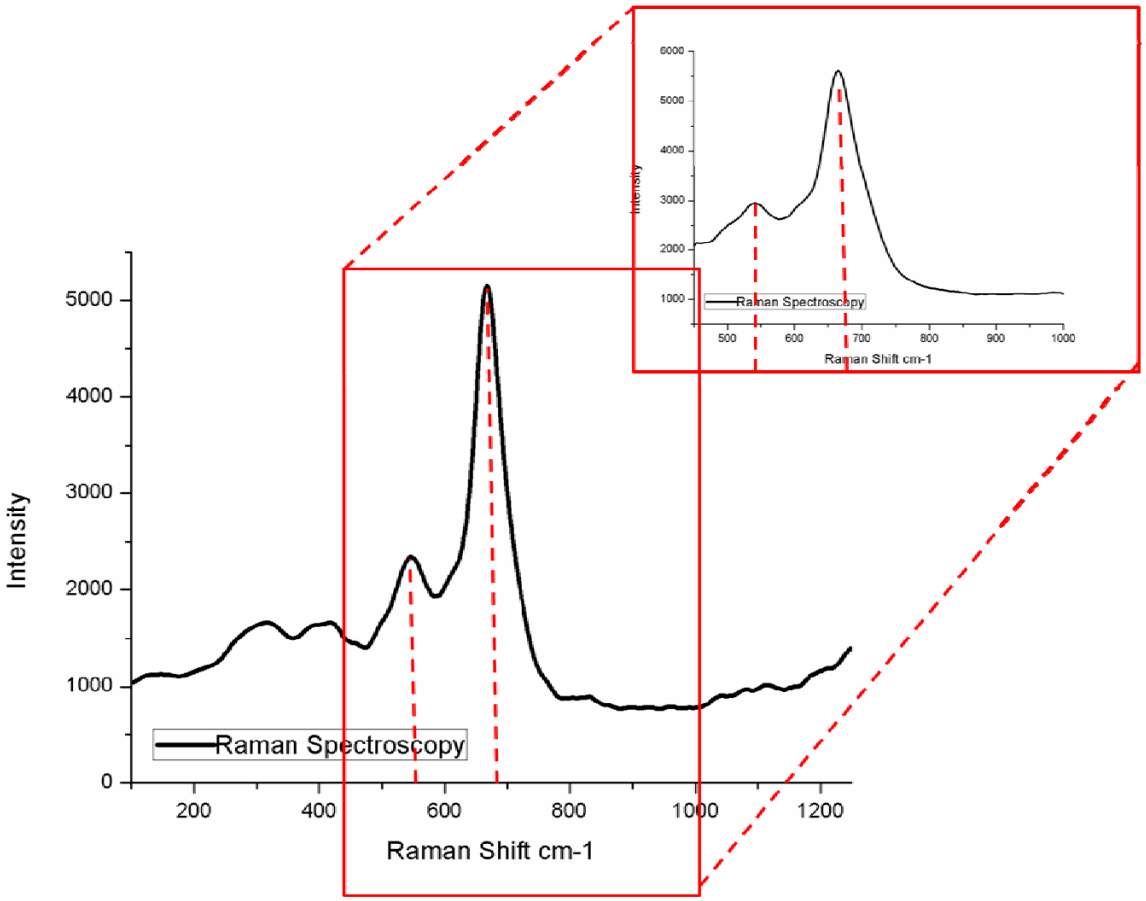

\

Figure 3.3. Raman spectra of fabricated Fe_3O_4-magnetite thin film capped with Ti. The Raman analysis was done in Molecular Analysis facility (MAF) using Renishaw InVIa Raman Microscope. The wavelength of the excitation laser source was 785 nm, which is highly collimated, and monochromatic.

3.3. Fe_3O_4-magnetite/Ti SAF thin film

3.3.1. Fe_3O_4-magnetite/Ti SAF thin film deposition

A reproducible fabrication of Fe_3O_4-magnetite based SAF thin films was carried out by magnetron sputtering system ($P_{base} < 5*10^{-6}$ torr). Our magnetron sputtering system, described in Chapter 2, is capable of having up to three different targets in deposition chamber, which enables the alternating of deposited materials. We selected Fe_3O_4-magnetite for magnetic, and Titanium as spacer materials due to their biocompatibility and cost

efficiency. Four different samples were fabricated: Ti/(Fe_3O_4/Ti)$_{X-1}$/Fe_3O_4/Ti, with *X=1, 2, 4* and *6,* on silicon substrate. We followed the recipe outlined in an earlier work by Kwon *et al*, in order to fabricate SAF thin films with suitable magnetostatic compensation[38].

3.3.2. Fe_3O_4-magnetite/Ti SAF thin film magnetic reversal behavior

Here, we discuss magnetic reversal behavior of our SAF thin films. As mentioned in 3.3.1, we fabricated four different samples: Ti/(Fe_3O_4/Ti)$_{X-1}$/Fe_3O_4/Ti with *X=1, 2, 4* and *6* on silicon substrate. The hysteresis loops measured in the in-plane direction of the as-fabricated SAF thin film are shown in Figure 3.4. As the number of ferrimagnetic layers increases from *X = 1* to *X = 6*, a significant decrease was observed in the in-plane coercivity, H_c, from ~350 Oe to ~<25 Oe. It is worth noting that we observe more than 90% reduction in the value of coercivity upon increasing the number of ferrimagnetic layers. Especially, for each SAF thin film with *X = 4* and *X = 6*, near superparamagnet-like behavior (H_c=~*0*) was observed due to antiferrimagnetic coupling between each ferrimagnetic layers with only one step switching. This superparamanget-like behavior is also consistent with other reports that were previously published [11,34,38,55]. One step switching only happens when the magnetization of each magnetic layer changes simultaneously to achieve the most energetically favorable state. The antiferromagnetic coupling causes the magnetization of each ferrimagnetic layer to compensate perpendicularly to the initial external magnetic field to achieve the most energetically favorable state. Ideally, the magnetization of each magnetic layer has to be perfectly antiparallel, but due to imperfect coupling, ferrimagnetic layers compensate with a small misalignment, which results in a finite magnetic remanence. As the number of ferrimagnetic layers increases, the strength of antiferromagnetic coupling increases, which

causes the decrease in magnetic remanence and coercivity value. However, as we increase the number of ferrimagnetic layers, the antiferrimagnetic coupling between each ferrimagnetic layers never becomes perfect like idealistic cases. Therefore, we see decrease in magnetic remanence and coercivity toward zero in asymptotic manner, and the resultant magnetic remanence and coercivity will never reach actual zero.

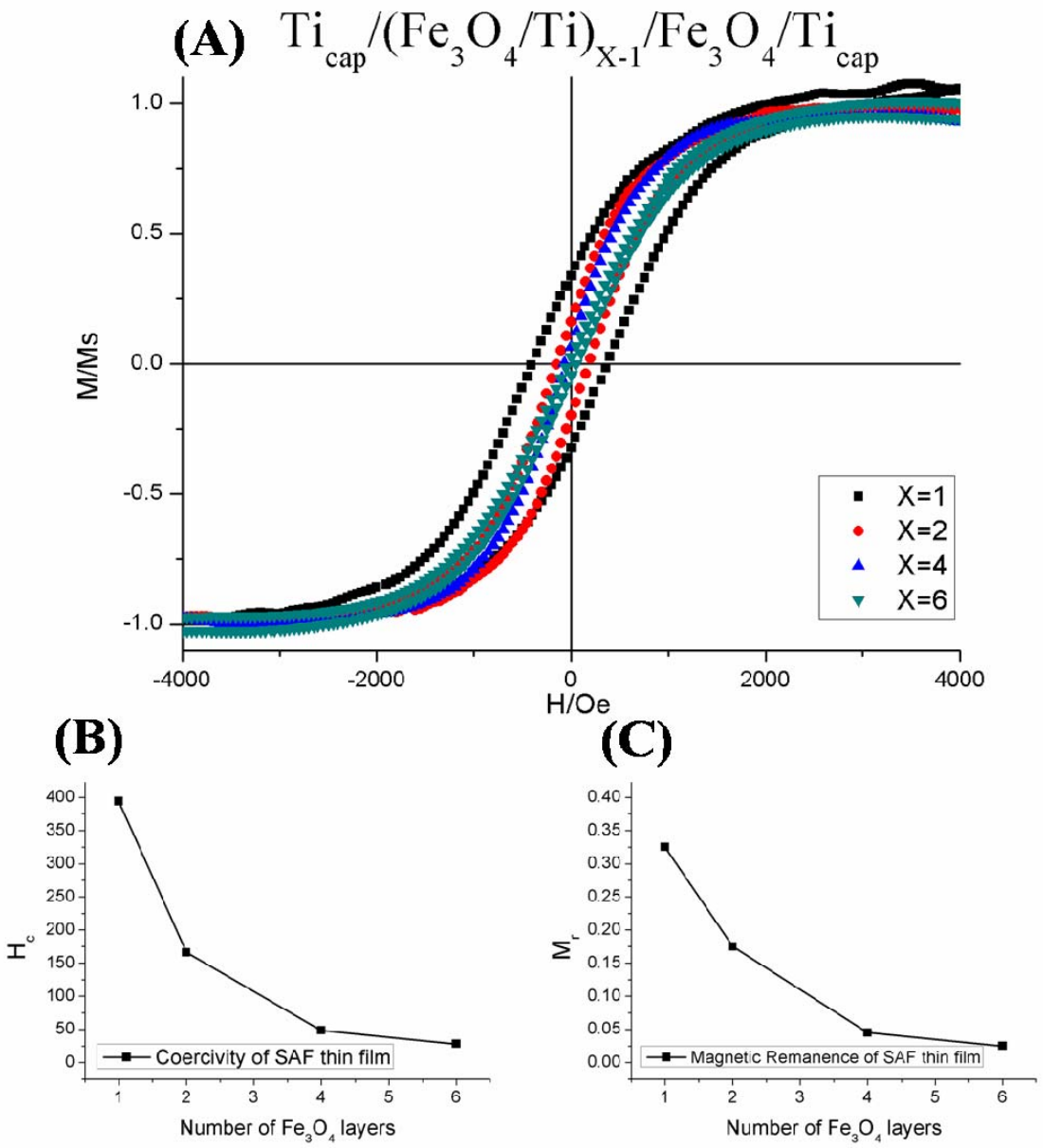

Figure 3.4. (A) represents the magnetic reversal behavior of SAF thin film with varying number of ferrimagnetic layers when *X= 1, 2, 4* and *6.* (B) and (C) present change of coercivity field and magnetic remanence of SAF thin film with varying number of ferrimagnetic layers, respectively.

3.3.3. Micromagnetic simulation and modeling of SAF thin film

The magnetization state of SAF thin film can be simulated by micromagnetic simulation (LLG) that was discussed in Chapter 2 in detail. As mentioned in Chapter 2, four different energies are involved in SAF system: exchange energy, magnetocrystalline energy, magneto-static energy and zeeman energy. In 3.3.2, we observed the decrease in magnetic remanence and coercivity value as we increased the number of ferrimagnetic layers. This is attributed to stronger anttiferromagnetic coupling as the number of ferrimagnetic layers was increased. Here, we discuss the computational method to estimate the effect of the number of ferrimagnetic layers on the magnetic remamence and coercivity value.

In order to do so, following dimensions were used to simulate the behavior of the thin film: cell dimension of the film = 500 nm by 500 nm with periodic boundary conditions to simulate a continuous thin film; thickness of the ferrimagnetic layer = 20 nm; thickness of the spacer layer = 15 nm; number of ferrimagnetic layers = 2,4, and 6; and number of spacer layers = 1, 3, and 5. The following dimensions were used in order to simulate the particular behavior of Fe_3O_4-magnetite: M_s = 480000 A/m, exchange stiffness constant, A = $1.32*10^{-6}$ J/m, magneto-crystalline anisotropy, K_{mc} = 0 to simulate the polycrystalline magnetite having 2 by 2 by 5 nm^3 cell. An in-plane external field of 0.5T was applied and then removed to achieve the remanent state (Figure 3.5). For SAF thin films, the LLG simulation predicts perpendicular antiparallel magnetization with certain misalignment due to the presence of the spacer, which is consistent with the magnetic reversal behavior at remanence (Figure 3.5). Furthermore, as the number of ferrimagnetic layer increases, we observe magnetostatic compensation of different layers in different directions, which results in a smaller magnetic remanence value. This is also consistent with a further decrease of magnetic remanence. In

conclusion, the remanent magnetiation state of SAF thin films involves in-plane magnetostatic compensation with imperfect antiferromagnetic coupling. From the domain images of each layer in Figure 3.5, we observe in-plane magnetostatic compensation with certain canting angle from the antiferromagnetic axis (perpendicular to external field). In order to further understand the magnetic behavior of SAF thin films, we proceed to explain this misalignment with fundamental antiferromagnetism.

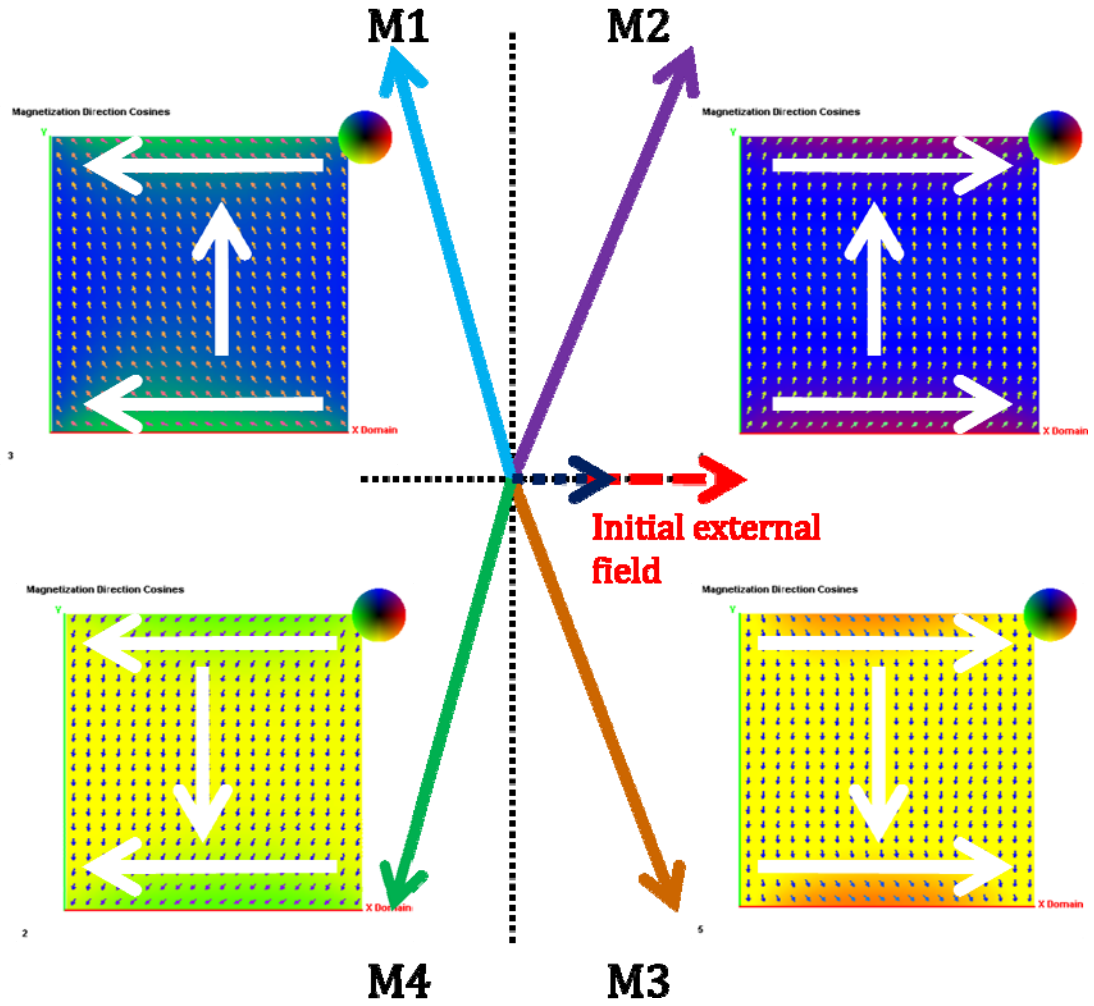

Figure 3.5. Domain images of simulated SAF thin films with two ferrimagnetic layers (A) and four ferrimagnetic layers (B) at magnetic remanence. (A) and (B) inset represent color wheel which indicate the direction of magnetization (**Red**: right, **Blue**: up, **Green**: left, **Yellow**: down). (A) and (B) both clearly demonstrate the magnetostatically compensating magnetization at remanence due to imperfect antiferrimagnetic coupling between each ferrimagnetic layers.

Here, the magnetization of the entire SAF thin film at remanence can be modeled as a single antiferrimagnet, which has compensating magnetization in a direction perpendicular to the initial field but with a fixed angle α, representing the imperfect antiferrimagnetic coupling between the magnetic layers (Figure 3.6). However, as the number of ferrimagnetic layers increases, the effect of antiferrimagnetic coupling becomes stronger. When the number of ferrimagnetic layers is two, those two layers magnetostatically compensate with respect to angle α. The antiferrimagnetic coupling, when the number of ferrimagnetic layers is even, can be quantitatively expressed as follows. When two layers magnetostatically compensate for each other, the resultant net magnetic moment is $M_{net,2} = 2M_A \sin \alpha$ from equation $H_{app} = 2\frac{1}{\chi}\omega M_A \sin \alpha$. When four layers magneto-statically compensate each other, the resultant net magnetic moment is $M_{net,4} = 2M_{net,2} * \sin \alpha = 4M_A \sin^2 a$ since two different sets of antiferrimagnetic coupling, each with angle α, exist (Figure 3.7 (B)). When six layers magneto-statically compensate for each other, the resultant net magnetic moment would be $6M_A \sin^2 \alpha * \sin \alpha$ since three antiferrimagnetic coupling exists. H_1, H_2, H_4, and H_6 are resultant magnetic moments at remanence state, which is also directly correlated to the field required to reverse the magnetization (coercivity value). By plotting the experimentally measured coercivity values against estimated values, we find that the values best fit the trend where $\alpha = \sim 24^{\circ}$, giving us an estimate of the α in our experiments.

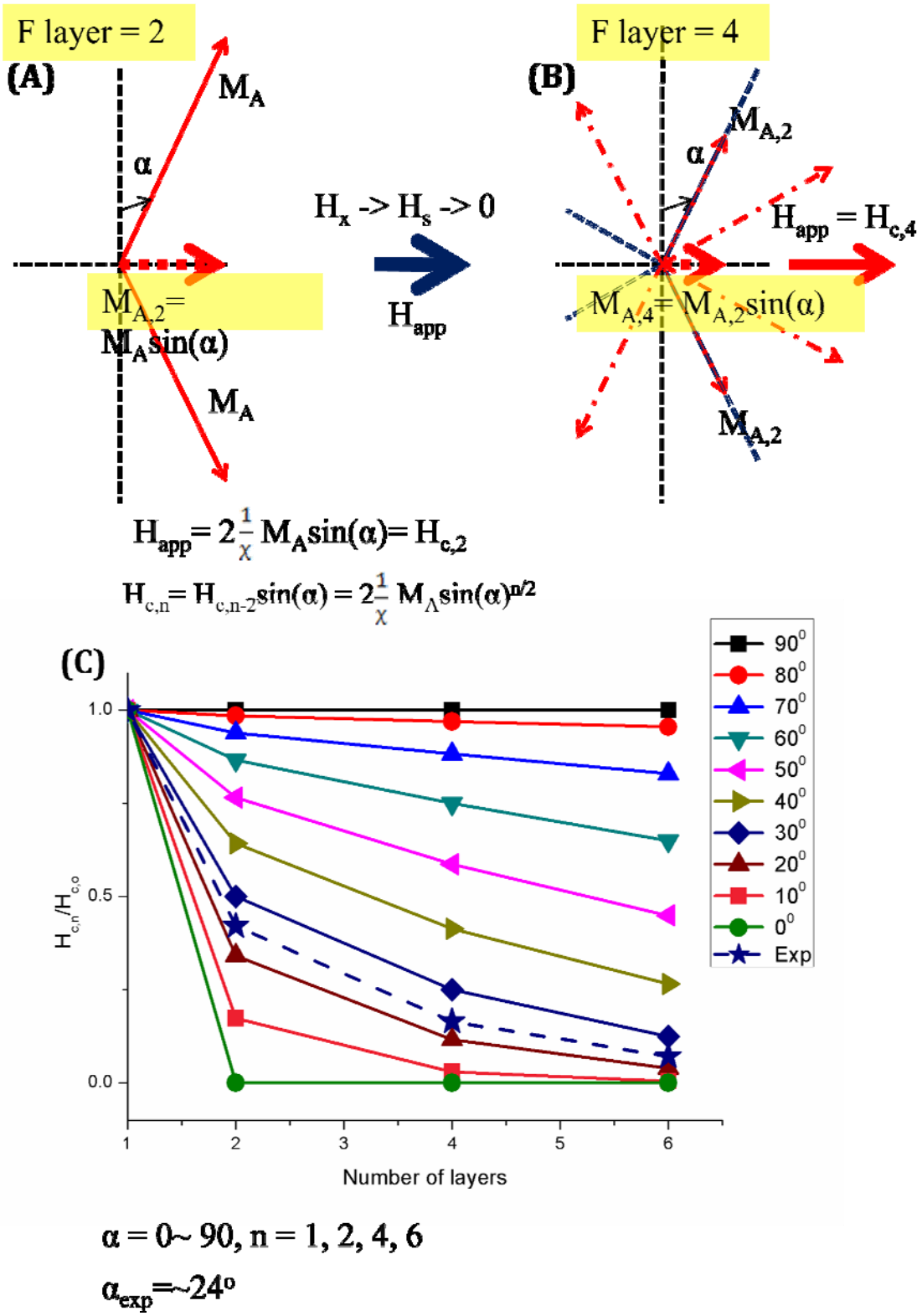

Figure 3.6. Model of magnetization of SAF thin film as the number of ferrimagnetic layers increases. (A) represents the magnetization when two ferrimagnetic layers are present, (B) represents the magnetization when four ferrimagnetic layers are present. (C) represents the resulting theoretical coercivity field value of SAF thin film using the theoretical model with respect to changing value of α.

We have demonstrated that the SAF films show a decrease in coercivity and magnetic remanence value due to antiferrimagnetic coupling, which is desired for our application. However, unlike the idealistic model of SAF configuration, we observed a finite residue value of magnetic remanence and coercivity due to imperfect magnetostatic compensation. As we increase the number of ferrimagnetic layers, we observed the decrease of magnetic remanence and coercivity as we strengthen the antiferrimagnetic coupling between magnetic layers. We attempted to numerically study and confirm such phenomenon using micromagnetic simulation and numerical modeling. With such studies, we were able to conclude that we would not have SAF configuration with perfect zero magnetic remanence and coercivity value. Therefore, we have to proceed with SAF configuration that has sufficiently low value of magnetic remanence and coercivity, but practical enough for our fabrication process.

Chapter 4

Fabrication of sombrero-shaped Fe_3O_4-magnetite nanoelements and their physical/magnetic properties

Contents of this chapter is partially published in reference [37], and [38]

4.1. Introduction

In Chapter 4, we discuss the fabrication of single phase Fe_3O_4-magnetite nanoelements, using nanoimprint lithography with control of the size and shape. In addition, we study physical and magnetic properties of nanoelements fabricated in an array form on silicon substrate. In Chapter 2.1., the deposition process using magnetron sputtering was discussed in detail. In Chapter 2.2., the fabrication method using nanoimprint lithography, selective etching, and lift-off process was described in detail. Furthermore, in Chapter 2.3, various characterization methods to study the physical and magnetic properties of fabricated elements were discussed in detail.

Here, we discuss how we combined the non-directional sputtering method using magnetron sputtering and nanoimprint lithography in order to produce complex, sombrero shape with 3D magnetization structure. Specifically, we utilized standard bi-layer resist undercut profile and non-directional sputtering in order to control the growth of side wall. Furthermore, controlled growth of center peak was observed as we increased the deposition length. After certain length of deposition, we confirmed a successful fabrication of arrays of

sombrero-shaped Fe_3O_4-magnetite nanoelements. Sombrero-shape is characterized by the existence of a side wall and a center cone-shaped peak, and exhibit unique 3D magnetic structure (co-existence of in-plane and out-of-plane magnetization within a single element). More specifically, we observed strong out-of-plane magnetization at side wall and center peak due to their high aspect ratio. However, we observed strong in-plane magnetization for the disk part of the elements due to its shape anisotropy. This co-existing different magnetic preference within a single nanoelement encourage us to study these fabricated nanoelements in detail.

4.2. Fe_3O_4-magnetite nanoelements

4.2.1. Fabrication of Fe_3O_4-magnetite nanoelements

As described in Chapter 2.2., we use nanoimprint lithography in order to create the dot patterns. This particular recipe was taken from the method developed by Zhang *et al.*[55] We first fabricated ETFE replicas via hot-embossing a clean ETFE sheet (DuPont Tefzel) with a Si master mold (350 nm size holes in hexagonal lattice form, 250 nm groove depth, and 700 nm period, from Lightsmyth Technologies), using our previously developed recipes[38,55]. Next, we fabricated a bilayer resist undercut profile for metallization. The bilayer resist consists of an undercut layer, LOR 1A (MicroChem) and an imprint layer, NXR-1025 (Nanonex). After the thermal imprinting with the ETFE stamp, we performed oxygen-plasma reactive ion etching (RIE) to remove the imprint resist residue, then selectively removed part of LOR 1A layer under the patterned area via wet-etching to create the bilayer-resist undercut profile (Figure. 4.1 (A, B, C, D). Next, we used non-directional deposition via magnetron

sputtering to develop sombrero-shaped magnetite nanoelements (Figure. 4.1 (E, F)). At the initial stage, magnetron sputtering deposits materials at the bottom forming nearly uniform thickness, with only a small amount of materials deposited along the side-walls. As the deposition time increases, a peak at the center starts to develop, and the side-wall becomes more apparent, eventually forming the sombrero-shaped structures. We also note that these nanoelements, both dish- and sombrero-shaped, are ~500 nm rather than ~350 nm in size (feature size of the stamp). Such enlargement of the feature size is attributed to the undercut resist profile (Figure. 4.1 (E,F)).

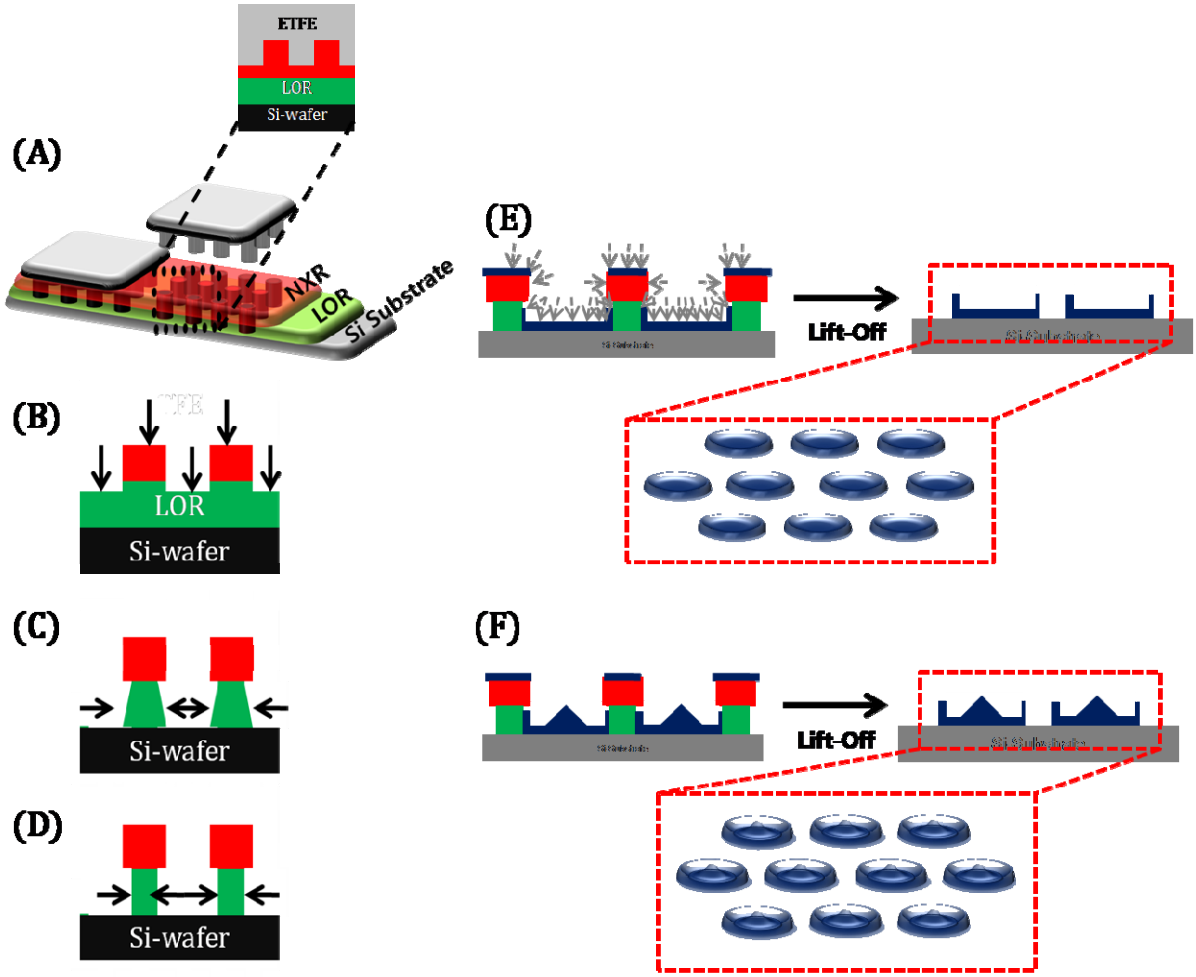

Figure 4.1. 3D and cross-sectional diagram showing the fabrication process of sombrero-shaped nanoelements using nanoimprint lithography (A), dry and chemical wet etching (B, C, D), and deposition and lift-off (E, F)

After patterning, we deposited Fe_3O_4 using magnetron sputtering under a deposition pressure less than 7.0 mTorr, and at room temperature. Figure 4.1 (E, F) demonstrate show sombrero-shaped nanoelements develop from a thin sheet. Initially, magnetron sputtering deposits materials only at the bottom and with a negligible amount on side-walls, but as the deposition time increases, side wall deposition starts to develop significantly. After a certain time of deposition (~2 hours), the side-wall is well-defined and is an essential part of the sombrero-shaped nanoelements. These sombrero-shaped nanoelements are larger (~500 nm) in size than the size of the stamp (~350 nm) because the non-directional sputtering deposits the material under the undercut resist profile and even at side-walls (Figure 4.1 E, F). After deposition, subsequent lift-off removed the bi-layer resist and the surplus metals on top to leave sombrero-shaped magnetite nanoelements on the silicon substrate (Figure 4.1 E, F).

Figure 4.2. shows the SEM images during the deposition process to show the development of sombrero-shaped nanoelements

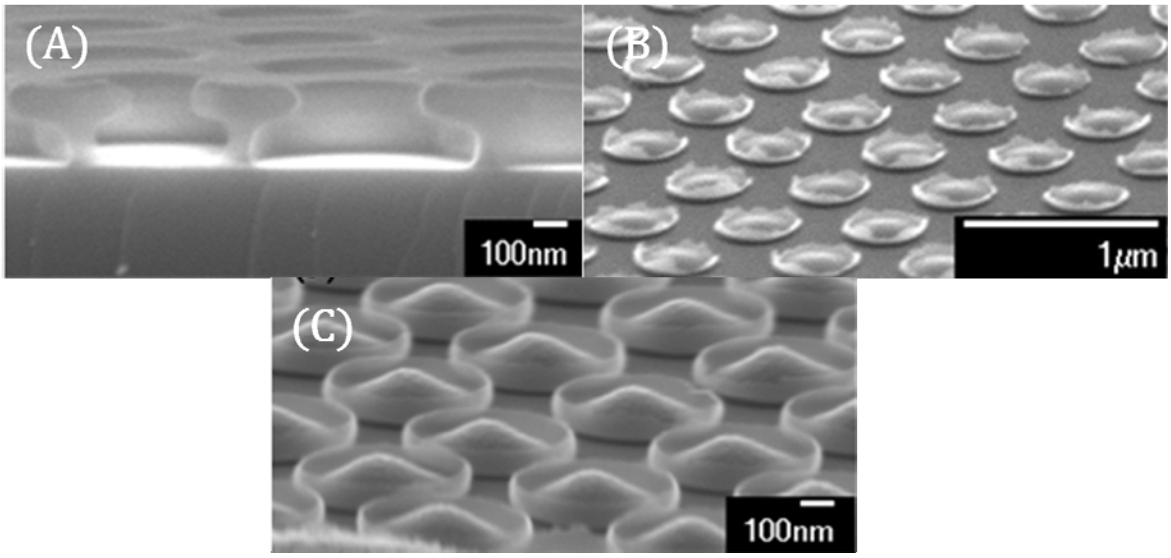

Figure 4.2. SEM images showing fabrication of sombrero-shaped Fe_3O_4-magnetite nanoelements: (A) bi-layer undercut resist profile, (B) dish-shaped nanoelements (intermediate state), and (C) sombrero-shaped nanoelements

4.2.2. Magnetic Force Microscopy/Atomic Force Microscopy on Fe_3O_4-magnetite nanoelements

Atomic Force Microscopy (AFM) and Magnetic Force Microscopy (MFM) are main tools to analyze the morphologies and out-of-plane magnetization state on a particular scan area. The detailed mechanism of AFM and MFM are discussed in Chapter 2.3. Here, MFM was used to analyze the out-of-plane magnetization state of both single dish- and sombrero-shaped nanoelements. An external field (~2500 Oe) perpendicular to the sample surface was applied for 20 seconds and then removed to achieve the magnetic remanent state. We first scanned for the topography using a CoCr coated low moment probe, followed by a MFM scan with a lift height of 50 nm to investigate the magnetization state of both nanoelements. From the topography scan (Figure 4.3 (A), (C)), we observe that both dish-shaped and sombrero-shaped nanolements are ~500 nm in diameter. Sombrero-shaped nanoelements have side-walls and a cone shaped structure at the center, which is consistent with SEM images. From the MFM scan (Figure 4.3 (B), (D)), we observe strong out-of-plane magnetic signal at the edge of both nanoelement, and at the center peak of the sombrero-shaped nanoelement. For dish-shaped nanoelements, no out-of-plane magnetization in the center was observed.

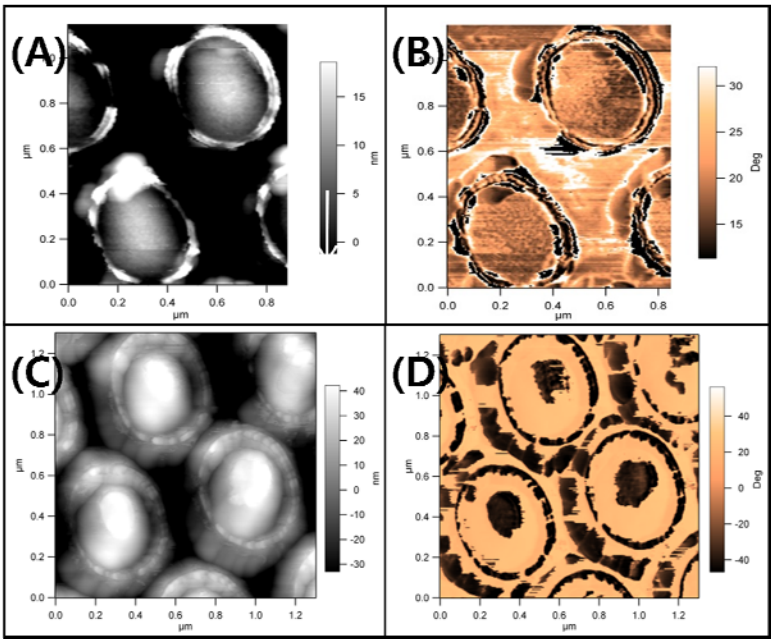

Figure 4.3. AFM topography images for (A) dish- and (C) sombrero-shaped nanoelements. Corresponding MFM images for each element showing out of plane magnetization components at the side-wall for both nanoelements (B, D) and in the central cone for only the sombrero-shaped nanoelements (D).

4.2.3. Micromagnetic simulation on Fe_3O_4-magnetite nanoelements

To further investigate the magnetization state of both elements, micromagnetic simulation (LLG) was carried out, as schematically shown in Figure 4.4 (A), (B). Following dimensions were used for simulations: diameter of the nanoelement = 500 nm; thickness of the disk-part = 50 nm; thickness of the side-wall = 3 nm; total height of side-wall = 150 nm; diameter of top and middle disk for sombrero-shaped nanoelement = 37.5 nm and 112.5 nm; height of top and middle disk for sombrero-shaped nanoelement = 50 nm. The following magnetic parameters were used for simulation: M_s = 480 emu/cm^3, exchange stiffness constant, A = 1.32 µerg/cm, magnetocrystalline anisotropy, K_{mc} = 0 to simulate the polycrystalline magnetite having 2×2×25 nm^3 cell. An out-of-plane external field of 1500 Oe was applied and then removed to achieve the remanent state shown in (Figure 4.4 (C), (D),

(E), (F)).The out-of-plane magnetization direction is shown by taking a side-view slice through the middle of each element. For the dish-shaped element, we observe a double vortex state for the bottom disk layer (Figure 4.4 (C)) with opposing chirality. In addition, a strong out-of-plane component was observed in the side-wall (side view (Figure 4.4 (G)) for a thickness of 3 nm (for larger thickness, ~ 5 nm, the magnetization in the side-wall was totally in plane). This is in agreement with the MFM images, where we observe an out-of-plane magnetization at the side-wall. Further, the MFM images revealed an in-plane magnetization at the center, but the simulated double vortex state was not observed in MFM due to insufficient resolution. For sombrero-shaped nanoelements, however, the simulation predicts a single vortex state in the bottom disk component (Figure 4.4 (D)) with its magnetic singularity being pinned by the out-of-plane magnetization component of the central cone of the sombrero. In addition, strong out-of-plane magnetization component at side-walls is predicted by the simulation (Figure 4.4 (H)) and observed in the MFM image. In conclusion, the remanent magnetization state of dish-shaped and sombrero-shaped nanoelements involves both in-plane and out-of-plane components that are consistent with their three-dimensional structures; and a good agreement was found between MFM images and micromagnetic simulation.

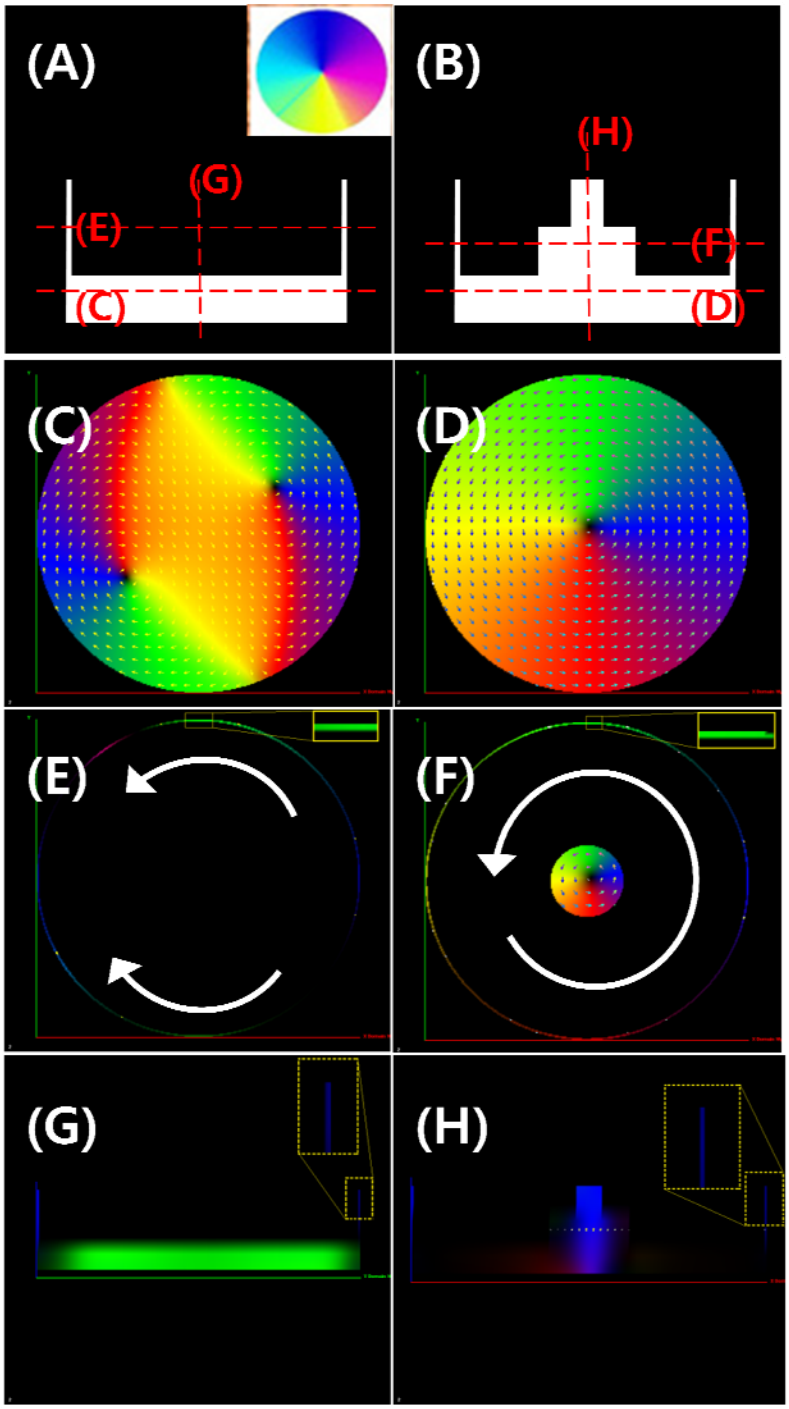

Figure 4.4. Schematic diagram of the model of the (A) dish-shaped and (B) sombrero-shaped nanoelements used for LLG micromagnetic modeling. The dish-shape was modeled as a disk with a narrow ring on top. For the sombrero-shape, two additional disks with decreasing diameter were used to simulate the central cone as well. Domain structures were then simulated at different heights. The magnetic structure of the bottom disk component of (C) dish- shape shows a double-vortex structure with opposite chirality but (D) sombrero-shaped nanoelements shows a single vortex. The side-walls in both cases (E, F) show an in-plane component with the chirality consistent with the underlying disk due to strong exchange coupling. Cross-sectional view of (G) dish-shaped nanoelements with a strong in-plane component and (H) sombrero-shaped nanoelements with an out-of-plane component in the central cone. In both cases, the side-wall has an out-of-plane magnetization component.

Chapter 5

Fabrication of Fe_3O_4/Ti SAF nanoparticles and their physical/magnetic properties

5.1. Introduction

In Chapter 5, we discuss fabrication of Fe_3O_4/Ti synthetic antiferromagnetic (SAF) nanoparticles using nanoimprint lithography with control of size, structure and shape. We combine the non-directional sputtering method and concept of SAF in order to fabricate sombrero-shaped nanoparticles, which has near zero magnetic remanence and coercivity at magnetic remanence. Furthermore, we discuss the method to release the fabricated nanoparticles into the solution using isotropic SF_6+O_2 ion etching. In Chapter 2.1., the deposition process using magnetron sputtering was discussed in detail. In Chapter 2.2., the fabrication method using nanoimprint lithography, selective etching, and lift-off process was described in detail. The fabricated nanoparticles were studied using various characterization methods discussed in Chapter 2.3.

In this Chapter, we proceeded from fabricating an array of sombrero-shaped Fe_3O_4 nanoparticles with 3D magnetic structures to fabricating an array of sombrero-shaped SAF nanoparticles by combining nanoimprint lithography, non-directional sputtering, and concept of SAF. The sombrero-shaped SAF nanoparticles have near zero magnetic remanence and coercivity at magnetic remanence. Sombrero-shape is mainly composed by the existence of side-wall and center cone-shaped peak. Furthermore, we released these nanoparticles in solution using isotropic SF_6+O_2 ion etching.

5.2. Fe_3O_4/Ti nanoparticles

5.2.1. Fabrication of Fe_3O_4/Ti nanoparticles

As described in Chapter 2.2., we use the nanoimprint lithography in order to create the dot patterns. The recipe was taken from the method developed by Zhang *et* al[55], but adjusted it for magnetite lift-off. To replicate ETFE mold from silicon master mold, we cleaned and ultra-sonicated a sheet of ETFE (DuPont Tefzel) with acetone and isopropyl alcohol for 5 minutes, blow-dried with nitrogen, and placed onto a clean Si-wafer. The Si master mold with 350 nm holes in a hexagonal lattice, from Lightsmyth Technologies, was placed on the ETFE sheet, then imprinted using a Nanonex NX-B 100 compact thermal nanoimprinter, at 250°C and 450 psi for 2 minutes. Next, we spin-coated a bilayer-resist, consist of LOR 1A (MicroChem) and NXR-1025 (Nanonex), and soft-baked each layer at 200°C and 150°C on a hot plate, respectively. After the bilayer-resist was ready, we patterned it with the replicated ETFE mold using Nanonex NX-B100 imprinter (Figure 5.1 (A)). Large area hole arrays (350 nm) of the top layer were obtained. Next, we performed anisotropic oxygen plasma reactive ion etching (RIE) to remove the imprint resist residue, then we selectively etched LOR 1A layer of the patterned bilayer resist to create an undercut. Then we deposited Fe_3O_4/Ti multilayers using magnetron sputtering under a deposition pressure less than 7.0 mTorr, and at room temperature. Figure 5.1 (C, D) demonstrate how Fe_3O_4/Ti multilayers are fabricated from a thin sheet to sombrero-shaped particles. Deposition time for both Fe_3O_4 and Ti was carefully calibrated for desired thickness for each layer (Fe_3O_4 = ~15 nm and Ti = ~2 nm). These sombrero shaped nanoparticles are larger (~500 nm) in size than the size of the stamp (~350 nm) because the non-directional sputtering deposits under the

undercut resist profile and even at side-walls (Figure 5.1 (C & D)). After the deposition, subsequent lift-off removed the bilayer resist and the surplus metals on top to leave sombrero-shaped magnetite nanoparticles on the silicon substrate (Figure 5.1 (E)). Finally, using a $SF_6 + O_2$ mixed gas plasma RIE, the silicon substrate was selectively etched into sharp peaks using the SAF nanoparticles themselves as the etching mask, eventually leaving the SAF magnetite nanoparticles loosely attached to each silicon peak via Van der Waals forces (Figure 5.1 (F)). Then these magnetite nanoparticles were released by putting the silicon substrate into DI water, followed by a brief ultra-sonication to shake off the nanoparticles (Figure 5.1 (G)). Finally, these magnetite nanoparticles were characterized with SEM and PPMS to analyze their morphology and magnetic properties.

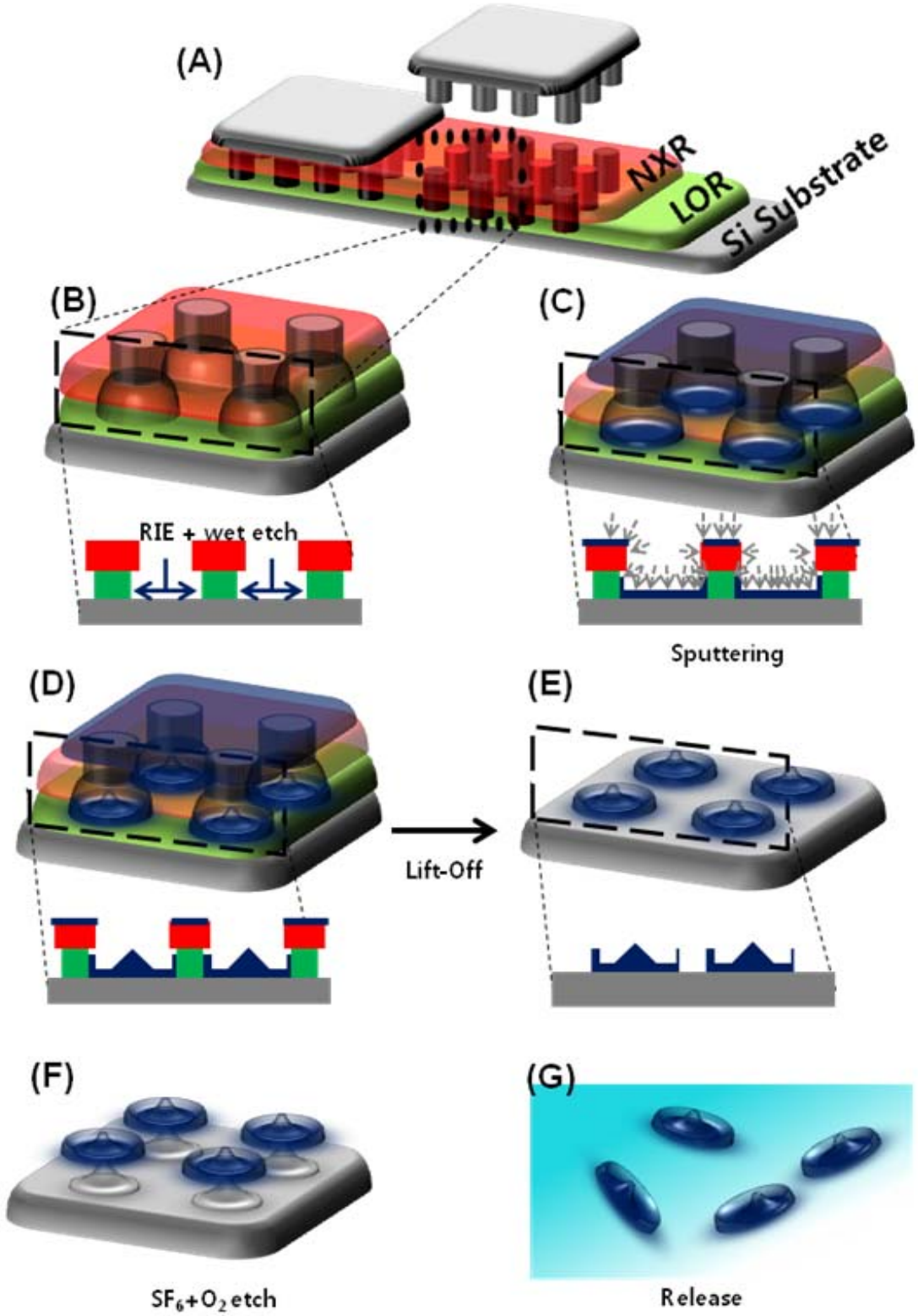

Figure 5.1. Schematic diagram of nanoimprint process used to fabricate sombrero-shaped magnetic nanoparticles.

Each of the steps presented above is demonstrated visually by SEM images. Figure 5.2 (A) demonstrates the bilayer resist undercut profile after the nanoimprinting and wet etching development. To fabricate the sombrero-shape without defects on the wall, we controlled the time of wet etching in order to develop an undercut profile without any bottom tail; bottom tail refers to undercut resist residue due to under-etch and has to be avoided as it can cause breakage of the side wall at the time of wet etching and ultra-sonication. Detail of the relationship between the bottom tail and etching is discussed in an earlier work. Figure 5.2 (B, C) presents cross-sectional and overhead views, respectively, of arrays of magnetite nanoparticles on a silicon substrate after the lift-off step. The diameter of the sombrero-shaped SAF nanoparticle is ~500 nm. Our innovation here is to fabricate sombrero-shaped SAF nanoparticle by using non-directional deposition with bi-layer undercut profile. Figure 5.2 (D) presents intermediate step of $SF_6 + O_2$ etch, which shows that the nanoparticles are still attached to Si pillars. Figure 5.2 (E & F) exhibits the ideal etch result where the sombrero-shaped nanoparticles are loosely attached to cone-shaped Si pillars via Van der Waals force. Figure 5.2 (E) shows that the sombrero-shaped nanoparticles are attached as arrays; however, after slight external force such as slight sudden tilt, they are tilted and only loosely attached to the Si substrate[38,55]. We tested the etching parameters for releasing the nanoparticles and found that the optimized etching power is 50W (Trion RIE) with 3 min etching, which is sufficient to fully detach the nanoparticles from the Si wafer. The sombrero-shaped SAF nanoparticles are then released from the original substrate (Figure 5.2 (G)), and transferred to solution (Figure 5.2 (H)). The thickness of the center of SAF nanoparticles and diameter of SAF nanoparticles were ~70 nm, and ~500 nm respectively, and the height of the side-wall was ~50 nm, which remained intact and unchanged throughout the process of release. As demonstrated in Figure 5.2 (E, F, H), the sombrero-shaped SAF nanoparticles

were transferred without change in shape, structure, and size. Even the thin side-wall was not damaged throughout the process.

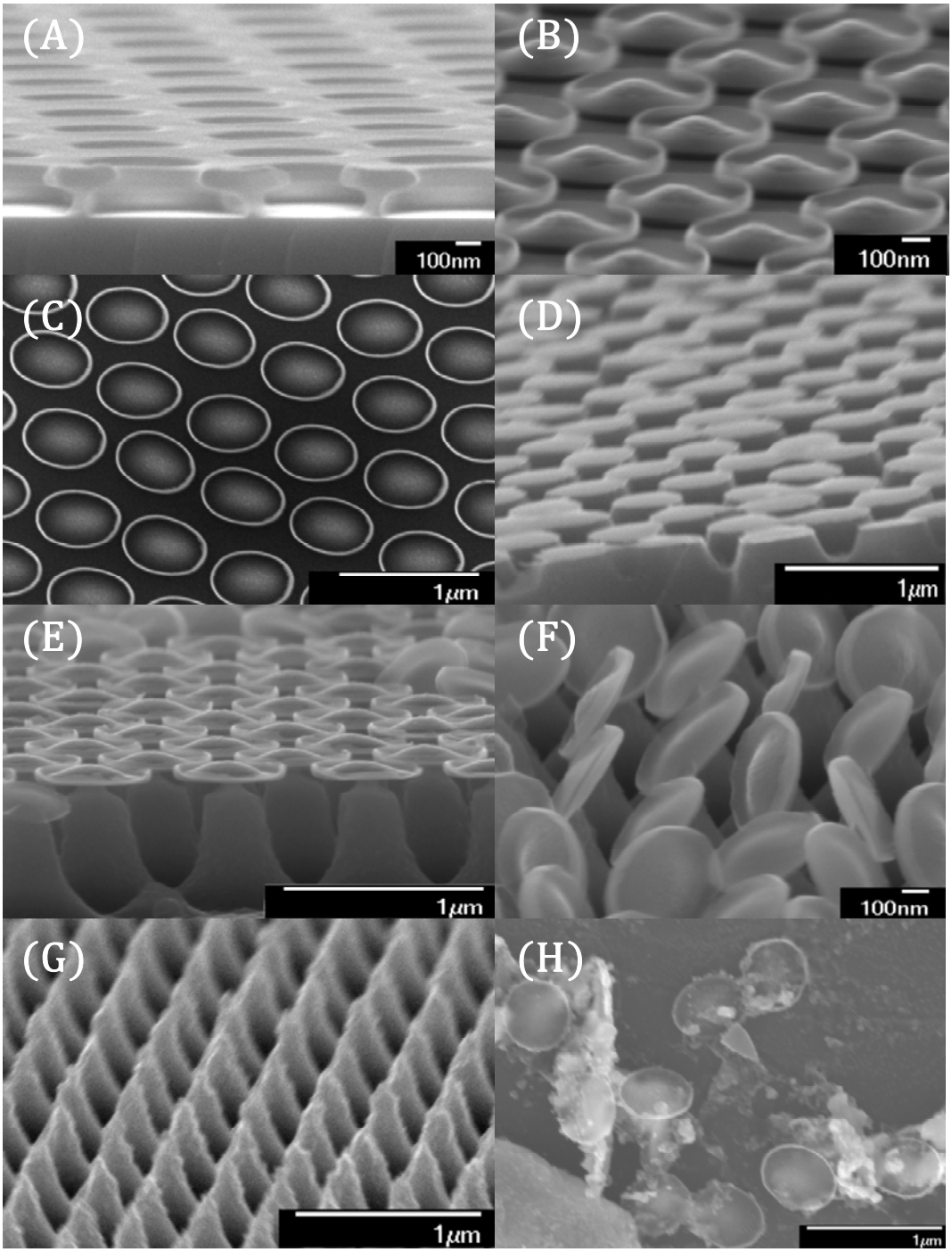

Figure 5.2. SEM images showing the steps in the fabrication and release of sombrero-shaped SAF nanoparticles.

5.2.2. Magnetic reversal behavior of sombrero-shaped SAF nanonparticles

In order to demonstrate the magnetic properties of our SAF, we prepared Fe_3O_4/Ti multilayer elements. There have been many previous papers on synthetic antiferromagnetic (SAF) nanoparticles discussing the variation of magnetic properties with the thickness of each layers[11,27,28,34,38,55,64]. We used two sequences of multilayers Ti/$(Fe_3O_4/Ti)_{X-1}$/Fe_3O_4/Ti, with *X=1, 2, 4 and 6*, deposited by magnetron sputtering. The hysteresis loop measured in the in-plane and out-of-plane directions of the as-fabricated SAFs are shown in Figure 5.3 (A & B). As the number of ferrimagnetic layers increases from X = 1 to X = 6, significant decrease of coercivity, H_c, in the in-plane direction, from ~ 355 Oe to ~ < 25 Oe, was observed. Especially, for SAF nanoparticles with X = 4, and X = 6, near superparamagnet-like behavior (H_c ~ 0) was observed, which will lead to minimal agglomeration when released into solution, and enhanced their potential use in biomedical application. This superparamagnet-like behavior of SAF nanoparticles with bi-ferromagnetic layer in the in-plane direction is consistent with other reports that were previously published[11,34,38,55]. However, no change in the coercivity was observed in the out-of-plane direction, which remained at ~ 200 Oe. It is speculated that as the side wall becomes extremely thin at the end, the magnetic and non-magnetic layers start to merge into each other. Therefore, side wall would act as a single magnetic layer, which causes the coercivity and magnetic remanence.

Despite the complex shape, the sombrero-shaped SAF nanoparticles have higher aspect ratio in the in-plane direction than the out-of-plane direction. Due to their shape anisotropy, these SAF nanoparticles primarily prefer in-plane magnetization. Therefore, we observe significant decrease in coercivity value in the in-plane direction since stronger

antiparallel magneto-static compensation forces the in-plane magnetization to remain very small as the number of ferromagnetic layer increases. This is reflected in the in-plane hysteresis loops shown in Figure 5.3 (A). On the other hand, the sombrero-shaped SAF nanoparticles also favors certain magnetization components to be along the out-of-plane magnetization direction, especially at the side-walls and at the center peak. However, this out-of-plane magnetization component is significantly smaller compared to the in-plane magnetization component due to the aspect ratio of sombrero-shape of the particle. This is consistent with the higher and unchanging coercivity value shown in Figure 5.3 (B).

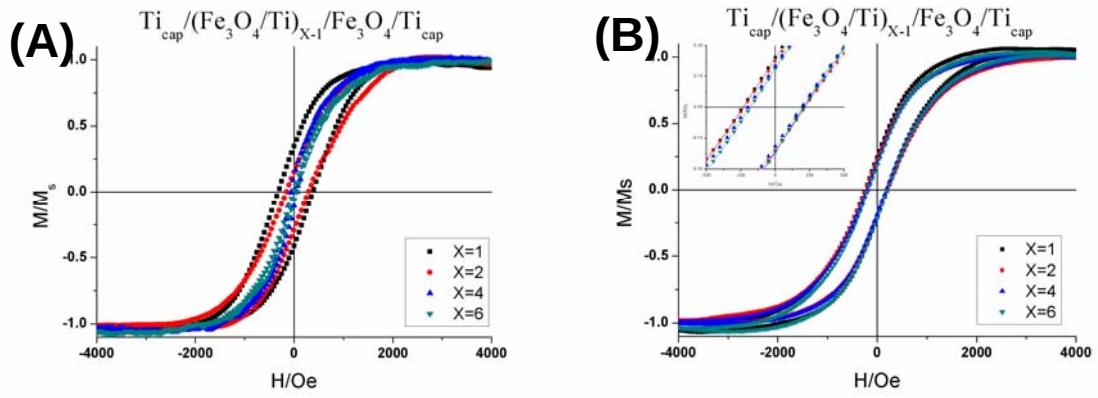

Figure 5.3. Hysteresis loops of the SAF multi-layered nanoparticles measured in the in-plane direction, in which H_c~0 is observed at X=4, and X=6, (A) and out-of-plane direction (B) on substrate with different number of alternating layers (X=1, X=2, X=4, X=6).

5.2.3. Micromagnetic modeling of sombrero-shaped SAF nanoparticles using LLG simulation

The magnetization state of sombrero-shaped particles were further investigated by micromagnetic simulation (LLG) as shown in Figure 5.4. The following dimensions were used for simulations: diameter of the nanoelement = 500 nm; thickness of the ferrimagnetic layer = 20 nm; thickness of the spacer layer = 5 nm; number of ferrimagnetic layers = 4;

number of spacer layers = 3; thickness of the side wall = 3 nm; total height of side wall = 150 nm; base diameter of center peak for sombrero-shaped nanoelement = 97.5 nm. The following magnetic parameters were used for simulation: M_s = 480 emu/cm^3, exchange stiffness constant, A = 1.32 μerg/cm, magneto-crystalline anisotropy, K_{mc} = 0 to simulate the polycrystalline magnetite having 2×2×5 nm^3 cell. An out-of-plane external field of 5000 Oe was applied and then removed to achieve the remanent state shown in Figure 5.4 (A, B, C & D). The out-of-plane magnetization direction is shown by taking a side-view slice through the middle of each element. For sombrero-shaped nanoparticles, the LLG simulation predicts a single vortex state in the bottom disk component (Figure 5.4 (C)) with its magnetic singularity being pinned by the out-of-plane magnetization component of the central cone of the sombrero (Figure 5.4 (A)). In addition, antiparallel magneto-static compensation was observed between each ferrimagnetic layer outside of the center cone, which explains the near zero coercivity in the in-plane hysteresis loop. In addition, strong out-of-plane magnetization component at side-walls is predicted by the simulation (Figure 5.4 (A)). In conclusion, the remanent magnetization state of sombrero-shaped nanoelements involves both in-plane and out-of-plane components that are consistent with their three-dimensional structures; and a good agreement was found between magnetic reversal analysis and micromagnetic simulation.

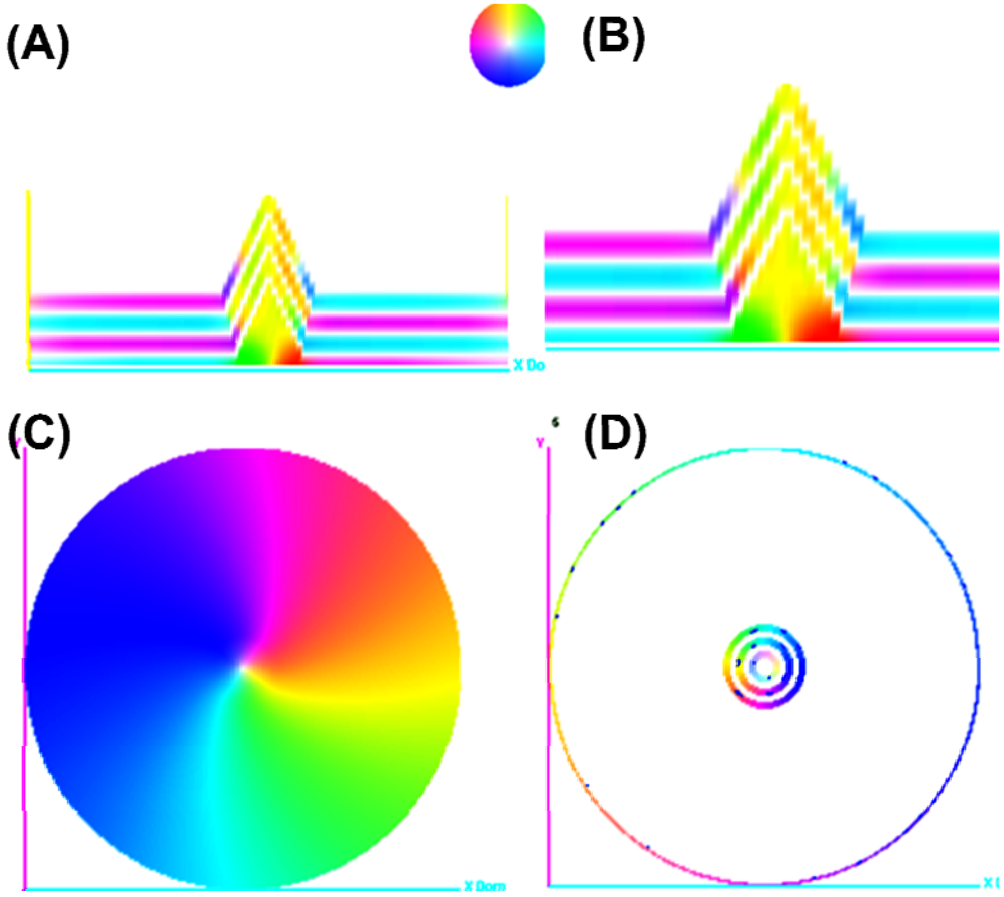

Figure 5.4. Synthetic Antiferromagnetic sombrero-shaped nanoparticles used for LLG micromagnetic modeling. For the SAF nanoparticles, alternating layers of ferrimagnetic layers and spacer were used to simulate the mechanism of SAF. Multiple disks with decreasing diameter were used to simulate the central cone. A thin ring at the edge was used to simulate the side wall. Cross-sectional view of sombrero-shaped nanoparticles with an out-of-plane component in the central cone and side wall, anti-parallel magneto-static compensation is shown between layers (A, B). Domain structures were then simulated at different heights. SAF sombrero-shaped nanoparticles shows a single vortex at the bottom layer (C). However, opposite chirality shows as layer increases due to the antiparallel magneto-static interaction to compensate.

5.2.4. Magnetic force microscopy on sombrero-shaped SAF nanoparticles

The magnetization state of a single SAF nanoparticle was studied through Magnetic Force Microscopy (MFM). We applied external field higher than the saturation field (~2500 Oe) parallel to the sample surface and removed to achieve the magnetic remanent state. Then we investigated magnetic configurations of the particle using 15 nm CoCr coated low

moment probes with a lift height of 50 nm[65,66]. As shown in Figure 5.5, we observed a strong out-of-plane component at edge/center. This is consistent with the hysteresis loop (Figure 5.3) and micromagnetic simulation (Figure 5.4). The zero remanent magnetization could possibly be attributed to the anti-parallel magneto-static compensation between each ferrimagnetic layers within the sombrero-shaped nanoparticle. It is also worth mentioning that this distinct magnetic signal observed through MFM was sensitive to the layer structure of a SAF nanoparticle, and was not caused by any topological residue. To be specific, when the number of Fe_3O_4 and Ti spacer layers double, the magnetic signal becomes much stronger compared to bilayer-structure, where it shows barely any magnetic signal.

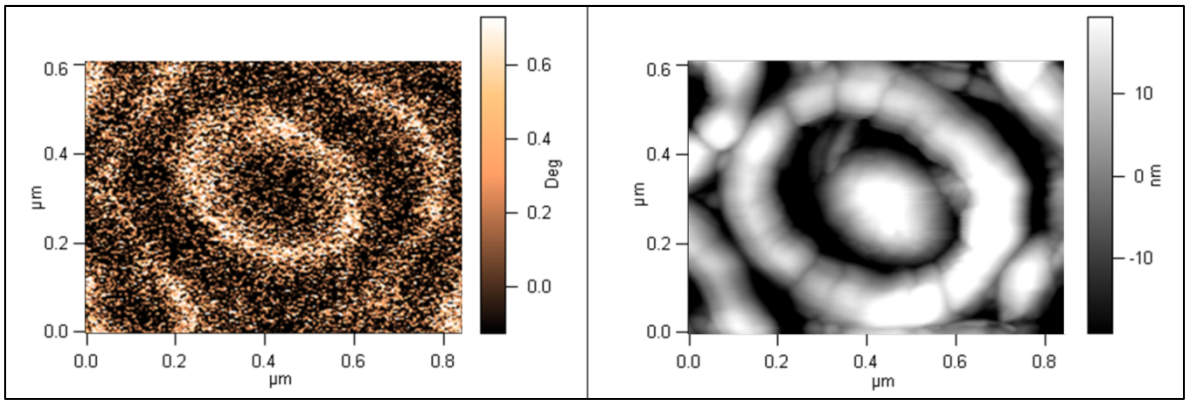

Figure 5.5. Magnetic Force Microscopy (MFM) image of SAF sombrero-shaped nanoparticles with four alternating Fe_3O_4 layers with a Ti spacer layer between each pair of Fe_3O_4 layers (A). Out-of-plane component is observed in the central cone and side wall. Scanning probe image (B) demonstrates the complex topology of SAF sombrero-shaped nanoparticles with side-wall and central cone.

Chapter 6

Fabrication, release and mechanical rotation of disk-shaped SAF nanoparticles

6.1. Introduction

In Chapter 6, we demonstrate fabrication, release, and rotation of synthetic antiferromagnetic (SAF) nanoparticles using nanoimprint lithography with the control of size, structure and shape. In order to have magnetic nanoparticles in aqueous solution for proposed biomedical application, we use SAF nanoparticles sputtered by the anisotropic sputtering method, which then is released from the silicon substrate using isotropic RIE etching. The detailed method was discussed in Chapters 2, 4 and 5. In this chapter, we characterize the mechanical rotation of SAF nanoparticles in aqueous solution by using a simple instrument, which uses laser, photodiode and rotating magnet. This instrument detects the difference of transmitted laser intensity caused by the mechanical rotation of magnetic nanoparticles in solution.

6.2. Disk-shaped SAF nanoparticles

In Chapters 4 and 5, we utilized non-directional sputtering method in order to fabricate sombrero-shaped magnetic nanoparticles with control. However, due to complex geometry and complex magnetic orientation of sombrero-shaped magnetic nanoparticles, we find that SAF nanoparticles with a sombrero-shape are not conducive to controlled

mechanical rotation. Instead, we recommend the use of disk-shaped SAF nanoparticles for biomedical application, as its magnetic orientation allows for a calibrated control of movements of nanoparticles in aqueous solution.

6.2.1. Fabrication of disk-shaped nanoparticles

As described in Chapter 2.2., we use nanoimprint lithography in order to create the dot patterns with diameter of 350 nm. The lithography method was described in detail in Chapter 2.2, 4.2 and 5.2. In previous chapters, non-directional magnetron sputtering was used in the deposition step in order to fabricate sombrero-shaped nanoparticles, but here, we used ion beam sputtering (IBS) in order to perform anisotropic deposition, instead of non-directional magnetron sputtering. IBS deposition method allows us to obtain disk-shaped nanoparticles rather than sombrero-shaped nanoparticles (Figure 6.1). These disk-shaped nanoparticles are similar (~350 nm) in size to the size of the stamp (~350 nm), which is an indication of highly anisotropic deposition. After deposition, subsequent lift-off removed the bilayer resist and the surplus metals on top to leave disk-shaped nanoaprticles on the silicon substrate (Figure 6.1). Finally, using a $SF_6 + O_2$ mixed gas plasma RIE, the silicon substrate was selectively etched into sharp peaks using the SAF nanoparticles themselves as the etching mask, eventually leaving the SAF nanoparticles loosely attached to each silicon peak via Van der Waals forces. Then these nanoparticles were released by putting the silicon substrate into DI water, followed by a brief ultra-sonication (< 5mins) to shake off the nanoparticles.

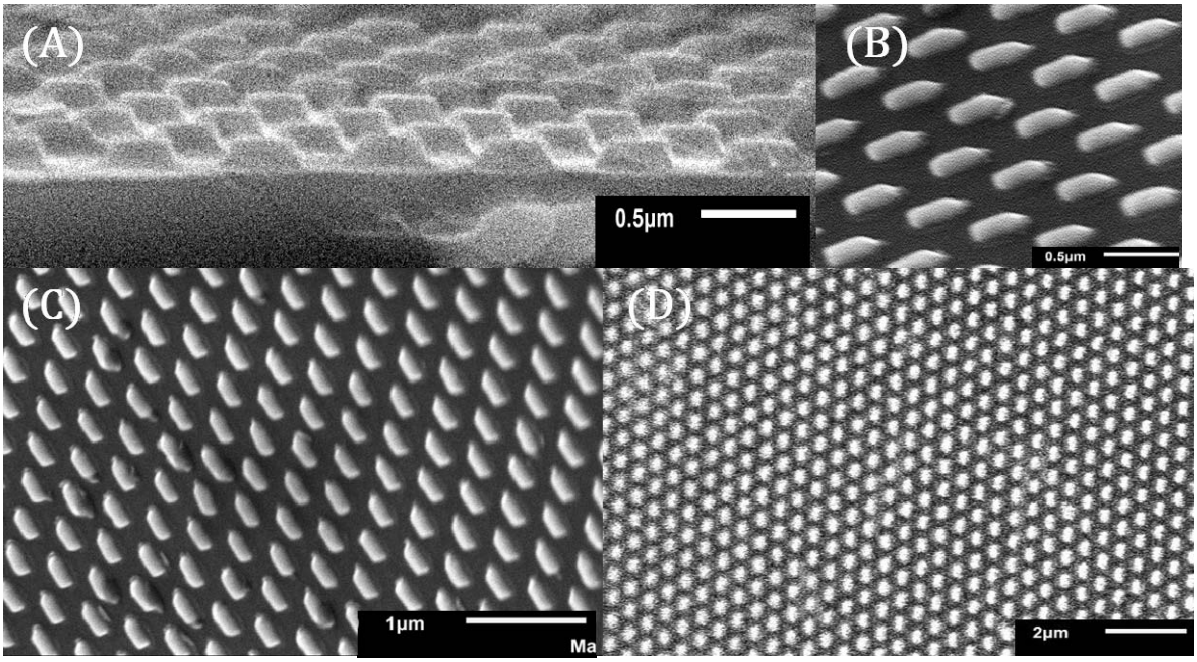

Figure 6.1. SEM images of the disk-shaped SAF nanoparticles using anisotropic deposition from different angles. The cross-section images show the array of SAF nanoparticles (A). (B), (C) and (D) show the array of SAF nanoparticles from top down with varying magnification. The images show that our method of using nanoimprint lithography can pattern array of SAF nanoparticles in large area without defects.

6.2.2. Magnetic reversal behavior of disk-shaped SAF nanoparticles

In order to first demonstrate the magnetic properties of our SAF, we prepared an array of disk-shaped SAF nanoparticles on the silicon substrate. The hysteresis loop was measured in the in-plane direction, in order to show superparamagnet-like behavior ($H_c \sim 0$) (Figure 6.2 (A)). While on the silicon substrate, the nanoparticles exhibit superparamagnet-like behavior. The same superparamagnet-like behavior must remain even after those nanoparticles are in aqueous solution. Therefore, we released the SAF nanoparticles in solution using a $SF_6 + O_2$ mixed gas plasma etch into aqueous solution for magnetic reversal characterization. We also observed the superparamagnet-like behavior ($H_c \sim 0$) for SAF nanoparticles released in solution (Figure 6.2 (B)). The superparamagnet-like behavior of

released disk-shaped SAF nanoparticles in solution is a positive indication that the released SAF nanoparticles are not agglomerating. Having confirmed the superparamagnet-like behavior of nanoparticles in solution, we proceeded to the mechanical rotation experiments in order to control the mechanical behavior of released SAF nanoparticles in solution.

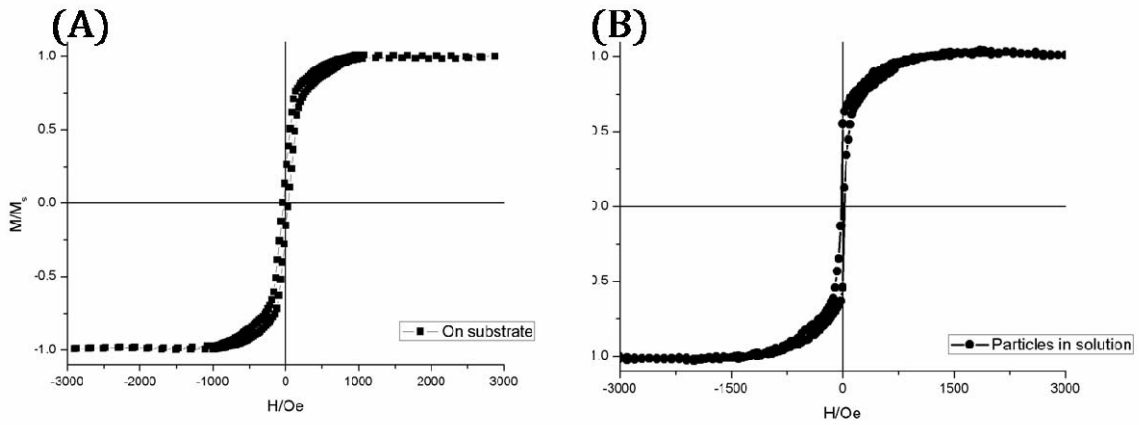

Figure 6.2. The magnetic hysteresis loop of SAF nanoparticles with four magnetic layers in an array form on silicon substrate (A), and in a released form in aqueous solution (B). SAF nanoparticles show super paramagnet-like behavior (H_c~0) and (M_r~0).

6.2.3. Mechanical rotation of SAF nanoparticles in solution

In order to use SAF nanoparticles for targeted cell death, the nanoparticles need to be able to deliver desired mechanical force to the cell. This is done by mechanically rotating the nanoparticles in solution. In order to confirm the mechanical rotation, we setup an instrument which can detect the mechanical rotation of magnetic nanoparticles in the solution using the laser (Figure 2.11). The laser is going through the vial with released magnetic nanoparticles, which is under the A.C. magnetic field, then the transmitted laser from the vial will be received by photodiode detector. In theory, the SAF nanoparticles would rotate to align itself to the external magnetic field due to in-plane preference of disk shape. This will increase the

laser intensity since the cross-section area, which blocks the incident laser, will be minimized. However, in absence of external magnetic field, SAF nanoparticles will exhibit Brownian motion, which is randomized motion due to collision between nanoparticles and aqueous solution molecules. This will decrease the laser intensity, since the randomized orientation of SAF nanoparticles will hinder the laser to be transmitted. Therefore, as the intensity of external magnetic field increases, the intensity of the transmitted laser should increase. Figure 6.3 shows the simple schematic diagram of particles in the absence of magnetic field, the diagram of particles in the presence of magnetic field, and the graph showing the laser intensity depending on magnetic field intensity.

Then we conducted the experiments with nanoparticles under external field of varying frequencies, from ~0.1 Hz to ~8 Hz, in order to confirm the mechanical rotation of the magnetic nanoparticles, which is governed by external magnetic field, and not by any other factor. Figure 6.3 shows the nanoparticle rotation frequency with the presence of magnetic field (A). As shown in the graph, 0.5 Hz of magnetic field produces 1 Hz of nanoparticle rotation. A.C magnetic field created by the rotating magnets have maximum positive magnetic field and minimum negative magnetic field, which both align the disk-shaped magnetic nanoparticles in in-plane direction. Therefore, magnetic nanoparticles would align to the field two times in one cycle of A.C magnetic field. Therefore, the frequency of magnetic nanoparticle rotation is always two times the frequency of magnetic field.

Furthermore, we observe the change in nanoparticle rotation frequency as the frequency of magnetic field changes. Frequency of 0.1 Hz (0.05 Hz of magnetic field) was set initially and increased to 8 Hz (4 Hz) of magnetic field using a rotating magnet. The result clearly shows that the nanoparticle rotation frequency increases as the magnetic field

frequency changes. However, we observe the decrease in laser intensity larger than 2 Hz (1 Hz of magnetic field). This is attributed to the viscous drag on magnetic nanoparticles, which delays the time for magnetic nanoparitcles to rotate in response to the external magnetic field. It takes approximately 0.5 s for magnetic nanoparticles to rotate fully in response to the external magnetic field. Therefore, as the frequency increases above such limit (>2 Hz), the magnetic nanoparticles will not make a full rotation, but partial rotation, which will decrease the difference of intensity of the transmitted laser. This trend is clearly shown in Figure 6.3 (B). With such results, we concluded that frequency above 2 Hz will not be suitable for our biomedical application since the rotation of magnetic nanoparticles is partial. However, we desire to deliver the maximum mechanical force from full rotation onto the cell within short amount of time. Therefore, we decided to proceed with frequency of 1 Hz for our cell experiment.

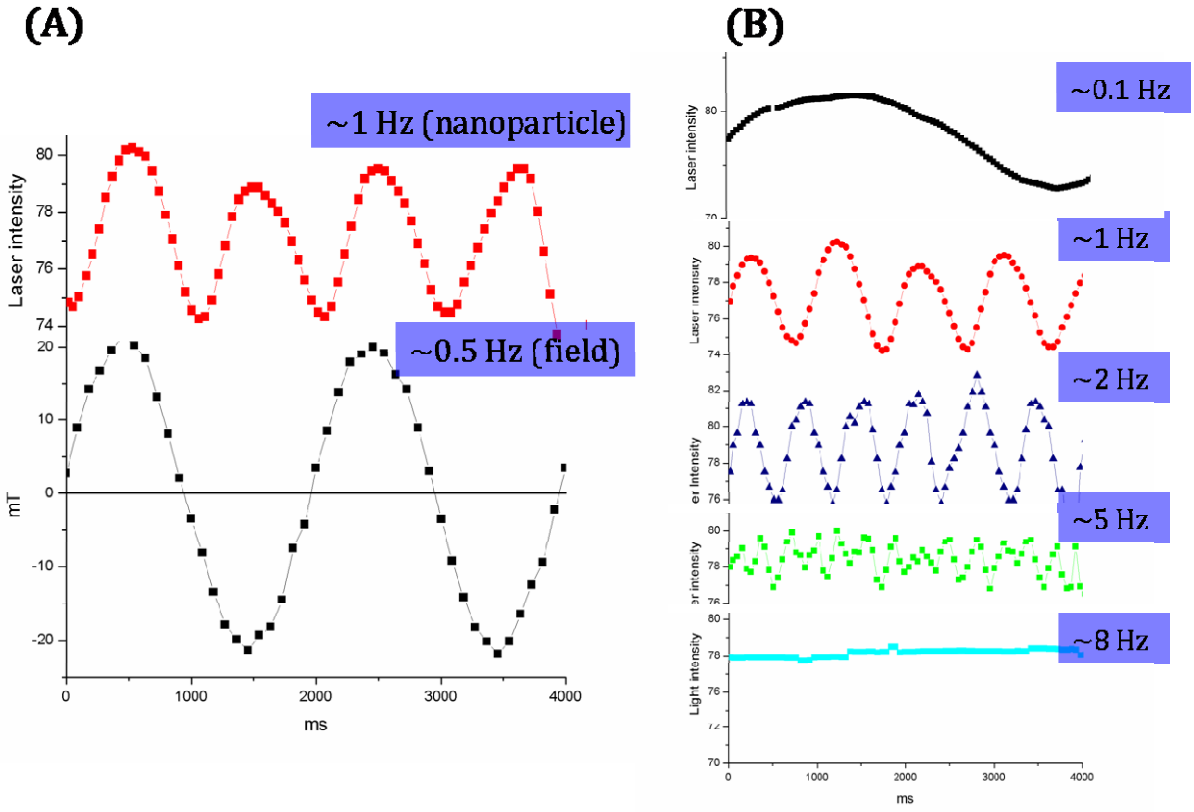

Figure 6.3. (A) (upper) graph of laser intensity change due to SAF nanoparticle rotation under A.C. magnetic field and (lower) graph of magnetic field respect to time. (B) graph of laser intensity change due to SAF nanoparticles rotation under different frequency of A.C magnetic field.

Chapter 7

Cell death via mechanical effect of SAF nanoparticles

7.1. Introduction

In Chapter 7, we demonstrate cell death via mechanical rotation of synthetic antiferromagnetic (SAF) nanoparticles. Specifically, we use HeLa cancer cells for their unlimited growing capacity. We show that our fabricated particles can effectively eradicate cancer cells that are otherwise immortal. The procedure of fabricating SAF nanoparticles were described in detail in Chapters 2, 5 and 6. In Chapter 6, we demonstrated that the frequency of mechanical rotation of nanoparticles in aqueous solution can be controlled using a rotating magnetic field. Here, we expand upon the use of mechanical rotation for cancer cell death.

7.2. HeLa cell culture

We chose HeLa cells for our experiment for their immortality, which specifies its inability to degrade. This makes HeLa cells desirable for our experiment, in which we demonstrate the ability to kill cells by inducing mechanical force by rotation of nanoparticles. The detailed protocol of culturing HeLa cell was described in Chapter 2.

For our experiment, we went through at least two passages before we conduct the

experiment using magnetic nanoparticles. It has been well established that when cells are thawed from the frozen state, cells do not exhibit their full characteristic for the first two passages. Also, when cells are initially thawed, some of the cells do not revive or recover fully. For later cell viability experiment, these dead or unhealthy cells must be removed from the culture flask. Therefore, while we go through several passages, we change the media of the culture flask in order to remove dead or unhealthy cells.

7.2.1. Time dependence on cell viability

Here, we introduced fabricated SAF nanoparticles into the cell with the following parameters: well size = one well in 24 well plate, cell number per well = 180,000, nanoparticle number per well = 180,000, ratio between cell number to nanparticle number = 1:1, maximum magnetic field = 200 mT, frequency of A.C magnetic field = 1 Hz. The only parameter that we vary for this particular experiment is the time of exposure to mechanically rotatating SAF nanoparticles. We increased the time of treatment using mechanically rotating SAF nanoparticles under A.C magnetic field from 0 min of exposure to 16 minutes of exposure. For this experiment, three wells were used per data points (0 minute, 1 minute, 2 minutes, 4 minutes, 8 minutes, and 16 minutes of treatment) in order to avoid any error. After the treatment, nanoparticles and dead cells were washed out with media in order to avoid any erroneous response to fluorescent agent. The rinsing of the wells should be done gently in order to retain healthy cell attachment to the well surface. After the thorough rinse, fluorescent agent Alamar Blue, was added for cell viability response. Alamar Blue is a cell viability indicator that uses the natural reducing power of living cells to convert Alamar Blue to the fluorescent molecule, resorufin. Alamar Blue itself is blue in color and virtually non-

fluorescent, but upon entering cells, Alamar Blue is reduced to resorufin, which produces very bright red fluorescence. By measuring the intensity of the fluorescence, we can generate quantitative data for cell viability. After Alamar Blue was added, wells were left to react in the incubator for 1.5 hours to allow sufficient reaction. Then we conducted cell viability experiment using fluorescence detector to confirm the cell death using SAF nanoparticles under A.C. magnetic field.

Figure 7.1 shows cell viability as a function of time of treatment. Cell viability did not change appreciably for exposure time under 4 minutes. After 8 minutes of exposure, however, approximately 20% of the cells died, and 80% of the cells were viable. After 16 minutes of exposure, we observed less than 8% of the cell was alive. This provides quantitative evidence that the use of SAF nanoparticles to mechanically affect the cells is an effective method to target cancer cells in a reasonable period of time (under 16 minutes).

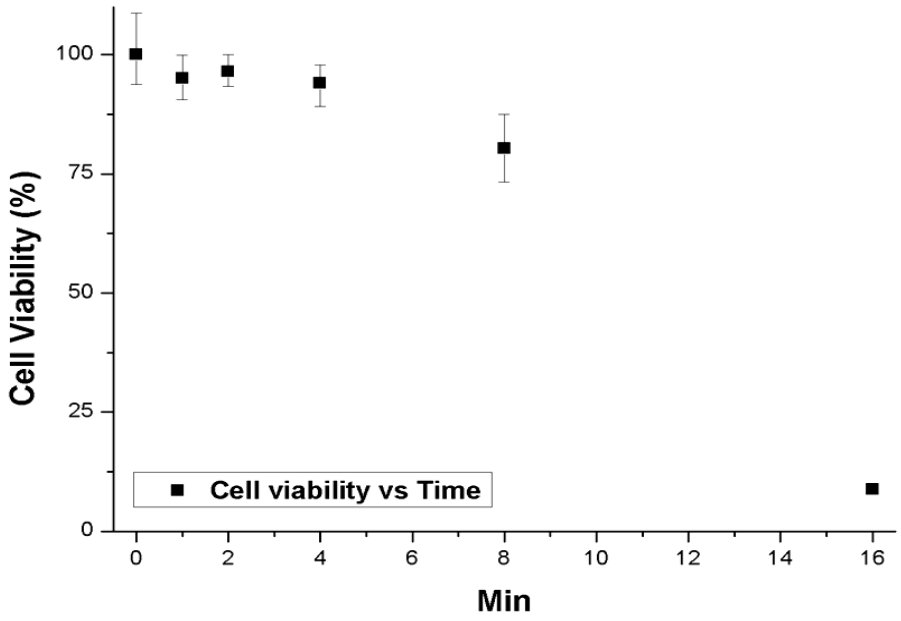

Figure 7.1. Mean cell viability due to time of exposure to SAF nanoparticles under mechanical rotation. Upto 8 minutes, cell viability doesn't change, but after 8 minutes, partial cell death was observed (~20%). After 16 minutes mark, almost complete cell death was observed (~92%)

7.2.2. Concentration of nanoparticle dependence on cell viability

At 1:1 concentration, we demonstrated that there was a decay of cell viability with time. By 16 minutes of exposure, more than 92% of cells were dead. However, for biomedical applications, it is important to minimize the amount of foreign objects introduced to the body. Toward this goal, we vary the ratio of nanoparticles to cells to determine the minimum amount of nanoparticles required for efficient cell death. At the time point of confirmed cell death (16 minutes), we varied the concentration from 1:1, 1:2, 1:4, and 1:8 (number of nanoparticles : number of cell). The exact same post-experimental procedure was followed to determine the fluorescence and subsequently cell viability of the final solution. Figure 7.2 shows the mean cell viability as a function of concentration. Here, the

concentration of 1:1 is considered as 100% concentration and 1:2 as 50% and so forth. As we decrease the concentration, we observed the increased number of cells alive after the exposure.

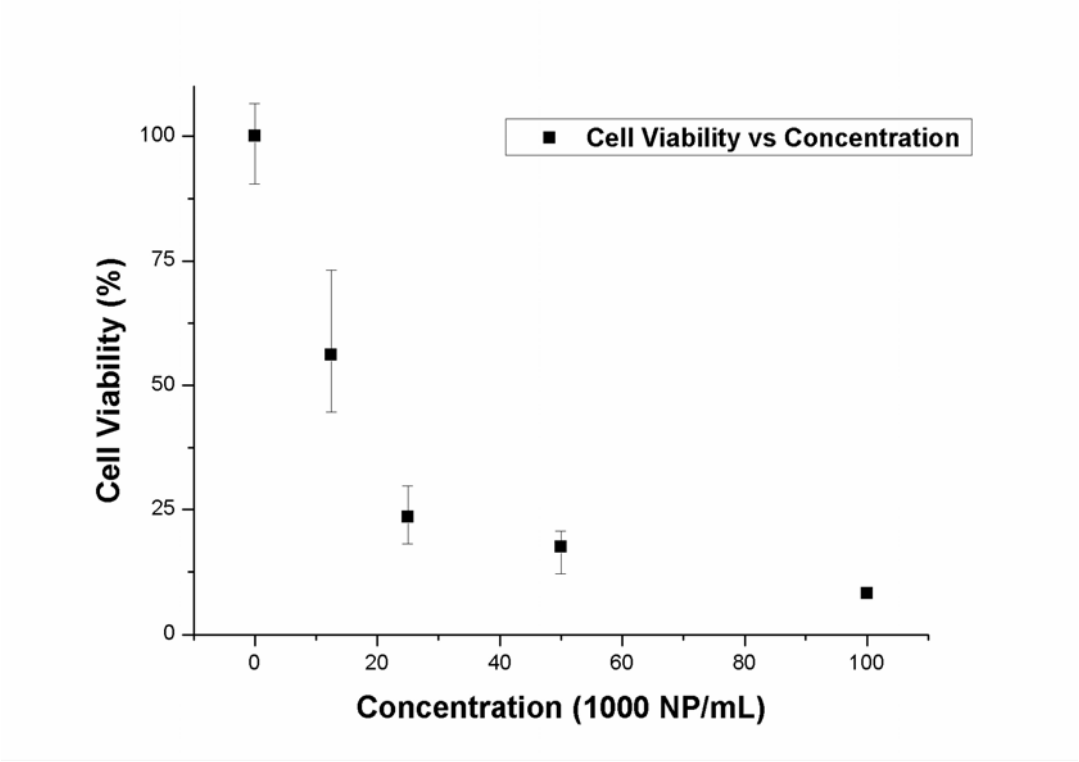

Figure 7.2. Mean cell viability due to concentration at 16 minutes of exposure to SAF nanoparticles under mechanical rotation. The cell to nanoparticle ratio was decrease from 1:1 to 1:8. As the concentration of nanoparticles decrease, the cell alive after the 16 minutes of exposure to SAF nanoparticles increase

This figure indicates that the amount of exposure/treatment time required for complete cell death is highly dependent on the concentration ratio of nanoparticles to cells. Here, we observed that there is a rapid drop in cell viability as we increase the concentration from 1:8 to 1:4. However, from 1:4 to 1:2, and from 1:2 to 1:1, we didn't observe much change in cell viability. From this result, we can partially conclude that there is a "threshhold" concentration at 1:4 in which the cell viability rapidly decreases due to exposure to magnetic nanoparticles. Even though higher concentration of magnetic nanoparticles would decrease

the cell viability even further, it would be most practical to utilize the threshhold concentration, considering the limited amount of magnetic nanoparticles available.

7.2.3. Calcium ICP analysis (Part of future work)

With confirmation of cancer cell death by mechanical perturbation, my initial goal has been achieved. However, the biological mechanism of this mechanical perturbation of the cell is of high interest due to its apoptosis nature.

In the stage of apoptosis, self-induced cell death, calcium signaling is involved in a number of key mechanisms[67-69]. Stimulus-induced calcium influx as a result of DNA fragmentation through membrane ionic channels, or calcium release from the internal cell sources, can result in the total perturbation of cellular calcium homeostasis and triggering of apoptosis[67-69]. Even though the mechanical force delivered by the magnetic nanoparticles can be meager, it is well established that this mechanical force, if transient and gentle, leads to the induction of stretch-activated channels, and further increasing levels of intracellular calcium ions[70-72]. Therefore, we investigate the calcium content comparison between samples with different cell viability in order to confirm the cell death by mechanical force delivered by magnetic nanoparticles.

Figure 7.3 shows the different calcium content of samples with different exposure time to mechanical rotation of magnetic nanoparticles.

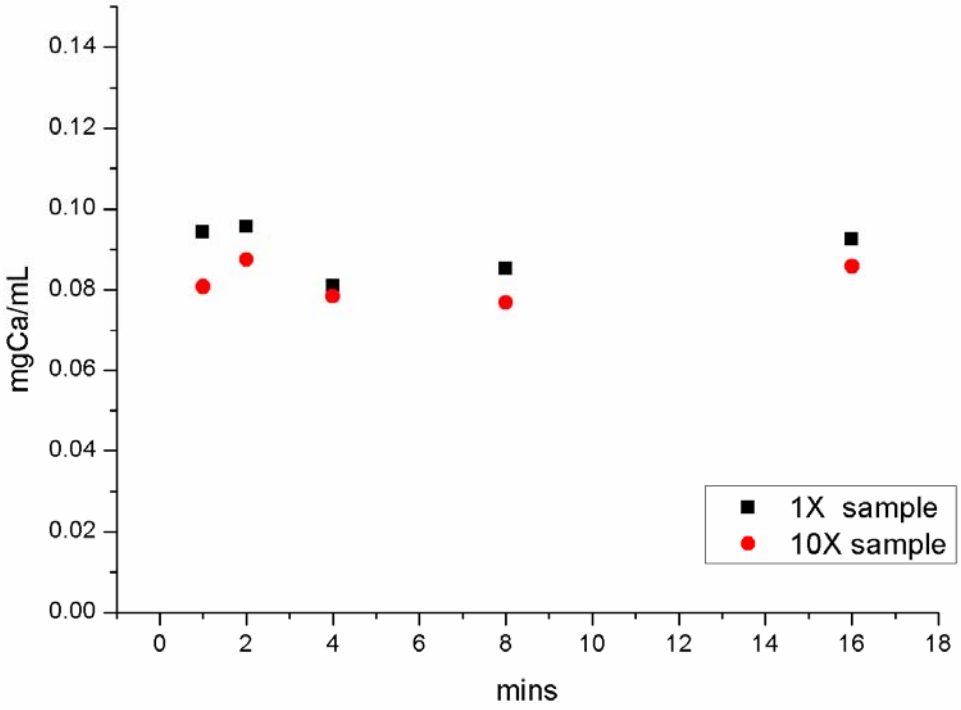

Figure 7.3. Calcium ICP analysis on HeLa cell samples exposed to mechanical rotation of magnetic nanoparticles with different durations. Calcium ICP analysis does not show any kind of trend depending on the difference in exposure time.

Please note that the calcium content analysis as a function of exposure time does not show any kind of trend. It has to be noted that the calcium ICP analysis is only a partial indication for confirming apoptosis for several reasons: 1) the calcium content of media is too high compared to the calcium created due to apoptosis, 2) DNA fragmentation—clear indication of apoptosis—causes calcium content increase, but it is a converse of such phenomenon which is not necessarily true, 3) Cell death by membrane rupture also has potential to provide similar result due to inherent calcium content within the cell.

Therefore, in order to provide a conclusive result of apoptosis, it is suggested to

conduct western blotting in order to confirm the DNA fragmentation. Western blotting is a analytical technique which can detect specific protein/DNA/RNA (depending on the analysis) in a sample of tissue homogenate or extract. After the process of gel electrophoresis to separate protein/DNA/RNA, the electric current through the protein/DNA/RNA in order to detect the electric current at the end, will differentiate cells with normal DNA and cells with fragmented DNA. However, this process requires a large number of new magnetic nanoparticles and new instrument set ups, which are not readily available. Therefore, in the future, it is suggested that a mass production of magnetic nanoparticles (comparable to number produced by chemical method) must be done. Furthermore, a collaboration with experts who are familiar with cell molecular analysis is suggested in order to understand and further investigate the cell death mechanism in biological level.

Chapter 8

Conclusion and Future Work

In this thesis we have:

1) Studied and confirmed the deposition of mono-phase Fe_3O_4 thin film by using magnetron sputtering.

2) Studied the magnetic properties of synthetic antiferromagnetic (SAF) configuration using Fe_3O_4 thin film, and optimizing the configuration in order to minimize the magnetic remanence and coercivity value.

3) Used the concept of SAF configuration and fabricated an array of nanoparticles via nanoimprint lithography with control of size/shape/structure.

4) Fabricated the sombrero-shaped Fe_3O_4 and SAF nanoparticles using isotropic deposition, and studied the magnetic/physical properties of sombrero-shaped magnetic nanoparticles.

5) Used disk-shaped SAF nanoparticles and released them into the aqueous solution.

6) Controlled the mechanical movement of SAF nanoparticles using A.C magnetic field and confirmed the SAF nanoparticles rotate.

7) Implemented SAF nanoparticles to cell environment to investigate the cell viability due to

the time of exposure to mechanical rotating SAF nanoparticles, and cell viability due to the concentration of SAF nanoparticles in aqueous solution.

8) Conducted a calcium ICP analysis in order to investigate the calcium content of samples—indication of apoptosis— with different exposure time to mechanical force created by magnetic nanoparticles.

This thesis provides a systematic study of magnetism, fabrication and application using SAF nanoparticles. Even though SAF nanoparticles have been demonstrated to be effective for targeted cancer cell death by mechanical effects, this concept of using nanoparticles requires further investigation before the idea becomes applicable.

In order to proceed with the idea of mechanically rotating top-down lithographic magnetic nanoparticles and inducing cancer cell death, a way to mass produce the top-down lithographic nanoparticles is required. Nanoimprint lithography can retain the integrity of resolution and can pattern sufficiently large areas, but the fabrication process is not facile to be repeated reliably. Therefore, one of the way to improve the turn-over number of nanoparticles would be using a roll-to-roll system rather than using a hand-to-hand production. This will help to produce the sufficient number of nanoparticles (comparable to number of nanoparticles produced by chemical synthesis) in relatively short amount of time

For cancer cell death, we have studied and confirmed the cancer cell death by mechanical effect, but the biological mechanism of cancer cell death was not fully investigated. We were able to partially confirm the apoptosis through calcium ICP analysis, but as mentioned in Chapter 7, calcium ICP only provides a partial indication due to several reasons. Therefore, it is highly suggested to conduct further molecular level analysis, such as western blotting, in order to confirm the DNA fragmentation, which is complete indication of

apoptosis.

Reference:

1 Krishnan, K. M. Biomedical nanomagnetics: a spin through possibilities in imaging, diagnostics, and therapy. *IEEE transactions on magnetics* **46**, 2523 (2010).

2 Ferguson, R. M., Minard, K. R., Khandhar, A. P. & Krishnan, K. M. Optimizing magnetite nanoparticles for mass sensitivity in magnetic particle imaging. *Med Phys* **38**, 1619-1626 (2011).

3 Khandhar, A. P., Ferguson, R. M., Simon, J. A. & Krishnan, K. M. Tailored magnetic nanoparticles for optimizing magnetic fluid hyperthermia. *Journal of Biomedical Materials Research Part A* **100**, 728-737 (2012).

4 Lin, M. M., Kim, H.-H., Kim, H., Muhammed, M. & Kim, D. K. Iron oxide-based nanomagnets in nanomedicine: fabrication and applications. *Nano Reviews* **1** (2010).

5 Martínez-Mera, I., Espinosa-Pesqueira, M., Pérez-Hernández, R. & Arenas-Alatorre, J. Synthesis of magnetite (Fe< sub> 3</sub> O< sub> 4</sub>) nanoparticles without surfactants at room temperature. *Materials Letters* **61**, 4447-4451 (2007).

6 Massart, R. Preparation of aqueous magnetic liquids in alkaline and acidic media. *Magnetics, IEEE Transactions on* **17**, 1247-1248 (1981).

7 Woo, K., Lee, H. J., Ahn, J. P. & Park, Y. S. Sol–gel mediated synthesis of Fe2O3 nanorods. *Advanced Materials* **15**, 1761-1764 (2003).

8 Feldmann, C. & Jungk, H. O. Polyol-Mediated Preparation of Nanoscale Oxide Particles. *Angewandte Chemie International Edition* **40**, 359-362 (2001).

9 Shafi, K. V. *et al.* Sonochemical synthesis of functionalized amorphous iron oxide nanoparticles. *Langmuir* **17**, 5093-5097 (2001).

10 Kobori, H. *et al.* in *Journal of Physics: Conference Series.* 022042 (IOP Publishing).

11 Hu, W. *et al.* Synthetic antiferromagnetic nanoparticles with tunable susceptibilities. *J Appl Phys* **105**, 7B508, doi:10.1063/1.3072028 (2009).

12 Krishnan, K. M. *et al.* Nanomagnetism and spin electronics: materials, microstructure and novel properties. *Journal of materials science* **41**, 793-815 (2006).

13 Kim, D.-H. *et al.* Biofunctionalized magnetic-vortex microdiscs for targeted cancer-cell destruction. *Nature materials* **9**, 165-171 (2009).

14 Vitol, E. A., Novosad, V. & Rozhkova, E. A. Multifunctional ferromagnetic disks for modulating cell function. *IEEE transactions on magnetics* **48**, 3269 (2012).

15 Vitol, E. A., Novosad, V. & Rozhkova, E. A. Microfabricated magnetic structures for future medicine: from sensors to cell actuators. *Nanomedicine* **7**, 1611-1624 (2012).

16 Mund, H. *et al.* Investigation of orbital magnetization in inverse spinel cobalt ferrite using magnetic Compton scattering. *Journal of Applied Physics* **110**, 073914 (2011).

17 Chen, C.-W. *Magnetism and metallurgy of soft magnetic materials*. (Courier Corporation, 2013).

18 Yuan, S., Zhou, Z. & Li, G. Structural evolution from mesoporous α-Fe 2 O 3 to Fe 3 O 4@ C and γ-Fe 2 O 3 nanospheres and their lithium storage performances. *CrystEngComm* **13**, 4709-4713 (2011).

19 Chambers, S., Kim, Y. & Gao, Y. Fe 2p core-level spectra for pure, epitaxial α-Fe2O3 (0001), γ-Fe2O3 (001), and Fe3O4 (001). *Surface Science Spectra* **5**, 219-228 (1998).

20 Lu, J., Jiao, X., Chen, D. & Li, W. Solvothermal synthesis and characterization of Fe3O4 and γ-Fe2O3 nanoplates. *The Journal of Physical Chemistry C* **113**, 4012-4017 (2009).

21 De Faria, D., Venâncio Silva, S. & De Oliveira, M. Raman microspectroscopy of

some iron oxides and oxyhydroxides. *Journal of Raman spectroscopy* **28**, 873-878 (1997).
22 Hyeon, T., Lee, S. S., Park, J., Chung, Y. & Na, H. B. Synthesis of highly crystalline and monodisperse maghemite nanocrystallites without a size-selection process. *Journal of the American Chemical Society* **123**, 12798-12801 (2001).
23 Wang, A., Haskin, L. & Jolliff, B. in *29th Annual Lunar and Planetary Science Conference.*
24 Kim, D. *et al.* Interface electronic structures of BaTiO 3@ X nanoparticles (X= γ-Fe 2 O 3, Fe 3 O 4, α-Fe 2 O 3, and Fe) investigated by XAS and XMCD. *Physical Review B* **79**, 033402 (2009).
25 Sklyarova, A. Mössbauer spectra of iron oxides in the bulk and nanocrystalline states. (2010).
26 Daniels, J. & Rosencwaig, A. Mössbauer spectroscopy of stoichiometric and non-stoichiometric magnetite. *Journal of Physics and Chemistry of Solids* **30**, 1561-1571 (1969).
27 Zhu, J.-G. Spin valve and dual spin valve heads with synthetic antiferromagnets. *Magnetics, IEEE Transactions on* **35**, 655-660 (1999).
28 Zhu, J.-G. & Zheng, Y. Characteristics of AP bias in spin valve memory elements. *Magnetics, IEEE Transactions on* **34**, 1063-1065 (1998).
29 Sakuraba, Y. *et al.* Giant tunneling magnetoresistance in Co2MnSi⁄ Al–O⁄ Co2MnSi magnetic tunnel junctions. *Applied physics letters* **88**, 192508 (2006).
30 Sakuraba, Y. *et al.* Huge Spin-Polarization of L21-Ordered Co2MnSi Epitaxial Heusler Alloy Film. *Japanese journal of applied physics* **44**, L1100 (2005).
31 Sakuraba, Y., Ueda, M., Bosu, S., Saito, K. & Takanashi, K. CPP-GMR study of half-metallic full-Heusler compound Co 2 (Fe, Mn) Si. *Journal of the Magnetics Society of Japan* **38**, 45-49 (2014).
32 Sakuraba, Y. *et al.* Extensive study of giant magnetoresistance properties in half-metallic Co2 (Fe, Mn) Si-based devices. *Applied Physics Letters* **101**, 252408 (2012).
33 Baibich, M. N. *et al.* Giant magnetoresistance of (001) Fe/(001) Cr magnetic superlattices. *Physical review letters* **61**, 2472 (1988).
34 Hu, W. *et al.* High-Moment Antiferromagnetic Nanoparticles with Tunable Magnetic Properties. *Advanced Materials* **20**, 1479-1483 (2008).
35 Hu, W. *et al.* Fabrication of planar, layered nanoparticles using tri-layer resist templates. *Nanotechnology* **22**, 185302 (2011).
36 Zhang, W. & Krishnan, K. M. Direct release of synthetic antiferromagnetic nanoparticles fabricated by defect-free thermal imprinting. *Journal of Applied Physics* **111**, 07B509 (2012).
37 Kwon, B. S., Li, Z., Zhang, W. & Krishnan, K. M. Sombrero-shaped Fe3O4 nanoelements with tunable out-of-plane and in-plane magnetization components fabricated by nano-imprint lithography. *Journal of Applied Physics* **115**, 17B506 (2014).
38 Kwon, B. S., Zhang, W., Li, Z. & Krishnan, K. M. Direct Release of Sombrero-Shaped Magnetite Nanoparticles via Nanoimprint Lithography. *Advanced Materials Interfaces* (2015).
39 Hou, Y.-f., Zhan, Q.-f. & Krishnan, K. M. Magnetization reversal in exchange biased IrMn/Fe ring arrays. *Applied Physics Letters* **98**, 042510 (2011).
40 Zhang, W., Bowden, M. E. & Krishnan, K. M. Competing effects of magnetocrystalline anisotropy and exchange bias in epitaxial Fe/IrMn bilayers.

Applied Physics Letters **98**, 092503 (2011).
41 Gennardo, D. J. *Design, construction, and optimization of a magnetron sputtering system for urania deposition*, University of Illinois at Urbana-Champaign, (2010).
42 McCord, M. A. & Rooks, M. J. in *SPIE, Bellingham.*
43 Vieu, C. *et al.* Electron beam lithography: resolution limits and applications. *Applied Surface Science* **164**, 111-117 (2000).
44 Microchem. http://microchem.com/pdf/PMMA_Data_Sheet.pdf.
45 Microchem. http://www.microchem.com/pdf/removerpg.pdf.
46 Chou, S. Y., Krauss, P. R. & Renstrom, P. J. Nanoimprint lithography. *Journal of Vacuum Science & Technology B: Microelectronics and Nanometer Structures* **14**, 4129-4133 (1996).
47 Chou, S. Y., Krauss, P. R. & Renstrom, P. J. 25-nanometer resolution. *Science272*, 85-87 (1996).
48 Chou, S. Y., Krauss, P. R., Zhang, W., Guo, L. & Zhuang, L. Sub-10 nm imprint lithography and applications. *Journal of Vacuum Science & Technology B* **15**, 2897-2904 (1997).
49 Choi, S.-J., Yoo, P. J., Baek, S. J., Kim, T. W. & Lee, H. H. An ultraviolet-curable mold for sub-100-nm lithography. *Journal of the American Chemical Society* **126**, 7744-7745 (2004).
50 Ahn, S. H. & Guo, L. J. High-speed roll-to-roll nanoimprint lithography on flexible plastic substrates. *Advanced materials* **20**, 2044-2049 (2008).
51 Weiss, D. N., Meyers, S. T. & Keszler, D. A. All-inorganic thermal nanoimprint process. *Journal of Vacuum Science & Technology B* **28**, 823-828 (2010).
52 Koo, N. *et al.* Improved mold fabrication for the definition of high quality nanopatterns by soft UV-nanoimprint lithography using diluted PDMS material. *Microelectronic Engineering* **84**, 904-908 (2007).
53 Koo, N. *et al.* The fabrication of a flexible mold for high resolution soft ultraviolet nanoimprint lithography. *Nanotechnology* **19**, 225304 (2008).
54 Guo, L. J. Recent progress in nanoimprint technology and its applications. *Journal of Physics D: Applied Physics* **37**, R123 (2004).
55 Zhang, W. & Krishnan, K. M. Direct release of synthetic antiferromagnetic nanoparticles fabricated by defect-free thermal imprinting. *Journal of Applied Physics* **111**, 07B509-507B509-503 (2012).
56 Zhang, W. & Krishnan, K. M. Epitaxial patterning of thin-films: conventional lithographies and beyond. *Journal of Micromechanics and Microengineering* **24**, 093001 (2014).
57 Barbero, D. R. *et al.* High-Resolution Nanoimprinting with a Robust and Reusable Polymer Mold. *Advanced Functional Materials* **17**, 2419-2425 (2007).
58 Weiss, D. N. *et al.* Nanoimprinting for diffractive light trapping in solar cells. *Journal of Vacuum Science & Technology B* **28**, C6M98-C96M103 (2010).
59 Rohrer, G. S. *Structure and bonding in crystalline materials*. (Cambridge University Press, 2001).
60 Warren, B. E. *X-ray Diffraction*. (Courier Corporation, 1969).
61 Scheinfein, M. *et al.* Micromagnetics of domain walls at surfaces. *Physical Review B* **43**, 3395 (1991).
62 Scheinfein, M. R. http://llgmicro.home.mindspring.com/.
63 Liu, J. P., Fullerton, E., Gutfleisch, O. & Sellmyer, D. J. *Nanoscale magnetic materials and applications*. (Springer, 2009).

64 Tong, H. *et al.* The spin flop of synthetic antiferromagnetic films. *Journal of Applied Physics* **87**, 5055-5057 (2000).
65 Li, Z. & Krishnan, K. M. Highly stable signal propagation in a consecutively tuned nanomagnet array. *Journal of Applied Physics* **113**, 17B901-917B901-903 (2013).
66 Li, Z., Kwon, B. S. & Krishnan, K. M. Misalignment-free signal propagation in nanomagnet arrays and logic gates with 45°-clocking field. *Journal of Applied Physics* **115**, 17E502 (2014).
67 Mattson, M. P. & Chan, S. L. Calcium orchestrates apoptosis. *Nature cell biology* **5**, 1041-1043 (2003).
68 Clapham, D. E. Calcium signaling. *Cell* **80**, 259-268 (1995).
69 Boehning, D. *et al.* Cytochrome c binds to inositol (1, 4, 5) trisphosphate receptors, amplifying calcium-dependent apoptosis. *Nature cell biology* **5**, 1051-1061 (2003).
70 Adachi, T., Sato, K. & Tomita, Y. Directional dependence of osteoblastic calcium response to mechanical stimuli. *Biomechanics and Modeling in Mechanobiology* **2**, 73-82 (2003).
71 Diamond, S. L., Sachs, F. & Sigurdson, W. J. Mechanically induced calcium mobilization in cultured endothelial cells is dependent on actin and phospholipase. *Arteriosclerosis, Thrombosis, and Vascular Biology* **14**, 2000-2006 (1994).
72 Guharay, F. & Sachs, F. Stretch-activated single ion channel currents in tissue-cultured embryonic chick skeletal muscle. *The Journal of physiology* **352**, 685 (1984).